Diss. ETH No. 21559

Turbine Design Optimizations using High Fidelity CFD

A dissertation submitted to

ETH Zurich

for the degree of

Doctor of Sciences

presented by

Altug Melik Basol

M.S., Bogazici University
born August 04, 1980
citizen of Turkey

accepted on the recommendation of
Prof. Dr. Reza S. Abhari, examiner
Prof. Dr. Patrick Jenny, co-examiner

Zurich, 2014

Our responsibility is to do what we can, learn what we can, improve the solutions and pass them on.

Richard Feynman

Acknowledgement

Abstract

Temperature distribution downstream of the combustor exhibits non-uniformities both in radial and circumferential directions. When the relatively hot gases termed as hot streaks migrate downstream they alter both the aerodynamics of the turbine and increase the incident heat load on the HP turbine along their flow path. This study numerically investigates the interaction of the hot streaks with the turbine aerodynamics using an unsteady particle tracking tool in conjunction with the unsteady RANS simulations.

The necessary numerical tools required have been developed and the capabilities of the existing tools have been extended enabling more accurate and faster numerical predictions. Regarding the accuracy the solver's capability in modeling the diffusion processes is greatly improved through the development of novel techniques. The k-ω turbulence model enabled to impose the highly turbulent flow field downstream of the combustor which greatly affects the mixing behavior within the turbine. A cell Reynolds and local CFL number scaled, anisotropic artificial dissipation algorithm is proposed for the Ni-Lax Wendroff scheme to improve the accuracy at the very high aspect ratio cells used at the wall in RANS simulations. The new artificial dissipation scheme showed a superior accuracy in resolving the boundary layers compared to the similar central 2nd order schemes present in the literature and resulted in a more accurate prediction of the secondary flows especially of the tip leakage vortex. A further improvement is also observed in the studies with the temperature non-uniformities present at the turbine inlet. Regarding the speed the solver is GPU accelerated which enabled to complete unsteady, one-and-a-half stage turbine simulations within 24 hours.

In the numerical study the inlet boundary conditions are taken from the experiments that are conducted in the axial research turbine facility "LISA" at ETH Zurich. Two different hot streak shapes have been considered. With its relatively high circumferential temperature gradients the circular hot streak models the temperature distribution downstream of the

can-annular combustors. For the second study a non-axisymmetric hot streak shape has been considered which has reduced circumferential temperature gradients at midspan and has different spanwise extents impinging on the opposite sides of the stator. With these properties it models the temperature distribution downstream of the more recent full annular combustor designs. The numerical results have been validated in different aspects with the time resolved measurements conducted. Flow physics behind the observed hot streak migration patterns is in detail discussed revealing the effect of the stator aerodynamics, non-axisymmetric endwall profiling and also the hot streak induced secondary flows.

The unsteady particle tracking studies revealed the increase in the radial transport within the rotor blade in presence of hot streaks. As the underlying mechanism in the rise in the radial transport, the effect of the hot streak induced secondary flows on the rotor blade heat load is investigated. The hot streak induced secondary flows in the case of the circular hot streak led to about 0.25 % rise in the adiabatic wall temperature level at the rotor pressure side that would correspond to about 5 K rise in the real engine conditions. On the other hand, the temperature level at the rotor suction side was completely insensitive to the presence of the secondary flows induced by the hot streaks. The particle tracking studies also showed a considerable effect of the stator aerodynamics on the hot streak migration. Accordingly, the main hot streak convection to the rotor blade tip originates from the region close to the stator suction side at the inlet plane. Also the non-axisymmetric endwalls affect the hot streak migration. They reduce the circumferential non-uniformity in the hot streak convection to the rotor blade tip.

Parallel to the migration pattern observed, adaptations in the hot streak's circumferential orientation at the turbine inlet have been conducted by taking the combustor framework into account for the applicability of the considered temperature boundary conditions in real engines. For the circular hot streak the fuel injector – stator clocking has been considered. Due to its relatively high circumferential temperature gradients clocking the circular hot streak even by 10% of the stator pitch towards the stator's pressure side led to considerable reductions in the rotor blade tip adiabatic wall temperature levels that would correspond up to 24 K in realistic engine conditions.

For the non-axisymmetric hot streak shape the effect of impinging the spanwise larger edge of the hot streak on the opposite sides of the stator blade on the rotor blade heat load is evaluated. The alignment of the hot streak's spanwise larger extent to stator's pressure side reduced the adiabatic wall temperature levels both at the rotor midspan and also at the tip region reaching values up to 10 K in realistic engine conditions. Controlling the penetration of the dilution air on the liner the circumferential temperature distribution at the endwalls can be modified according to the observed turbine aerodynamics. This method is proposed as a more practical approach to be used in modern full-annular combustors as opposed to the fuel injector – stator clocking which puts serious constraints both on the turbine and combustor design.

Kurzfassung

Die Temperaturverteilung am Austritt der Brennkammer weist Ungleichmäßigkeiten sowohl in radialer als auch in Umfangsrichtung. Wenn die relativ heißen Gase, die als "heisse Streifen" bezeichnet sind, durch die Turbine strömen, sie erhöhen nicht nur die Wärmebelastung auf die Hochdruck-Turbine entlang ihrer Strömungsweg sondern sie verändern auch die Aerodynamik der Turbine. Diese numerische Studie untersucht die Wechselwirkung der "heissen Streifen" mit der Turbinen-Aerodynamik anhand eines instationären Partikel Verfolgung Programm in Verbindung mit der instationären RANS Simulationen.

Die notwendigen numerischen Werkzeuge sind entwickelt worden und die Fähigkeiten der vorhandenen Werkzeuge wurden erweitert um genauere und schnellere numerische Resultate zu ermöglichen. In Bezug auf die Genauigkeit, die Fähigkeit des numerischen Strömungslösers in der Modellierung der Diffusionsprozesse durch die Entwicklung neuer Techniken stark verbessert. Die k-ω Turbulenzmodell ermöglicht die Modellierung von hoch turbulenter Strömung an dem Austritt vom Brennkammer, der ein großer Einfluss auf das Mischverhalten innerhalb der Turbine hat. Zusätzlich eine anisotropische künstliche Dämpfung Methode ist für die Ni-Lax Wendroff numerische Methode entwickelt worden, welche die Dämpfung Koeffizienten in Beziehung mit der lokalen Zell Reynolds Nummer und lokalen CFL Anzahl skaliert. Das neue Modell verbessert die Genauigkeit der Resultate besonders bei den hoch gestreckten Zellen an den Wänden in RANS Simulationen. Die neue künstliche Dämpfung erhöhte die Präzision des numerische Lösers besonders in Grenzschichten im Vergleich zu den ähnlichen Lösern mit zentralen Differenzen in der Literatur und führt in Folge zu einem genaueren Prognose der sekundären Strömungen insbesondere des Schaufelspitzenwirbels. Eine weitere Verbesserung ist auch in den Simulationen mit der Temperatur Ungleichmäßigkeiten am Turbineneintritt beobachtet worden. In Bezug auf die Geschwindigkeit der numerische Löser ist GPU-beschleunigt worden und anhand dieser Geschwindigkeit können instationäre ein-und-ein-halb stufigen Turbinen Simulationen in 24 Stunden durchgeführt werden. In dieser numerischen Untersuchung die

Randbedingungen am Turbinen Eintritt sind aus den Experimenten hergeleitet,die in der axialen Forschung Turbinen Anlage "LISA" an der ETH Zürich durchgeführt worden sind. Zwei unterschiedliche Formen von "heissen Streifen" sind untersucht worden. Mit seiner relativ hohen Temperaturgradienten in der Umfang Richtung die kreisförmigen "heissen Flecke" modellieren die Temperaturverteilung hinter den ringförmigen Kanne-brennkammern. Für die zweite Studie eine nicht-achsensymmetrische Form von heissen Fleck wurde betrachtet, welche geringe Temperaturgradienten in der Umfang Richtung besitzt und unterschiedliche Spannweiten auf den gegenüberliegenden Seiten des Stator hat. Mit diesen Eigenschaften ist die Temperaturverteilung hinter dem moderneren Voll-ringförmigen Brennkammerdesign ist modelliert worden. Die numerischen Ergebnisse wurden in verschiedenen Aspekten anhand der zeitaufgelösten Messungen validiert. Strömungsphysik über das beobachtete Strömungsverhalten des "heissen Streifens" ist im Detail diskutiert dass die Wirkung der Stator Aerodynamik, der nicht-achsensymmetrischen Stirnwand Formgebung und auch der zusätzlichen sekundären Strömungen an dem Strömungsverhalten sind gezeigt worden.

Die instationären Partikel Verfolgung Studien zeigten die Zunahme der radialen Transport innerhalb des Rotorschaufels in Anwesenheit von heißen Streifen. Die Wirkung von Sekundärströmungen verursacht durch die "heissen Streifen", die der zugrunde liegende Mechanismus für den Anstieg in der radialen Transport ist, an die Wärmebelastung der Rotorschaufeln wird untersucht. Sie führen im Falle des kreisförmigen "heißen Flecks" zu etwa 0.25% Anstieg in dem adiabatischen Wand Temperaturniveau am Rotor Druckseite, die bis etwa 5K Anstieg an der realen Bedingungen entsprechen würde. Auf der anderen Seite war das Temperaturniveau am Rotor Saugseite völlig unempfindlich gegenüber der Anwesenheit der Sekundärströmung durch die heißen Streifen. Die Partikel-Tracking-Studien zeigten auch einen erheblichen Einfluss der Stator-Aerodynamik auf die Strömung von "heissen Streifen". Folglich stammt die Haupt "heisse Streifen" Konvektion an die Rotorschaufellspitze aus dem Bereich in der Nähe des Stator Saugseite am Turbineneintritt. Auch die nicht-achsensymmetrischen Stirnseiten beeinflussen die Strömung von "heissen Streifen". Sie reduzieren die Uneinheitlichkeit in der Umfangsrichtung in der "heissen Streifen" Konvektion an die Rotorschaufelspitze.Parallel zum beobachteten Strömungsverhalten der "heissen Streifen" Anpassungen in

der Orientierung des „heissen Flecks" am Turbineneintritt sind durchgeführt worden wobei die Brennkammer Geometrie für die Anwendbarkeit der betrachteten Temperatur Randbedingungen in realen Gas Turbinen berücksichtigt worden ist. Für die kreisförmige heißen Streifen das Brennstoff Einspritzventil - Stator Taktung wurde berücksichtigt. Aufgrund seiner relativ hohen umlaufenden Temperaturgradienten Takten des kreisförmigen heißen Flecks sogar von 10% des Stator Nickwinkels in die Richtung des Stators Druckseite führt zu erheblichen Reduzierungen des adiabatische Wandtemperaturniveau der Rotorschaufelspitze, die bis zu 24K in realistischen Bedingungen entsprechen würde.

Für die nicht-achsensymmetrischen heissen Fleck Form der Effekt des Auftreffens der Seite mit der grösseren Spannweite des heissen Flecks auf die gegenüberliegenden Seiten des Stators an dem Rotorschaufel Wärmelast ausgewertet. Die Ausrichtung der Seite des heissen Flecks mit der grösseren Spannweite auf die Druckseite des Stator reduziert das adiabatische Wandtemperaturniveau des Rotorschaufels an der mittleren Spanweite und auch an der Spitze das bis zu 10 K in realistischen Bedingungen entsprechen würde. Bei Steuerung der Penetration der Verdünnungsluft am Brennkammer die Temperaturverteilung an der Stirnwände an der Brennkammer Austritt können nach den beobachteten Turbinen Aerodynamik modifiziert werden. Diese Methode kann als praktischer Ansatz in der modernen Voll-Ringbrennkammern verwendet werden, im Gegensatz zu dem Brennstoff Injektor - Stator Taktung, welche schwere Einschränkungen sowohl auf die Turbine und als auch auf das Brennkammerdesign hat.

Table of Contents

1. Introduction

The goals of achieving gas turbines with high efficiency, low environmental impact, and offering a long component life time are in general conflicting. Modern gas turbines are designed to offer a good compromise between these conflicting goals trying to match the strict requirements in all these separate aspects. For example, the need for more efficient turbines drives up the turbine inlet temperature level which has an adverse effect on the life time of the turbine components. On the other hand, cooling the turbine heavily increases the component life time but reduces the thermodynamic cycle performance. The ultimate goal in the design is to cool the blade just as necessary to preserve its structural integrity for a given blade life time in order not to lose the additional rise in thermal efficiency with the penalty on the thermodynamic cycle performance by using excessive amount of coolant mass flow. However, as the temperature level rises, the design margins are also decreasing. Han, Dutta and Ekkad [1] state that at the temperature levels modern gas turbines operate even a 25K under-prediction of the blade metal temperature can result in a halving of its life.

Moreover, the combustor outlet temperature distribution is non-uniform which brings an additional complexity into the design process. This non-uniformity is due to the presence of discrete fuel injectors, due to the non-uniformity in the flame temperature and also due to the air injection from the liner both to cool the liner itself and the regulate the radial temperature profile upstream of the HP turbine stage. The temperature distribution downstream of the combustor of a military engine is given in Figure 1.1. The relatively hot gases coming out from the combustor are termed as hot streaks and have distinct migration patterns within the HP turbine and affect thereby the turbine aerodynamics. Moreover, they increase the heat load along their flow path and reduce the component life time if necessary measures in terms of cooling are not taken. There are two main groups of application areas for the gas turbines which directly affect the type of the combustor used and thereby also the resulting combustor outlet temperature distribution.
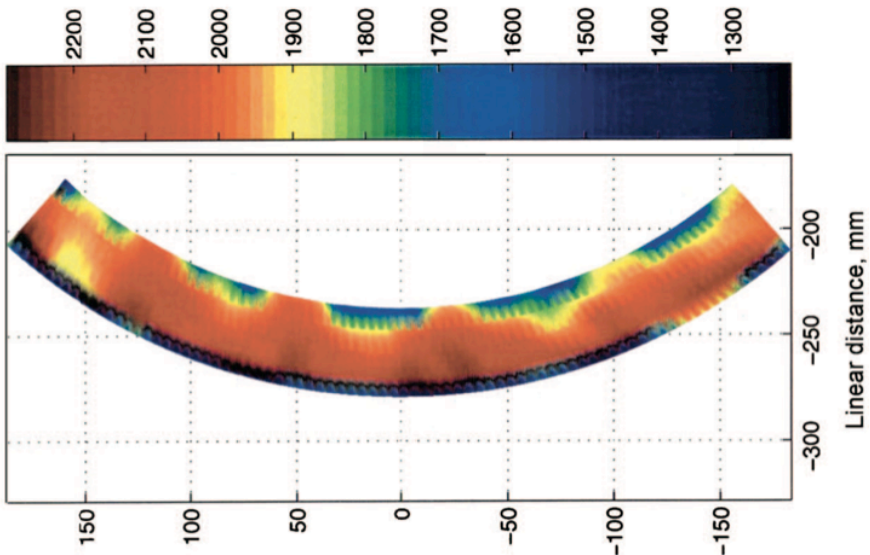
Figure 1.1 Measured temperature profile (K) at the combustor exit plane of a military engine with 20 burners - from QinetiQ [2]

1.1. Combustor Technologies

The state of the art gas turbines used for the power generation are facilitated with the lean premixed type combustors known for their very low NOx formation operating character. In the lean premixed combustion technology the air discharged from the compressor is mixed with the fuel to form a lean mixture before delivery to the combustor. The key in reducing the NOx level with this method is to burn the fuel under lean conditions with excess air such that the flame temperatures stay low. [3] Since the thermal NOx formation is strongly temperature dependent its formation can be limited by keeping the flame temperatures as low as possible. Moreover, in this approach premixing the fuel and the air before the combustion as opposed to the situation in the diffusion flames prevents also hot spots within the combustor where NOx can form. The combustor liner cooling

can have an important effect on the resulting combustor outlet temperature profiles. A variety of liner cooling methods are being utilized ranging from the film cooling to backside cooling. The trend in the cooling technology is towards the backside cooling, where the liner wall is cooled convectively by the cold, high velocity air stream on the other side of the wall. Even though the lean premixed combustion technology has clear benefits in terms of the NOx reduction and the uniformity of the temperature distribution, there are also issues related to stability and flexibility which might limit the application of this combustion technology for other areas. The lean operating character of the combustor brings in additional issues in terms of the flame stability at part loads. Reducing the fuel concentration to a combustor operating under lean conditions even at full load may result in the extinguishment of the flame if necessary adaptations are not carried out.

In aeroengine applications the combustion stability is a much bigger concern than it is in power generation applications. [4] Moreover, in aircraft engines much more variable load conditions are needed as opposed to land based gas turbines where the duty cycle is much more constrained. Under these conditions the lean premixed combustion might not be the most suitable technology to use. Because of this reason an additional low NOx generation combustor concept called the Rich-Burn, Quick-Mix, Lean-Burn (RQL) combustor was introduced in 1980's. This combustor has superior characteristics in terms of the combustion stability at varying operating loads and thereby preferred by some major aircraft engine producers. Moreover, there is a growing interest for this combustor technology for power generation applications as well due to their advantages in dealing with fuels of complex and varying composition.

The RQL combustion concept relies on the variation in the NOx formation depending on the fuel ratio shown in Figure 1.2. As shown, the NOx formation reaches a peak at about the stoichiometric conditions and sharply drops away from this point towards both the fuel lean and fuel rich conditions.
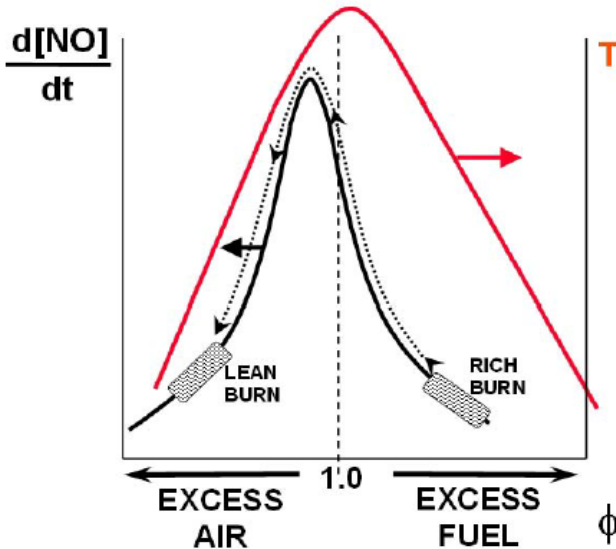
Figure 1.2 Nitric Oxide production versus the fuel equivalence ratio [4]

According to the NOx formation behavior shown, the combustor is divided into three zones as shown in Figure 1.3. In the primary zone, the fuel is burned under reach conditions. These rich conditions ensure the flame stability even at part loads because there is a very high margin to the lean conditions occurring in the lean premixed type combustors. Moreover, the low temperature level at the fuel rich conditions does not promote the NOx production. Downstream of this region excess air is injected from the walls in form of big jets which lead to lean conditions in the next combustor zone. In this zone the combustion under lean conditions ensures a low NOx formation as well in a similar strategy used in lean premixed combustion. Dividing the combustion process into two stages by burning the fuel once under rich and later on under lean conditions limits the peak temperature level and thereby the NOx formation is not promoted. And at the combustor outlet dilution holes are placed to reduce the temperature level and adjust the radial temperature profile in a way downstream components can withstand.
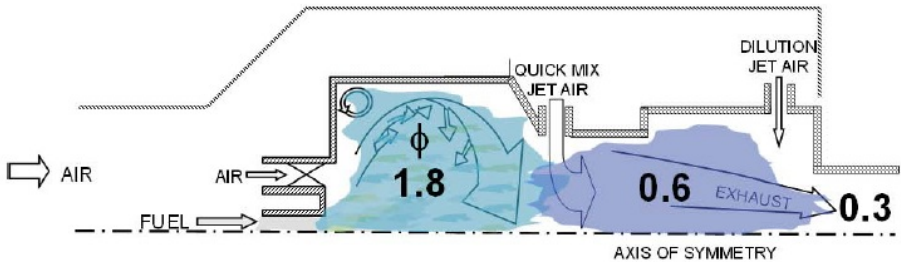
Figure 1.3 Rich-Burn, Quick-Mix, Lean-Burn Combustor with the fuel equivalence ratios at each stages of the combustor [4]

As opposed to the lean premixed combustor concept this concept utilizes from considerable amount of dilution air which offers a larger flexibility in terms of shaping the combustor outlet temperature distribution which can also have some benefits in terms of the aero-thermal performance of the HP turbines.

Apart from the combustion concept used combustors could also be classified according to their shapes. The two most frequently used combustor types are the can-annular and the full-annular combustors. Each of these shapes has their cons and pros which make one concept more advantageous for an application area and the other one for another. LeFebvre[5] and Odgers and Kretschmer[6] discuss the advantages of each of these design concepts. A can-annular combustor design is shown in Figure 1.4. In can-annular design the combustion takes place in separated containers called cans. They are placed in a common casing where air that is not entering into the cans are flowing through to cool the outside walls of the cans, called the liner, and also to dilute the hot air inside the cans with cold air from the compressor. In this design concept the cans can be tested stand alone as a unit of combustor since the interaction between the cans is rather weak which is an advantage in terms of cost of design. Also in case of damage the cans can be separately replaced which reduces the cost of maintenance. Another major design concept is the full-annular combustor shown in Figure 1.5. In full-annular combustors the fuel injectors are distributed on a ring around the annulus but they are positioned in a common liner where the interaction in-between the fuel-injectors is

stronger. Due to the more complex dynamics of this design they have to be tested as a whole which increases the cost of design of the combustor. However, they also offer considerable advantages such as weight reduction which is particularly important for the aeroengine applications. They also provide circumferentially a more uniform combustor outlet temperature distribution. Because of these advantages full-annular combustors started to be used in aeroengine application over the last years. In the evaluation of the full annular concept injectors distributed on multiple rings have also been developed which offers a low NOx level advantage at varying load requirements by switching on and off the injectors at different radii.
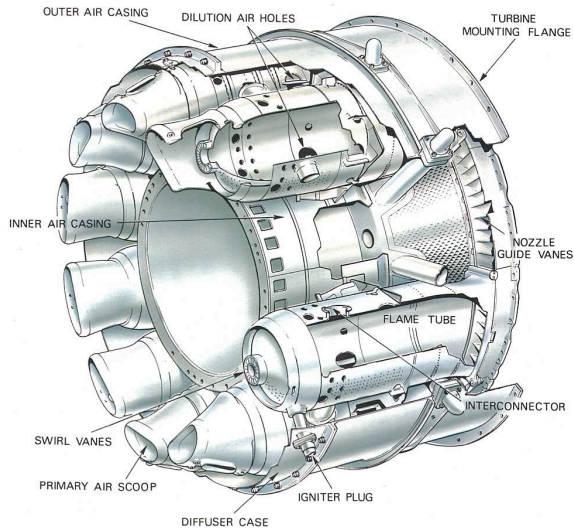
Figure 1.4 Can-annular (tubo-annular) combustion chamber [7]

On the other hand, for the land-based gas turbines the can-annular combustors are more frequently used mainly because of the ease of maintenance and no restrictions on weight.
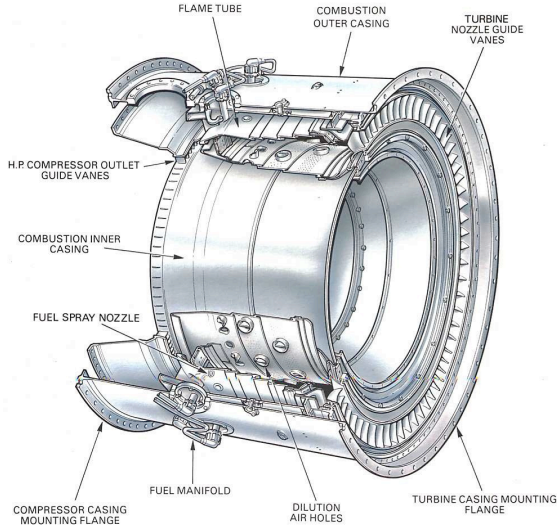
Figure 1.5 Full-annular combustion chamber [7]

1.2. Hot Streaks and Their Intrinsic Aerodynamics

Hot streaks are generated within the combustor chamber. There is a considerable variation in their intensities and shapes depending on the combustor type used which is mainly dictated by the field of application. Accordingly, in the literature hot streaks with different intensities and shapes have been considered. Povey and Qureshi [8] compared the different test rigs worldwide and the characteristics of the generated hot spots. In the very first experimental studies on the effect of hot streaks on the turbine Butler et. al. [9] have considered a circular shape hot streak with peak to free-stream temperature ratio of about 2. Over the years imposed regulations especially in the concentration of NOx levels led serious advancements in the design of the combustors resulting in a decrease in the intensities of the generated hot streaks. A recent temperature distortion generator has been developed by Povey and Qureshi [8]   taking the temperature non-uniformity observed downstream of a modern combustor as a basis. As in the very first hot streaks experiments also in this recent

study a circular shape hot streak has been considered but the intensity of the temperature non-uniformity being much lower.

After generated within the combustor, hot streaks migrate downstream and increase the heat load along their flow path. While hot streaks are convecting downstream, they not only get affected by the turbine aerodynamics but also show a clearly distinct migration pattern due to their intrinsic properties. A very fundamental principle which is directly applicable to understanding the effect of temperature non-uniformities on the turbine aerodynamics is raised by Munk and Prim [10]. According to that, non-uniformities in temperature distribution only do not alter the inviscid flow aerodynamics as long as the total pressure distribution is kept unchanged. What it is meant with this is that the Mach number distribution and the pressure distribution are not affected from the variation in the temperature levels of the streams. The main reasoning behind this principle is that the change in the temperature level of a fluid does not alter its momentum. On one side, the hot gas expands more and results in a lower density fluid but on the other side, this drop in the gas density is balanced by the increase in its convective speed due to the rise in the speed of sound with the rise in temperature level. This balance keeps the momentum level of the gas constant irrespective of its temperature level. The validity of this principle has been observed by Povey et. al. [2] within the first stage stator. As shown in their work introducing hot streaks upstream of the stator row did not change the inviscid stator aerodynamics. On the other hand, the loss generation mechanism is affected by the introduction of the temperature non-uniformities. Additional entropy is generated as a result of mixing of the two fluids with different temperature and velocity levels but this is beyond the scope of Munk and Prim [10] principle.

One of the first experimental studies on hot streak migration has been conducted by Butler et al. [9] in a single-stage, low speed rig with a circular hot streak introduced from a tube upstream of the stator. Seeding the hot air with CO_2 and measuring its concentration level downstream within the turbine, Butler et. al [9] experimentally showed for the first time that hot streaks impinge on the pressure side of the rotor blade and create preferential pressure side heating. They explained this flow behavior with the very fundamental Kerrebrock-Mikolajczak [11] effect. According to this effect, the difference in the absolute flow velocities between the hot

and the relatively cold surrounding streams create a difference in the relative flow angles within the turbine rotor passage. The difference in the absolute flow velocities downstream of the stator row is due to the Munk and Prim [10] principle which dictates that the Mach number distribution should be kept unchanged with the addition of temperature non-uniformities but results in a higher flow velocity for the hot streak due to the rise in the speed of sound level with the temperature. As a result of this, hot streaks always approach the turbine rotor blade with a higher relative flow angle compared to the surrounding stream and thereby impinge on the rotor pressure side. Previously, Kerrebrock-Mikolajczak [11] have observed a similar flow physics within the compressor rows. In their study about the migration pattern of the compressor stator wakes within the rotor, the velocity deficit in the stator wakes make them approach the rotor pressure side in the compressor.

The hot streak segregation observed by Butler et al. [9] has also been investigated numerically. The two dimensional studies of Rai and Dring [12] and Krouthen and Giles [13] did not correctly capture the heat load distribution observed in the experiment. On the other hand, the matching of the three-dimensional simulations by Dorney et al. [14] and Takahashi et al. [15] emphasized the importance of three-dimensional effects on hot streak migration.

Hot streaks also generate additional secondary flows within the rotating blade rows because they affect the relative total pressure distribution upstream of the rotor row. Depending on the severity of the temperature non-uniformity these secondary flows can have a considerable effect on the turbine aerodynamics. They enhance the mixing of the hot streak and affect the spanwise distribution of the hot fluid within the rotor row which might lead to failures at critical regions such as the rotor blade tip.

1.3. Turbine Aerodynamics and Its Interaction with the Hot Streaks

Imposed to the highest level of hot streak intensities and also being stationary the first stage stator blades are very severely affected by the temperature non-uniformities. Depending on the way the hot streaks

impinge on the stator the incident heat load and thereby the cooling requirements might change considerably. In a recent experimental study Povey et. al. [2] have investigated the effect of the hot streaks on the first stage stator heat load. They have considered two different circumferential positions of the hot streak relative to the stator and compared the resulting incident heat loads on the blade. In one of the cases the hot streak was impinging on the stator leading edge and in the other case it was heading to the middle of the passage. The results have shown that the pressure side heat load distribution was quite insensitive to the position of the hot streak. On the other hand, at the stator suction side there was a major 50% increase in the Nusselt number level when the hot streak was impinging the stator leading edge compared to the case when it was heading to the middle of the passage. The rise in the Nusselt number was concluded to be only due to the increase in the incoming gas temperature level and not in the local heat transfer rate which was shown before by Munk and Prim [10] that the temperature non-uniformities do not change the aerodynamics within stationary blade rows.

Even though their intensities are reduced within the stator passage hot streaks still have a very considerable effect on the rotor blade heat load. Moreover, the hot streak segregation mechanism that Butler et. al. [9] have experimentally observed prevents their effects to be averaged out due to the rotation of the rotor blade. Additionally, different from the stators the rotor blades have to cope with very high level of mechanical stresses. Combining all these aspects imposes a major challenge for the design of the rotor blades. So the effect of the hot streak on the rotor blade heat load has been investigated in great coverage in the literature. In a number of numerical studies the effect of the relative positions between the hot streak and the stator blade on the heat load of the rotor downstream has been investigated. Changing the circumferential position of the fuel injectors with respect to the stator blades is known as hot streak clocking. One of the first clocking studies has been conducted by Dorney and Burlet [16]. They have studied numerically the effect of two clocking positions on the rotor heat load; one with the hot streak at mid-passage and the other with the hot streak impinging on the first stage stator leading edge. It has been shown that impinging the stators by the hot streaks enhances their mixing and reduces their intensity downstream. Thereby, their effects on the rotor blade are alleviated especially on the pressure side. However, the reduction in the

rotor pressure side temperature is counterbalanced by the increase in the heat load on the stator especially at the leading edge and at the suction side as Povey et. al. [2] have shown. On the other hand, keeping the hot streaks in the middle of the stator passages keeps their intensities in a great extent due to the convection dominated flow pattern within the turbine and leads to more pronounced effects on the downstream rotor row. In this case the distinct migration patterns of the hot streaks within the rotor leads them to migrate to the pressure side and lead to excessive pressure side heating.

In a more recent study An et. al. [17] investigated numerically additional clocking positions in-between the two extremes that Dorney and Burlet [16] have studied before and analyzed the steady and unsteady heat load on the stage. Although being an effective way of distributing the heat load between the rows and thereby considered widely in the literature, fuel injector – stator clocking has a serious limitation requiring integer stator – fuel injector ratios. Nevertheless, this is only very rarely the case [2], which makes this method quite inapplicable.

When hot streaks impinge on the rotor pressure side they also interact with the tip leakage flow which is the most dominant secondary flow feature within the HP turbine due to their low aspect ratio. In a numerical study Dorney et al. [18] investigated the interaction between the hot streak and the tip leakage flow where they have compared the radial spread of the hot fluid on the rotor pressure side for two different simulations. In one of the simulations the tip clearance gap was included and in the other one it was excluded from the computational domain. Simulations including the tip clearance gap showed a considerable higher radial spread of the hot fluid on the rotor pressure side compared to the simulations excluding the rotor tip gap. This result emphasized the importance of including the tip clearance gap within the HP turbine simulations because of the dominant effect of the tip clearance flow on the estimation of the incoming heat load.

Unlike in stationary blade rows hot streaks induce secondary flows within the rotor passage, altering the streamline patterns thereby and migrate spanwise to the periphery of the rotor blade. Prasad and Hendricks [19] have shown that by adjusting the vortexing of the stator upstream the spanwise migration of the hot streak within the rotor passage can be manipulated as required. Using a blade stacking that leads to stator exit

flow angle distribution decreasing from hub to casing they have considerably reduced the radial transport of the hot streak towards the rotor blade tip as opposed to the case with uniform flow angle distribution at the stator exit. However, in their study they have used a low speed turbine geometry where the compressibility effects were not pronounced. So application of this study on real engines with compressibility effects should be done with care.

Three-dimensional design features are not only limited with the blades themselves but are even applied at the endwalls in form of the non-axisymmetric bumps especially within stators. In various experimental studies in linear and annular cascades non-axisymmetric endwall profiling has been proven to reduce the endwall secondary losses by decreasing the intensities of the passage vortices at the endwalls. The passage vortices are triggered by the interaction of the incoming boundary layer with the airfoil leading edge and are diverted downstream by the cross passage pressure gradient accumulating them at the blade suction side. It has been shown that reducing the cross-passage pressure gradient by introducing bumps at the endwalls reduced the intensities of the passage vortices and their associated losses thereby. In a recent experimental study conducted at LEC's research turbine facility "LISA" Schuepbach et. al. [20] have carried out time resolved measurements downstream of the first stage stator of the one-and-half stage turbine similar to the HP turbines in terms of geometry and loading. They have experimentally observed a major reduction in the intensities of the passage vortices and also in the wake just by profiling the endwalls of the stator accordingly. The resulting rise in efficiency was about 1% which is very considerable. The endwall design procedure along with the numerical studies has been carried out by Germain et. al. [21] Moreover, different from the three-dimensional blading they can also be applied within rotating blade rows since they do not introduce additional mechanical loads on the blades. However, in case of the unshrouded rotor blades as in the most of the HP turbines they could only be applied at the hub endwall. On the other hand, in the shrouded rotor blades such as in the low pressure turbines they can be applied on both endwalls. Jenny et. al. [22] have conducted a very detailed experimental and numerical study on the effect of the endwall profiling on the performance of the very highly loaded, shrouded, low pressure turbines in presence of the rim seal cavity purge flows. Due to their favorable aerodynamics in reducing the secondary

flow losses they are increasingly becoming a more common design feature in modern gas turbines. However, as they change the stator endwall aerodynamics the hot streak migration pattern might be affected as well. Moreover, due to the low aspect ratio design of the stators in HP turbines their effects might be considerable even at a major portion of the blade span.

Unsteadiness in the flow also affects the hot streak migration. In this regard the stator-rotor interaction as the most dominant unsteadiness present has been considered by Shang and Epstein [23] In their numerical work they have used an unsteady Euler solver to simulate the hot streak migration imposed to the unsteadiness by the rotor rotation. The unsteady rotor potential field led the hot streak to wobble at the interface which was later on observed experimentally by Jenny et. al. [24] conducting time resolved temperature measurements at the interface. As Shang and Epstein [23] have shown in their numerical work when time averaged this unsteady wobbling behavior leads to circumferential non-uniformities in temperature distribution upstream of the rotor row which at the end affects the time averaged heat load distribution on the rotor blades. So the blade ratio between the stationary and rotating rows affects the unsteadiness in the flow and thereby the thermal load on the rotor blade.

1.4. High Pressure Turbine Aero-Thermodynamics

Modern HP turbines operate already at temperatures exceeding material temperature limits. However, the demand on more efficient gas turbines forces the designers to increase the turbine inlet temperature level even further which makes the turbine cooling design more critical than ever. Figure 1.6 shows the trend in the turbine inlet temperature levels over the years and how the cooling technology is evolved to keep up with the increasing temperature levels.

Within the HP turbine the rotor blades are also subject to very high mechanical stresses in addition to the thermal stresses that they have to deal with. The combustor outlet radial temperature profiles are adjusted in a way considering not only the mechanical stress distribution on the rotor blade but also the cooling requirements of the endwalls. Over the years the

positive trend in the turbine inlet temperature levels did not show up in the level of the temperature non-uniformity. Quite the opposite with the advances in the combustor technology the level of the non-uniformity smoothed down. However, less peaky radial temperature profiles meant higher heat loads at the endwalls as well.
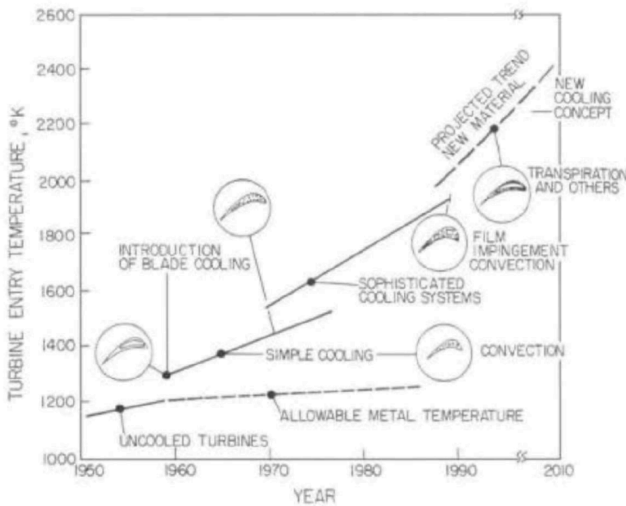
Figure 1.6 Turbine Inlet Temperature Variation over Recent Years and the cooling technologies adapted enabling the increase in the turbine inlet temperature level [25]

The HP rotor blade tip is also severely affected by the flattening of the radial temperature profiles. Imposed to highly vortical flow field the blade tip area is subjected to one of the highest convective heat transfer rates on the entire rotor blade. Due to the harsh conditions the design of the rotor blade tips are dominated by the heat transfer considerations rather than the aerodynamics. Even though shrouded turbine blades offer higher aerodynamic component efficiency, the difficulty in their cooling and the associated cost on the thermodynamic performance should have dominated their component efficiency benefits such that they are not used in modern HP turbines.

But still even though heavily cooled quite frequently local material degradation due to overheating are observed at the blade tip. Bunker [26] states that one third of all the rotor blade failures occurs at the tip region which clearly shows the severity of the conditions faced with. Figure 1.7 shows the material loss at the squealer tip of an HP turbine blade due primarily to oxidation effects. Main material loss is observed at the suction side rim at about the middle of the blade cord. At the pressure side rim and in the tip cavity bottom additional cooling holes were placed to cool the blade tip. However, even with these additional measures the integrity of the blade tip could not be preserved with operation. And the change in the aerodynamics due to the change in the tip geometry usually increases the degradation rate as well, and after some time the blade tips have to be repaired when the loss in the efficiency due to the burning of the blade tips goes beyond being tolerable.

The HP rotor blade tip has a profound influence on the aero-thermal performance of the HP turbines and thereby on the overall engine efficiency. There are a variety of recent experimental and numerical studies that have investigated the aerothermal performance of the rotor blade tips in HP turbines. Most of these studies were conducted in linear cascades. Bunker et. al. [27] have conducted an experimental study using a linear cascade where the heat transfer map of the complete rotor tip was measured for the first time. With its flat tip design the rotor was representing the geometry of the first stage rotor of a modern gas turbine for power generation. In their experimental study they have identified a characteristic central sweet spot of low heat transfer which extends into mid-chord region and towards the suction side. They also have shown that adding radius to the geometry of the tip edge along the perimeter led to 10% increase in the heat transfer coefficient which is attributed to the increase in the tip leakage mass flow. In the continuation of the experimental work Ameri and Bunker [28] have also conducted RANS simulations on a single rotor row using the two-equation Wilcox [29] k-ω turbulence model. Their predictions of heat transfer showed a good comparison with the measurements capturing the sweet spot that was measured at the experiments. Moreover, adding a radius to the edge along the periphery of the blade tip prevented the formation of a corner vortex and increased the level of agreement between the predictions and the measurement thereby.
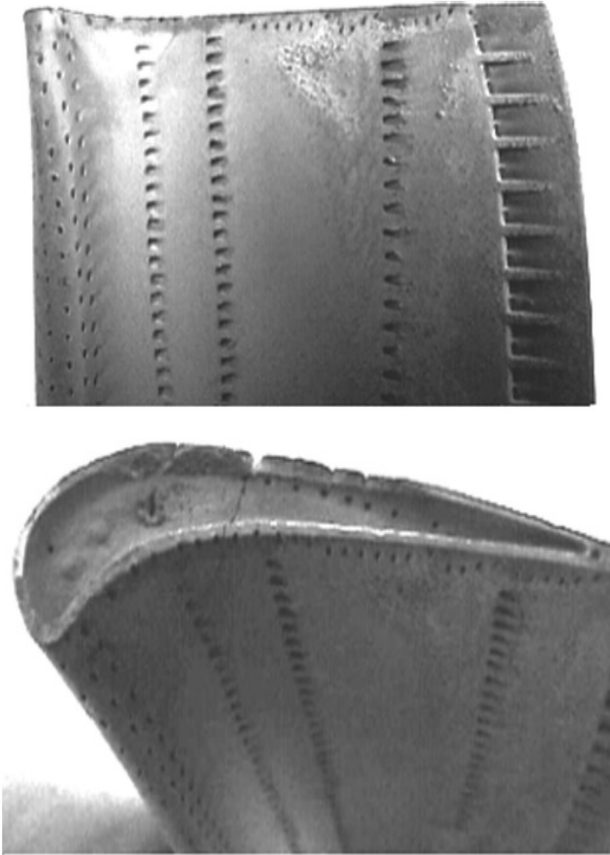
Figure 1.7 Tip material loss primarily due to oxidation after unspecified hot exposure time in service [30]

In HP turbines usually unshrouded rotor blades are utilized because of the ease of the cooling. Within unshrouded turbine geometries there are different blade tip designs which can be grouped into two main categories such as flat and recessed. In a numerical study by Ameri et. al. [31] they have compared the aero-thermal performance of the recessed blade tips with two different recess cavity heights with the one of the flat tip design. With respect to the flat tip the recessed tip design with a cavity height of

3% of the blade span reduce the tip leakage mass flow by 14 %. However, no significant increase in the aerodynamic efficiency was obtained. Moreover, especially high heat transfer rates were observed where the cavity vortices exit the recess cavity. A deep experimental and computational study on the aerothermal performances of the different unshrouded blade tip geometries have been published by Mischo et. al [32] where the measurements were conducted in a real rotating rig representative of a HP turbine. In complementary to the experimental work unsteady, multi row CFD simulations were also conducted. They have showed that including the recess geometry at the blade tip increases the sealing performance by the introduction of the additional vortical structures within the cavity. In addition, a new optimized recess geometry has been developed which reduces the heat transfer rate especially at the recess cavity wall compared to the conventional recessed blade tip designs.

The heat transfer coefficient is mainly dictated by the highly three-dimensional aerodynamics in the near tip region. The other factor driving the heat transfer is the gas temperature. The hot streak migration in the HP turbine is a convection dominated phenomenon. In their early numerical work Shang and Epstein [23] have used even an Euler solver to investigate the effect of the stator-rotor interaction mechanism on the hot streak migration physics. Even though their intensities are reduced over the years the hot streaks present at the turbine inlet might impinge on the rotor blade tip, drive up the gas temperature and enhance the heat load thereby. For components such the rotor blade tips operating under very harsh conditions slight changes in the gas temperature level might have an important effect on the overall efficiency of the engine and their life time and thereby to the operating cost of the engine. This is why the hot streak migration pattern especially to the critical regions in the turbine such as the blade tip area has to be taken into account.

1.5.   Use of CFD in the Design of the HP Turbines and Source of Errors in Turbomachinery CFD

The design of the turbomachinery is a complicated and costly process. The HP turbine as one of the most challenging component to design requires intensive use of CFD, empirical data and as well as very expensive test rig

measurements. Over the years with the advances in the hardware and software technology the use of CFD in the design process is considerably increased. Today CFD is used from the level of single blade geometry optimization up to the level of multi-stage aerothermal analysis of the HP turbines. However, the modeling of the complex flow within the HP turbine is numerically very challenging. On one side the flow itself is highly three-dimensional, unsteady and exhibits very diverse scales and on the other side the error margins are very low. Being subject to very high heat loads even a few degree difference in the blade surface temperature prediction can have big consequences on the design of the whole engine. Even though the advances in the computer technology enabled the designers to conduct more sophisticated CFD simulations still there are issues that are seriously limiting the accuracy of the CFD solvers. The designers should be aware of these limitations and use the CFD wisely.

Denton [33] explains the main sources of errors in the turbomachinery CFD by giving concrete examples from the literature. In Figure 1.8 the main sources of the errors related purely to the numerics itself are listed. As the problem is discretized and solved iteratively on a generated mesh, the mesh itself has a crucial role on the accuracy of the results. It requires quite a bit experience to generate high quality but also computationally affordable meshes. Distortions in the mesh in the form of skewness, high aspect ratio, high expansion ratio directly affect the accuracy of the solver. The solver can reach only the theoretical order of accuracy provided the mesh is uniform. Also the type of the mesh generated has a major influence on the accuracy of the solution as well. Even though they are more time consuming to generate today mostly the multi-block, structured grids are preferred over the unstructured ones due to their favorable characteristics reducing the numerical diffusion. Even though numerical diffusion is very important for the stability of the solvers it also artificially smears out the results and can decrease the accuracy considerably. Mesh refinement studies are conducted especially to evaluate the effect of the numerical diffusion on the accuracy of the results. However, in real application it is never the case to conduct proper grid refinement studies where the mesh is refined in all the three dimensions since the associated computational cost is too high to afford. So the need for the numerical schemes with minimum amount of numerical diffusion is immense. One of the main outcomes of

the "Far-Wake Workshop" taken place in Marseille in 2008 points out the importance of the numerical dissipation effects.

"Numerical dissipation effects due to numerical scheme and mesh discretization can be more important than the selected turbulence model for this kind of low-mach application"

Grid	Numerical Diffusion
• Skewness • Expansion Ratio • Aspect Ratio • Structured vs. Unstructured	• Inherent in the numerical scheme due to the truncation error • Via additional numerical smoothing; e.g in presence of shocks
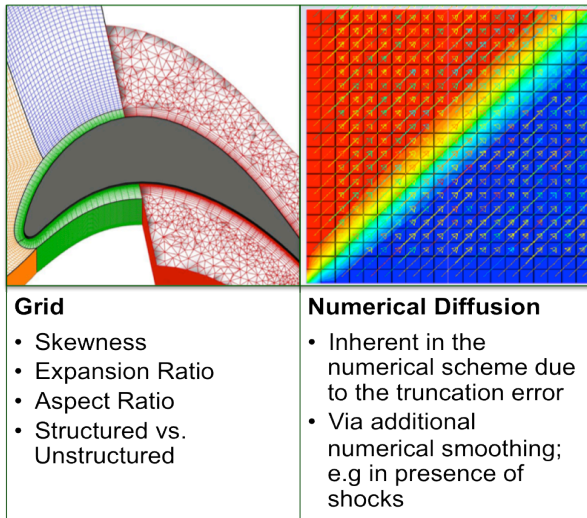
Figure 1.8 Main sources of the errors in CFD related to the numerics itself

In addition to the errors associated purely with the numerics there are also errors related to the modeling of the problem. As listed in Figure 1.9 these are due to the inaccuracies of the incorporated models and due to the uncertainties about the geometry and also about the boundary conditions imposed. Errors related to the uncertainties in the geometry are quite considerable. The HP turbine blades are exposed to very high heat loads which can result in changes in the blade geometry during the course of operation. For example; small degradations on the rotor tip geometry can alter the flow field considerably. Surface properties such as roughness play a major role in the heat transfer to the blades. However, mostly very few are known about the exact surface properties and also about their modification during the course of operation.

Assigning accurate boundary conditions are fundamental for the quality of the simulations. However, the presence of accurate and high resolution measurement data of the upstream flow conditions is rarely the case. For example, measurement of the flow conditions upstream of the HP turbine is very difficult to conduct. Accordingly, there are uncertainties associated especially with the temperature boundary conditions the HP turbines are faced with. At LEC a particular importance is given to the measurement technology. The probe technologies developed within the lab are continuously used in the test rig measurements to deliver high quality and time resolved measurement data that can be used as boundary conditions and also for the validation of the simulation results.

Models	Geometry	BC's
• Turbulence Model • Wall Functions • Mixing Plane – steady flow assumption • Periodicity assumption • .	• Modifications during operation; e.g rotor tip geometry • Roughness • Cavities	• Absence of experimental data • Measurement Uncertainity
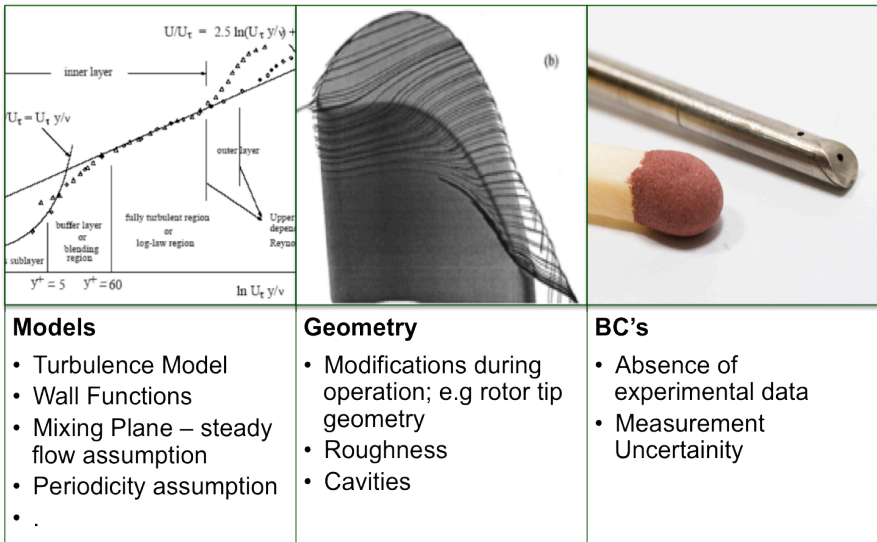
Figure 1.9 Sources of the errors in CFD related to the modeling of the problem

The incorporated models within the CFD solvers are a major source of error. The models are only required due to the unavailability of the computational resources. Major modeling approaches quite frequently used in the turbomachinery CFD are listed in Figure 1.9. [33] The advances in the computer hardware and software technology enabled to reduce the level

of modeling involved in the calculations or to make use of more elaborate models. For example; over the years the two-equation turbulence models replaced the more simplistic algebraic and the one-equation turbulence models. Especially for the multi-row turbine simulations the two-equation models have a major advantage of modeling the convection of the turbulence between the blade rows that is particularly important for the mixing of the upstream blade wakes and secondary flow features. In addition of its effect on the turbine aerodynamics, turbulence also has a primary effect on the heat transfer on the blade surface which is the most critical factor in the design of the HP turbines. Uncertainties about locating the position of the boundary layer transition can severely affect the accuracy of the blade metal temperature predictions. [8] The surface properties such as roughness is very effective in the wake profiles and in the losses generated.[34][35][36]However, they are mostly not very accurately known which leads to a source of error related to the uncertainties in the geometry.

The flow inside the turbine is highly unsteady and the major unsteadiness is due to the passing by of the rotor blades in between the stationary blade rows. This unsteadiness has a major influence on the flow physics of both the downstream and also the upstream rows. The mixing plane models kill the unsteady interaction between the rows and can seriously deteriorate the accuracy of the computation. However, the mixing plane approach continues to be widely used especially in the industry. The computational cost of unsteady simulations is one order of magnitude higher compared to the steady simulations carried out with the mixing plane approach which is still too high to afford in the design process. Also errors associated with the periodicity assumption are very considerable. Even though the blade counts have an integer ratio there are flow features inside the turbine which do not show the same periodicity pattern. Especially, in the simulations where the cavities are included imposing a periodicity condition will damp all the non-periodic flow features. Also most of the time the blade counts are not in integer ratio. And in this case the blade geometries are scaled in order to reach the most affordable integer ratio between the blade counts. This simplistic modeling approach also increases the errors in the predictions.

With the further improvements in the computer technology less and less modeling may be involved in the simulations which would directly affect

the accuracy of the simulations. Looking from this perspective parallel processing seems to continue to be a key issue for the CFD development.

1.6.   Parallelization Paradigms

The OpenMP approach offers the programmers a simple and flexible interface for parallelization. It is usually advantageous in terms of code development because the memory management is transparent to the user and is dealt completely by the programming model. As a disadvantage however, it can only be used on shared memory multi-core architectures. Moreover, if the code is divided into many small subroutines sharing the computational load the scalability of the code drops sharply. On the other hand, the MPI approach is a much more elaborate way of parallelization since the memory management has to be explicitly dealt by the developer. But, the parallelization is not limited to shared memory architectures and usually shows a better scalability compared to OpenMP approach if the load balancing between the processors is efficiently done.

Recently, a complete new parallel programming approach has emerged which makes use of the graphic cards which are originally developed for the computer games. The steep increase of the computational power of the GPU's (Graphical Processing Unit) in recent years put the modern GPU's much ahead of the many core CPU's. Figure 1.10 compares the computational power of Nvidia GPU's with the multi-core CPU's over the last years. Moreover, the increase in the computational power is also supported by the rise in the memory bandwith as shown Figure 1.11. With these properties the graphic cards have become an ideal candidate for scientific computing. Later on Nvidia released a relatively easy programming model called CUDA to spread the use of the graphic cards in the scientific computing community. One of the first works on the GPU parallelization of an in-house CFD code used in turbomachinery applications was carried out by Brandvik and Pullan [37]. The code has a second order accuracy in space utilizing a central discretization and the Scree scheme was used for the explicit time integration. A rather simplistic smoothing algorithm was applied that was making use of only second order artificial damping and also a simple algebraic mixing length turbulence model was implemented. Using single precision accuracy on a single G80

series GPU they have obtained a very impressive speed up rate of about 19x versus a quad-core CPU. Moreover, the scalability of the code up to 16 GPU's was almost linear. The very high speed up rate that they have obtained was also due to the structured data storage format of the code which enabled a very high memory bandwidth. However, in most of the commercial and in-house codes an unstructured data format was preferred because of the additional flexibility that it offers. Deploying these codes to GPU efficiently requires more effort and the performance might not be as high.
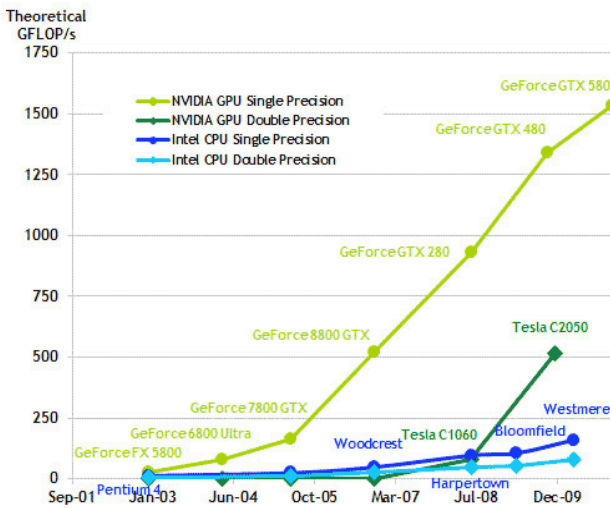
Figure 1.10 Comparison of the Flop-rates for the Nvidia GPU's and Intel multi-core CPU's over the last years

In a more recent study using the Nvidia's CUDA programming model Phillips et. al. [38] have parallelized their in-house URANS solver based on the Ni-Lax Wendroff [39] scheme and making use of the two-equation Wilcox [29] k-ω turbulence model. This solver runs on the multi-block, structured grids where the blocks are connected via an unstructured type of block connectivity which makes the implementation harder to deal with in terms of the memory management. They also have conducted their calculations with double precision accuracy and obtained an order of

magnitude speed-up on a single Tesla "Fermi" class GPU versus a single CPU core. This was the first graphic card chip developed by Nvidia with high double precision computing capability and utilizing of a memory cache and thereby designed for the scientific computing field. More recently directive based high-level programming models are released that can automatically generate the GPU kernels and reduces the effort of GPU programming thereby. However, the performance of these tools are not well known.
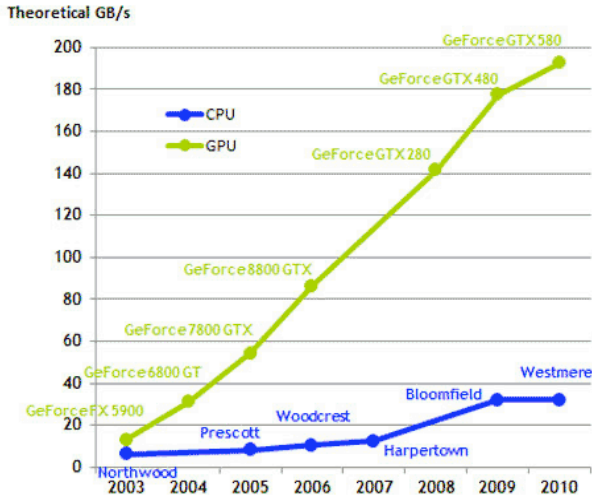
Figure 1.11 Comparison of the memory bandwith for the Nvidia graphic cards and Intel multi-core CPU architecture over the last years

The use of the parallel processing enabled to simulate more complex scenarios with less modeling. For example, the cost of the unsteady, multi row RANS simulations has been reduced considerably over the recent years. However, the post-processing of the huge amount of unsteady flow data is becoming an issue where the particle tracking tools might offer considerable benefits. Lagrangian particle tracking is being used as a post-processor tool in the detailed flow field analysis of the turbine simulations. Tallman and Laksminarayana [40] have conducted steady, single row

simulations with different tip clearance heights which they used to compare the intensities of the forming tip leakage vortices, the leakage mass flows and their associated losses via a steady Lagrangian particle tracking tool.

1.7. Integrated Combustor-Turbine Design Approach

The temperature non-uniformities at the combustor outlet have a profound effect on the engine performance, affecting the cooling requirement of the turbine and thereby influence the cycle performance. When the relatively high temperature gas referred as hot streak convects downstream it increases the incident heat load along its flow path considerably which the cooling designers have to take into account. Designing the turbine cooling with respect to the peak temperature puts a penalty on the thermodynamic cycle performance of the engine on the other hand; inadequate cooling might shorten the service periods of the engine considerably and thereby increase the operating cost of the engine. So for an optimum cooling design a good level of knowledge about the combustor outlet boundary conditions and their migration behavior within the turbine is very crucial.

The radial temperature profile downstream of the combustor is the key parameter affecting the spanwise heat load distribution on the HP turbine components. Because of the high mechanical stresses that the rotor blades have to face with, the way the heat load is distributed along the blade span is far more critical for the rotor blade than it is for the stator. Contrary to the mechanical stress distribution the thermal stresses do not decrease towards the tip of the rotor blade. The rotor blade tip area is imposed to highest convective heat transfer rates within the rotor passage [30]. Moreover, the effectiveness of the cooling techniques is relatively low at that region. This is why their designs are mostly dictated by the heat transfer considerations rather than local aerodynamics. The migration of the hot streaks to the rotor blade tip also makes the situation even worse increasing the local gas temperature one of the main factors driving the heat transfer rate. Even though they are very heavily cooled quite frequently local degradation on the rotor blade tip geometry is observed increasing the leakage mass flow with time and decrease the turbine efficiency which is usually monitored with the EGT margin of the engine.

So the proper adjustment of the radial temperature profiles has a critical role for the rotor blade cooling design and its aero-thermal performance and its life time. However, the flow inside the turbine is never two-dimensional. Both the advanced blade design concepts, non-axisymmetric endwall shapes and also the secondary flows resulting from the temperature gradients within the hot streaks promote the three-dimensionality of the flow which might have serious drawbacks for the rotor blade if not taken into account. As a result of this three-dimensional flow field even the circumferential temperature gradients downstream of the combustor might also be very influential on the spanwise heat load distribution on the rotor blade. In the combustor framework there might be multiple ways of manipulating the circumferential temperature distribution.

Integrated combustor – turbine design approach aims to take various aspects affecting the hot streak migration into account and apply the necessary modifications on the combustor framework that would result in a more beneficial temperature distribution for the aero-thermal performance of the HP turbines, the life time of its components and the engine's overall efficiency as well.

1.8.   Objectives of the Current Work

In this numerical study the hot streak migration physics within the turbine is investigated conducting unsteady RANS simulations and utilizing the unsteady particle tracking tool to analyze the unsteady data. For the numerical study the inlet boundary conditions are taken from the time resolved flow field and temperature measurements conducted in LEC's axial research turbine facility "LISA" equipped with a hot streak generator to simulate the effect of the temperature non-uniformities downstream of the combustor. The numerical flow field predictions are validated with the measurements conducted downstream of the turbine. The main objectives of this study can be summarized as follows.

- • Investigate the hot streak migration pattern within the turbine stage using the unsteady particle tracking tool in conjunction with the experimentally validated unsteady RANS simulations

- Understand the hot streak migration physics and evaluate the interaction with the main turbine aerodynamics

- Accordingly propose a practically applicable combustor outlet temperature profile that would reduce the heat load on the rotor tip

- Test the effect of that both on conventional turbine geometries and also on the recent aerodynamic designs such as endwall profiling

The aspects of the problem that are covered in this thesis are summarized in Figure 1.12.
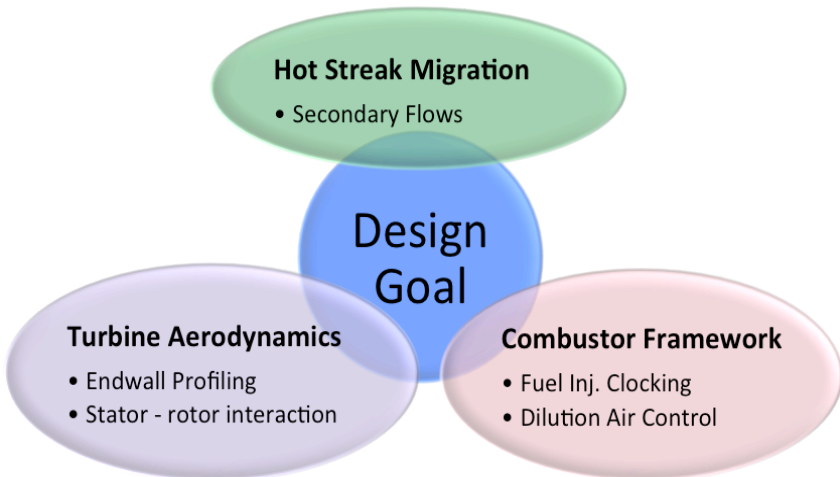
Figure 1.12 The schematic of the present research showing the different aspects of the problem affecting the combustor outlet temperature distribution

This numerical study has been conducted completely with the in-house CFD tools and one of the main objectives of this work is also to increase their capabilities in terms of both accuracy and productivity. Regarding the accuracy the modeling of the viscous effects is addressed. Accurate modeling of the viscous effects is crucial for the prediction of the

aerodynamic performance of the turbines. In RANS simulations one main source of diffusion is the turbulence itself. The effect of the turbulence on the mean flow is modeled using the eddy viscosity approach. In this regard the accuracy of the turbulence models are very effective on the overall accuracy of the simulations. The second important source of diffusion is purely numerical. To ensure the numerical stability in high Reynolds number flows a certain level of numerical diffusion is required. Algorithms that can locally regulate the level of artificial diffusion can improve the solution accuracy substantially. However, having a code that is very accurate may not be useful if the long run times are limiting the use of it. In this aspect parallelization is a key issue in increasing the productivity of the solvers. To summarize, the following aspects of the solver are dealt in this thesis.

- Accurate modeling of the diffusion processes (numerical and physical)

- Increasing the speed of the solver utilizing the state of the art parallel programming approaches to allow design optimizations

2. Numerical Methods

In this numerical work only the in-house developed tools have been used. LEC's in-house CFD toolset consists of the following tools.

- Multi-block, structured grid generator "Meshbound"
- Compressible URANS solver "MULTI3"
- Unsteady particle tracking tool "UNS-TRACK"
- Commercial post-processing tools such as Tecplot

The turbine geometries studied in this work are meshed via the multi-block, structured mesh generator "Meshbound". Thanks to its built-in blocking structure high quality, multi-block meshes can be generated even for the rotor blades with complicated tip geometries. The in-house 3D, compressible URANS solver "MULTI3" has being extensively used in the turbomachinery research within the LEC. Through the course of this study the capabilities of the solver has been greatly increased. The implementation of the two-equation k-ω turbulence model increased the solver's accuracy especially for the multi-row simulations where the turbulence needs to be transferred in between the blade rows. Particular effort is invested into the reduction of the artificial numerical diffusion. Numerical diffusion can artificially smear out the flow features and decrease the solution accuracy considerably. However, efforts in increasing the accuracy of the solver are worthless if the rise in the computational cost is not balanced by the increase in the computational power. In this regard the latest technological advances in terms of parallel programming are followed. The code has been parallelized using the OpenMP approach and can run on the modern multi-core CPU's. Recently the GP-GPU (general purpose GPU) programming has emerged as a new approach in the scientific computing and has gained a big popularity because of the exceptional performance modern GPU's can offer. Following the same trend the solver has been totally modified in order to benefit from this latest hardware technology. Even though parallel computing reduced the cost of conducting unsteady, multi-row simulations the difficulty in analyzing of

the very large amount of unsteady data still remains. In this regard an unsteady particle tracking tool has been developed which greatly increases the understanding about the migration patterns within the turbine stage.

2.1. Multi-Block, Structured Grid Generator "Meshbound"

In this numerical study all the meshes used have been generated via the in-house developed grid generator "Meshbound". Very detailed explanation of its features can be found in the work of Mischo [41]. Each blade passages are meshed separately via a multi-block strategy using the blade cuts as the input of the geometry data. Later on the blocks inside the mesh are merged to build a single block mesh that is fed into the solver in an unstructured data format. Finally, the separate meshes of each blade passage are merged to form a multi passage and multi row mesh. In order to decrease the mesh irregularities at the junction points of the blocks within the mesh a smoother has been recently developed. The smoother is based on the Laplacian operator [42] to regularize the mesh away from the blade surfaces since there the mesh is constraint by the geometry. Figure 2.1 and Figure 2.2 show constant radial cuts of the multi-block mesh through the rotor blade tip clearance section before and after applying the mesh smoothing respectively. As shown, the mesh shown in Figure 2.2 became more uniform especially at the block connection points and as well as at some other regions like the blade trailing edge.
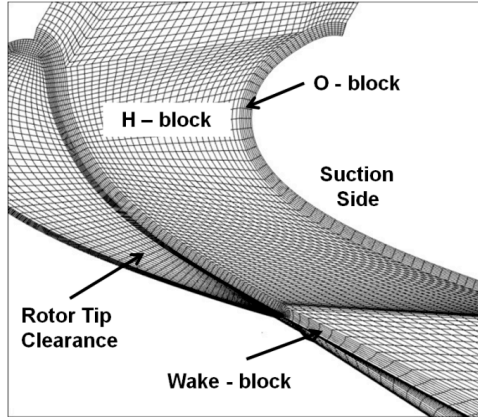
Figure 2.1 The multi block structured mesh at a section through the rotor blade tip gap (before applying the mesh smoothing)
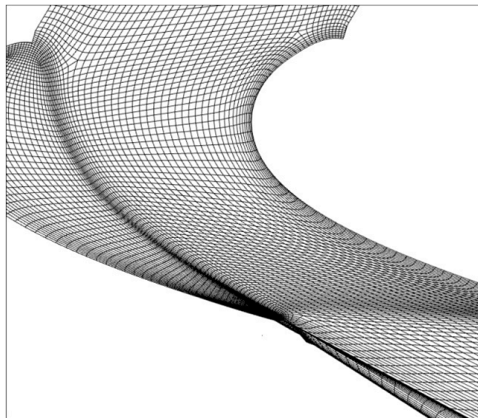
Figure 2.2 The multi block, structured mesh at a section through the rotor blade tip clearance (after applying the mesh smoothing)

2.2. Compressible URANS Solver "MULTI3"

In this numerical study the in-house URANS solver "MULTI3" has been used. The solver uses the Ni-Lax-Wendroff explicit time-marching

algorithm developed by Ni [39] to solve the unsteady, compressible RANS equations offering a second order accuracy both in time and in space.

The time dependent and three-dimensional Navier-Stokes equations are written in conservative form as

$$\frac{\partial Q}{\partial t} + \frac{\partial F_{invisc}}{\partial x} + \frac{\partial G_{invisc}}{\partial y} + \frac{\partial H_{invisc}}{\partial z} + \frac{\partial F_{visc}}{\partial x} + \frac{\partial G_{visc}}{\partial y} + \frac{\partial H_{visc}}{\partial z} = 0$$

Eq 2.1

The state vector is defined as

$$Q = \begin{pmatrix} \rho & \rho u & \rho v & \rho w & \rho E \end{pmatrix}^{T}$$

The inviscid and viscous flux vectors are given as

$$F_{invisc} = \begin{pmatrix} \rho u \\ \rho u^2 + P \\ \rho uv \\ \rho uw \\ \rho uH \end{pmatrix}, \quad G_{invisc} = \begin{pmatrix} \rho v \\ \rho uv \\ \rho v^2 + P \\ \rho vw \\ \rho vH \end{pmatrix}, \quad H_{invisc} = \begin{pmatrix} \rho w \\ \rho uw \\ \rho vw \\ \rho w^2 + P \\ \rho wH \end{pmatrix}$$

$$F_{visc} = \begin{pmatrix} 0 \\ -\tau_{xx} \\ -\tau_{xy} \\ -\tau_{xz} \\ -\tau_{xx}u - \tau_{xy}v - \tau_{xz}w - q_x \end{pmatrix}, \quad G_{visc} = \begin{pmatrix} 0 \\ -\tau_{xy} \\ -\tau_{yy} \\ -\tau_{yz} \\ -\tau_{xy}u - \tau_{yy}v - \tau_{yz}w - q_y \end{pmatrix}, \quad H_{visc} = \begin{pmatrix} 0 \\ -\tau_{xz} \\ -\tau_{yz} \\ -\tau_{zz} \\ -\tau_{xz}u - \tau_{yz}v - \tau_{zz}w - q_z \end{pmatrix}$$

The pressure is calculated using the ideal gas law.

$$P = (\gamma - 1)\left[\rho E - \frac{1}{2\rho}\left((\rho u)^2 + (\rho v)^2 + (\rho w)^2\right)\right]$$

Cell Vertex Discretization :

The time dependent Navier-Stokes equations are discretized using the Ni's [39] Lax-Wendroff scheme for the inviscid fluxes and the central differencing for the viscous fluxes. According to the Ni's cell vertex finite volume scheme the state vector **Q** is stored at the cell vertices. The algorithm is suitable for unstructured meshes but for simplicity the discretization procedure is explained for the structured and two-dimensional mesh shown in Figure 2.3. The Lax-Wendroff scheme is derived from the second order Taylor series expansion of the state vector **Q** in time. Substituting the inviscid fluxes for the time derivatives, the state vector **Q** at the next time step can be approximated as

$$Q^{n+1} \approx Q^n - \Delta t\left(\frac{\partial F_{invisc}^n}{\partial x} + \frac{\partial G_{invisc}^n}{\partial y} + \frac{\partial H_{invisc}^n}{\partial z}\right) - \frac{\Delta t}{2}\left(\frac{\partial}{\partial x}\Delta F_{invisc}^n + \frac{\partial}{\partial y}\Delta G_{invisc}^n + \frac{\partial}{\partial z}\Delta H_{invisc}^n\right)$$

where

$$\Delta F^n = \Delta t\frac{\partial F}{\partial t}, \;\; \Delta G^n = \Delta t\frac{\partial G}{\partial t}, \;\; \Delta H^n = \Delta t\frac{\partial H}{\partial t}$$

The change in the state vector is the sum of the contributions resulting from the first order and the second order time derivatives. The change in the state vector due to the first order time derivative is calculated on the primary cells shown by the solid lines in Figure 2.3. The resulting residual at the cell center is then distributed to the nodes at the cell vertices. Secondary cells are shown with the dashed lines in Figure 2.3 where the change in the state vector due to the second order time derivative is directly calculated on. Adding the first order and the second order contributions the overall change in the state vector can be calculated.
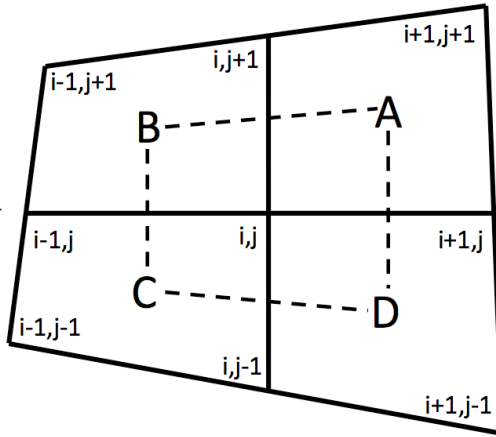
Figure 2.3 Two-dimensional, structured mesh; primary cells shown in solid lines and the secondary cells are shown in dashed lines

The inviscid flux contribution of the cell A to the residual of the cell vertex (i,j) can be calculated as

$$
\delta Q_{(i,j)A,invisc} = \left(\frac{\Delta t}{V}\right)_{i,j}\left\{-\frac{1}{4}\sum_{f=1}^{4\,faces\,of\,cell\,A}\left(\overline{F_{invisc}}S_x + \overline{G_{invisc}}S_y\right)_f\right\} -
$$

$$
\left(\frac{\Delta t}{V}\right)_{i,j}\left\{\frac{1}{2}\left(\begin{array}{c}\Delta F_{invisc}\\\Delta G_{invisc}\end{array}\right)_A \cdot \frac{1}{2}\left(\begin{array}{c}S_X\\S_Y\end{array}\right)_{i+\frac{1}{2},j} + \frac{1}{2}\left(\begin{array}{c}\Delta F_{invisc}\\\Delta G_{invisc}\end{array}\right)_A \cdot \frac{1}{2}\left(\begin{array}{c}S_X\\S_Y\end{array}\right)_{i,j+\frac{1}{2}}\right\}
$$

Eq 2.4

$$\Delta F_A = \left(\frac{\partial F}{\partial Q}\right)_A \left(-\left(\frac{\Delta t}{V}\right)_A \sum_{f=1}^{4 \text{ faces of cell A}} \left(\overline{F}S_x + \overline{G}S_y\right)_f\right)$$

$$\Delta G_A = \left(\frac{\partial G}{\partial Q}\right)_A \left(-\left(\frac{\Delta t}{V}\right)_A \sum_{f=1}^{4 \text{ faces of cell A}} \left(\overline{F}S_x + \overline{G}S_y\right)_f\right)$$

Eq 2.5

The viscous fluxes are directly calculated on the secondary cell faces. The viscous contribution of the cell A to the change of the state vector stored at the cell vertex (i,j) can be calculated as

$$\delta Q_{(i,j)A,visc} = -\left(\frac{\Delta t}{V}\right)_{i,j} \left\{ \begin{pmatrix} F_{visc} \\ G_{visc} \end{pmatrix}_A \cdot \frac{1}{2}\begin{pmatrix} S_X \\ S_Y \end{pmatrix}_{i+\frac{1}{2},j} + \begin{pmatrix} F_{visc} \\ G_{visc} \end{pmatrix}_A \cdot \frac{1}{2}\begin{pmatrix} S_X \\ S_Y \end{pmatrix}_{i,j+\frac{1}{2}} \right\}$$

Eq 2.6

The overall change in the state vector is the sum of the inviscid and viscous fluxes. Additionally, fourth order artificial dissipation is added to prevent the high frequency oscillations and second order artificial dissipation is introduced in the vicinity of the shocks. To speed-up the convergence, a local time-stepping approach is used for steady simulations, and dual time-stepping method is utilized for the time resolved simulations. The non-reflecting boundary conditions of Giles [43] have also been implemented to prevent the spurious oscillations reflecting back into the domain from the boundaries. Further details of the discretization scheme and its implementation details can be found in Burdet. [44]

For the closure of the RANS equations the zero-equation Baldwin-Lomax [45], one-equation Spalart-Allmaras [46] and also two-equation Wilcox [29] k-ω turbulence models have been implemented. The implementation of the k-ω turbulence model is based on the high-resolution numerical schemes which will be explained more detailed in Section 2.2.1.

Major effort was put into the parallelization of the solver both on the CPUs and on the GPUs. The code was parallelized using the OpenMP approach and can run in parallel on modern multi-core CPU's with a reasonable

parallelization efficiency up to eight cores. More detailed explanation about the GPU parallelization and the specifications of the GPU version of the solver is given in 0.

2.2.1. High Resolution Implementation of the Wilcox k-ω Turbulence Model into "MULTI3"

RANS simulations are the state of the art approach for the turbine simulations. At least within the turbine they offer a good balance between the computational cost and the accuracy. In RANS simulations the type of the turbulence model used has a major influence on the quality of the results and it always has been a big discussion topic which turbulence model is superior to the others. Unfortunately, there is no straightforward answer to this question since each of these models have their own strengths and weaknesses which can make a particular turbulence model more attractive than the others for some scenarios and another one for the other scenarios. However, over the years with the increase in the computational power, the k-ω turbulence model has gained popularity in the turbomachinery community. Its superior character in modeling the wall vicinity flows emerged as a clear advantage which led the users to prefer this model over the widely used k-ε turbulence model.

In this chapter the implementation of the Wilcox [29] k-ω turbulence model into the LEC's URANS solver "MULTI3" will be covered. Special emphasis will be given to the implementation of the convective fluxes. For this implementation the state of the art high resolution schemes are considered because of their superior accuracy and stable character which is especially important for the implementation of the turbulence models because otherwise the robustness of the solver is severely affected.

2.2.2. Wilcox [29] k-ω Turbulence Model Equations

In the solver the k-ω turbulence model equations are solved in non-dimensional form. The procedure of the non-dimensionalization is given in detail in A1. The k-ω turbulence model equations are given below in the non-dimensional form. The turbulence model equations can be written in a

form where they are divided into parts depending on the physics they describe. According to this there are three parts of the equations which are the convective and the diffusive parts and the source terms composed of the production and the destruction terms.

$$\frac{\partial Q_T}{\partial t} = -\left[\frac{\partial F_C}{\partial x} + \frac{\partial G_C}{\partial y} + \frac{\partial H_C}{\partial z}\right] + \left[\frac{\partial F_D}{\partial x} + \frac{\partial G_D}{\partial y} + \frac{\partial H_D}{\partial z}\right] + P - D$$

Eq 2.7

Parallel to the conservative variable approach used in the momentum and energy equations, the turbulent state vector $\mathbf{Q_T}$ shown in Eq 2.8 is also used in its conservative form.

$$Q_T = \begin{bmatrix} \rho k \\ \rho \omega \end{bmatrix}$$

Eq 2.8

The convective fluxes in three directions are given in Eq 2.9.

$$F_C = \begin{bmatrix} \rho u k \\ \rho u \omega \end{bmatrix}, \quad G_C = \begin{bmatrix} \rho v k \\ \rho v \omega \end{bmatrix}, \quad H_C = \begin{bmatrix} \rho w k \\ \rho w \omega \end{bmatrix}$$

Eq 2.9

The diffusive fluxes in three directions are given in Eq 2.10.

$$F_D = \begin{bmatrix} \left(\dfrac{\mu}{\mathrm{Re}_{ref}} + \sigma^* \mu_t \right) \dfrac{\partial k}{\partial x} \\ \left(\dfrac{\mu}{\mathrm{Re}_{ref}} + \sigma \mu_t \right) \dfrac{\partial \omega}{\partial x} \end{bmatrix} , \quad G_D = \begin{bmatrix} \left(\dfrac{\mu}{\mathrm{Re}_{ref}} + \sigma^* \mu_t \right) \dfrac{\partial k}{\partial y} \\ \left(\dfrac{\mu}{\mathrm{Re}_{ref}} + \sigma \mu_t \right) \dfrac{\partial \omega}{\partial y} \end{bmatrix} , \quad H_D = \begin{bmatrix} \left(\dfrac{\mu}{\mathrm{Re}_{ref}} + \sigma^* \mu_t \right) \dfrac{\partial k}{\partial z} \\ \left(\dfrac{\mu}{\mathrm{Re}_{ref}} + \sigma \mu_t \right) \dfrac{\partial \omega}{\partial z} \end{bmatrix}$$

<div align="right">Eq 2.10</div>

In this implementation the production terms are modified according to Kato and Launder [47]. It prevents the overproduction of turbulence in stagnation points which was a major drawback of the original source terms in the model of Wilcox [29].

$$P = \begin{bmatrix} \mu_T S \Omega \\ \alpha S \Omega \end{bmatrix} , \quad D = \begin{bmatrix} \beta^* \rho \omega k \\ \beta^* \rho \omega^2 \end{bmatrix}$$

<div align="right">Eq 2.11</div>

the definition of S and Ω are given in Eq 2.12.

$$S = \sqrt{\frac{1}{2} \left(\frac{\partial u_i}{\partial x_j} + \frac{\partial u_j}{\partial x_i} \right)^2} , \quad \Omega = \sqrt{\frac{1}{2} \left(\frac{\partial u_i}{\partial x_j} - \frac{\partial u_j}{\partial x_i} \right)^2}$$

<div align="right">Eq 2.12</div>

The model coefficients for the low Reynolds version of the model are given by Chima [48]. Once the equations are solved for the turbulent state vector the eddy viscosity can be calculated and entered into the viscous flux calculations for the momentum and the energy equations. The eddy viscosity can be derived from the turbulent state vector using the Eq 2.13.

$$\mu_T = \alpha^* \frac{\rho k}{\omega}$$

<div align="right">Eq 2.13</div>

2.2.2.1.   Discretization of the equations

Parallel to the discretization of the RANS equations, the k-ω turbulence model equations are discretized using a cell-vertex storage scheme. According to this scheme, the turbulent state vector $\mathbf{Q_T}$ is stored at the vertices of the cells. For the discretization of the turbulence model equations the dual control volume approach [35] has been followed where the fluxes are evaluated on the faces of the so called pseudo cells. Pseudo cells are formed around the cell vertices by joining the cell centers of the real cells. In the two dimensional, structured mesh portion shown in Figure 2.4 the borders of the real cells are shown by the solid lines and the turbulent state vectors are stored at their vertices which are indicated with the i and j indices. The borders of the pseudo cell drawn around the red vertex are shown by the red dashed lines. Both the convective and the diffusive fluxes will be evaluated on the faces of the pseudo cells. In Figure 2.4 one of the faces of the red pseudo cell is marked with the letter S. Discretization schemes can be divided into two main groups depending on the way the fluxes on the cell faces are evaluated from the discrete data surrounding the face.

i) Discretization in space

Due to the major differences in the physics they describe different approaches have to be followed for the discretization of the convective and diffusive parts of the equations. The discretization strategy for each of these parts will be covered in separate sections.
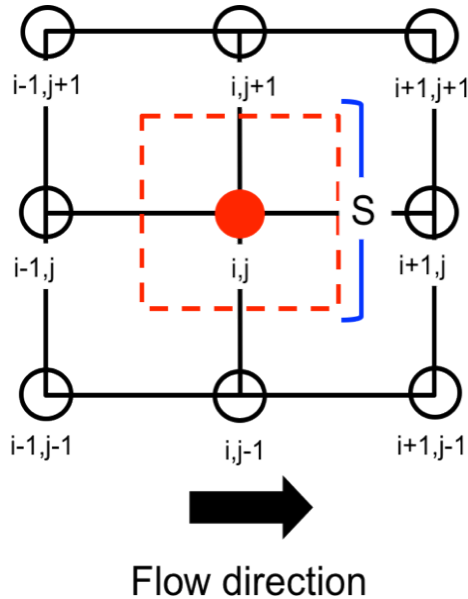
Figure 2.4 The constructed "pseudo" cell (shown in red) and its faces where the convective fluxes are evaluated on

Discretization of the Convective Fluxes

For the space discretization of the convective terms there are two major approaches.

- Central discretization
- Upwind discretization

Central schemes have second order accuracy in space, are easy to implement and computationally cheap. However, the downside of central schemes is their dispersive behavior. Unless the physical diffusion in the flow is at a certain value, high frequency artificial oscillations in the flow appear. The absence of any numerical diffusive terms in the central discretization of the convective terms necessitates cell Reynolds numbers being below two, which is a totally impractical criterion to obey for the

flow regimes within the turbomachinery. These oscillations not only reduce the quality of the results but also grow in time and lead to serious stability problems. Therefore, fourth order damping has to be added to the discretized equations which counteract the forming of the high frequency oscillations. On the other hand, adding more than necessary amount of damping leads to artificial numerical diffusion which reduces the quality of the results. So it is very crucial to have the artificial smoothing just at the right amount leading neither to highly diffusive results nor to oscillations. A high resolution smoothing algorithm combining second order and fourth order smoothing has been developed by Jameson, Schmidt and Turkel [], but its applicability is limited with the Navier-Stokes equations. The pressure sensor based switch which regulates the switching between the second order and the fourth order smoothing is not applicable to the turbulence model equations.

The same problem persists also if the Lax-Wendroff method is utilized for the space and time discretization of the convective terms. Even though the Lax-Wendroff method includes numerical diffusion which helps the scheme to stabilize, it is usually not enough and artificial oscillations appear unless damped by a fourth order smoothing operator. Previous efforts of using Lax-Wendroff method for the discretization of the convective part showed serious stability problems except at very low Mach number flows. Moreover, in the work of Liu and Zheng [49] it has been stated that using central scheme for the discretization of the convective part of the k-ε turbulence model equations was not satisfactory according to one of the reviewer's experience which was explicitly stated in the manuscript.

The alternative to the central discretization scheme is the upwind schemes where a biased strategy according to the convection direction is followed in the computation of the fluxes at the cell faces. The most basic version of the upwind schemes is the so-called simple upwind scheme. It has a clear advantage over the central schemes that it does not lead to artificial oscillations due to its inherent artificial diffusive terms. However, it has a first order of accuracy and also has a very diffusive character which makes this scheme totally impractical for the general purpose CFD codes.

To increase its accuracy and reduce the diffusive character the order of the simple upwind scheme has to be increased. Second order upwind schemes

are much less diffusive and therefore are widely used in the state of the art CFD codes. However, keeping the second order accuracy might induce artificial oscillations if the local gradients across the cells are beyond a certain threshold. In order to keep a scheme non-oscillatory the second order terms which reduce the numerical dissipation have to be limited depending on the local gradients. When necessary the scheme has to be locally downgraded to the first order simple upwind scheme as Godunov [50] has pointed out that the non-oscillatory schemes can only have at most a first order accuracy in space. This approach is the main idea behind the high resolution schemes utilized in modern CFD codes. So, the first order upwind scheme forms a good basis for the implementation because of its oscillation free character. And on top of this scheme second order terms will be added which will be limited in a way to prevent any artificial oscillations.

First order flux calculation

The convective fluxes are evaluated on the faces of the pseudo cells formed around the vertices where the turbulent state vectors are stored. In the three-dimensional sketch shown in Figure 2.5 the four real cells are shown in four different transparent colors and are bordered by the solid black lines. The vertices of one of these four real cells are enumerated. The volumes shown in solid colors depict half of the pseudo cell drawn around the node 1. The other half of the pseudo cell is not shown. The portions of the pseudo cell are shown in the same color of the real cells that they belong. The cell with the enumerated vertices is isolated and shown in Figure 2.6. Moreover, the faces of the pseudo cell portion pointing in i,j,k directions are also indicated. The fluxes are evaluated on these faces and the resulting residual is added to the respective vertices. In total, there are 24 faces for all the eight pseudo cell portions inside a real cell. However, each of these faces is shared by two pseudo cells. Once the flux on one of these faces is calculated it is added to the residual belonging to the vertex on one side of the face and subtracted from the residual of the vertex on the other side of the face. In this manner the conversation of the fluxes is ensured. According to the upwind discretization scheme for the evaluation of the convective fluxes first the upwind direction has to be determined at the pseudo cell face where the fluxes are evaluated. For the determination of

the upwind direction the local velocity vector at the pseudo cell face is required which is evaluated by simple averaging of the two velocity vectors stored at the nodes each side of the edge. The averaging procedure for the u velocity is shown in   Eq   2.14   for   the   three   faces indicated in Figure 2.6.
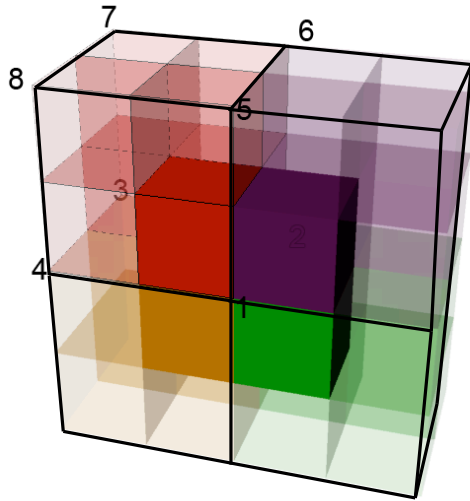
Figure 2.5 Real cells shown in transparent colors and bordered with the solid black lines and portions of the pseudo cell around the node 1 shown in solid colors

$$u_{S_{1,i}} = 0.5(u_1 + u_4)$$
$$u_{S_{1,j}} = 0.5(u_1 + u_2) \qquad \text{Eq 2.14}$$
$$u_{S_{1,k}} = 0.5(u_1 + u_5)$$
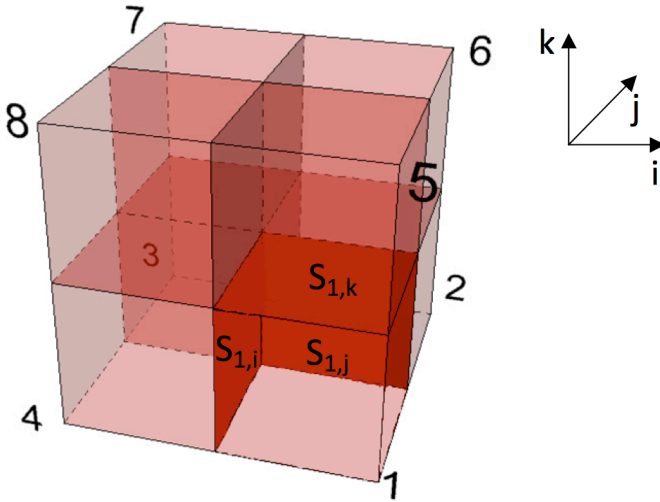
Figure 2.6 The real cell bordered with the solid black lines and the faces of the pseudo cell portion around node 1 are shown in solid red.

According to the sign of the dot product of the surface normal vector with the averaged velocity vector the upwind direction can be identified. After identifying the upwind direction, the turbulent state vector positioned at the upstream vertex is used in the flux computations.

Second order flux calculation

The implementation of the second order fluxes will be explained on the basis of the two dimensional, structured Cartesian mesh depicted in Figure 2.4. To evaluate the convective flux at the pseudo cell face indicated by S in Figure 2.4 first the upwind direction has to be identified. The first order flux is derived only from the state vector stored at the upstream node. The second order flux calculations make use of a larger stencil in the upstream direction. Assuming a flow field from left to right the face value of the unknowns can be approximated with second order accuracy using Eq 2.15. The first order term is only based on the value of the upstream node and the

second order contribution is expressed as a product of the ratio R and the difference of the values of the unknowns at the neighboring vertices.

$$\phi_S = \underbrace{\phi_{i,j}}_{\substack{\text{1st order contribution} \\ \text{(upwind)}}} + \underbrace{\frac{1}{2} R_S \left(\phi_{i+1,j} - \phi_{i,j} \right)}_{\text{2nd order contribution}}$$

Eq 2.15

where

$$R_S = \frac{\phi_{i,j} - \phi_{i-1,j}}{\phi_{i+1,j} - \phi_{i,j}}$$

For the calculation of the ratio R_S the values of the unknowns at the far upstream node ($\Phi_{i-1,j}$) of the cell face is required. By far upstream node the upstream neighbor of the node that is located upstream of the cell face is meant. Locating of this additional node is a straightforward issue in structured meshes. However, in both unstructured and in multi-block but structured meshes this task can be locally ambiguous. For example; as shown in Figure 2.7 at the junction of the blocks where singular nodes usually appear, there is no straight answer for locating this far upstream node. Because of these reason an alternative strategy is followed.

For the unstructured grids the definition of the ratio R_S has been modified by Darwish and Moukalled [51]. The revised definition for R_S is given below in Eq 2.16. Instead of the index based notation used for the structured grids an alternative labeling is used in the adapted formulation. In this formulation the indices C and D represent the upwind and the downwind nodes with respect to the cell face where the flux will be evaluated on. The advantage of this formulation is that it does not include any term directly for the far upstream node but requires the gradient of the unknowns at the upstream node C instead. These spatial gradients have to be calculated in three directions using the Green-Gauss theorem. As a disadvantage, there is a considerable computational cost that is associated with the calculation of this gradient term.
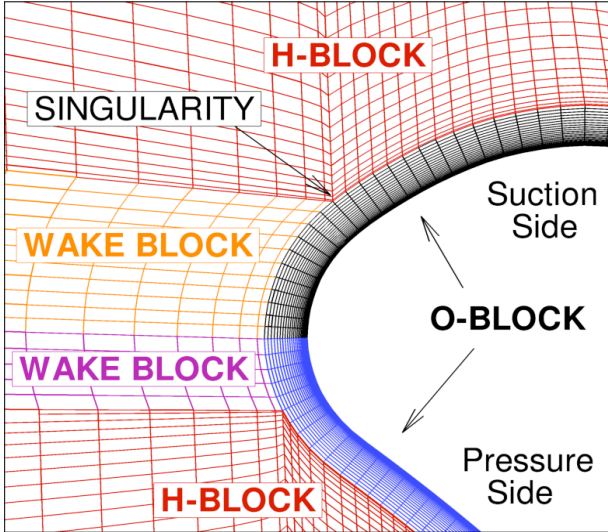
Figure 2.7 The singular nodes at the junction points of the blocks within the mesh where it is not straightforward to position the far upstream node required for the second order flux calculations

$$R_S = \frac{\left(2\nabla\phi_C \cdot r_{CD}\right)}{\phi_D - \phi_C} - 1$$

Eq 2.16

Next the implementation of the convective fluxes will be tested on a scenario where only the convective part of the turbulence model equations is considered. As a test case, a uniform turbulent kinetic energy is imposed at the inlet boundary of a single stator domain and the flow field is updated in time until the imposed turbulent kinetic energy level reaches the stator trailing edge. Additionally, a zero turbulent kinetic energy condition is set at the walls. Before running this numerical experiment, the single stator simulation is iterated using a simpler zero equation turbulence model until convergence since this velocity field is directly used in the calculation of the convective fluxes. Convecting the turbulent kinetic energy as a passive scalar using the first order and the second order upwind schemes separately

and making a constant axial cut in the domain for both of the cases, the accuracy of these schemes can be compared in terms of their lateral turbulent kinetic energy predictions. Figure 2.8 shows the convection of the turbulent kinetic energy within the passage simulated using the second order upwind scheme. In the vicinity of the blade walls boundary layers are present where the convective velocities sharply drop. Therefore the rise in the turbulent kinetic energy level within the boundary layers lacks behind the rise everywhere else within the passage. Even though diffusive fluxes are not evaluated in this test case there are weak gradients of the turbulent kinetic energy in streamwise direction which reflects the slight diffusive character of the second order discretization. The streamwise diffusion of the turbulent kinetic energy would be much more pronounced if the simple first order upwind scheme were applied.
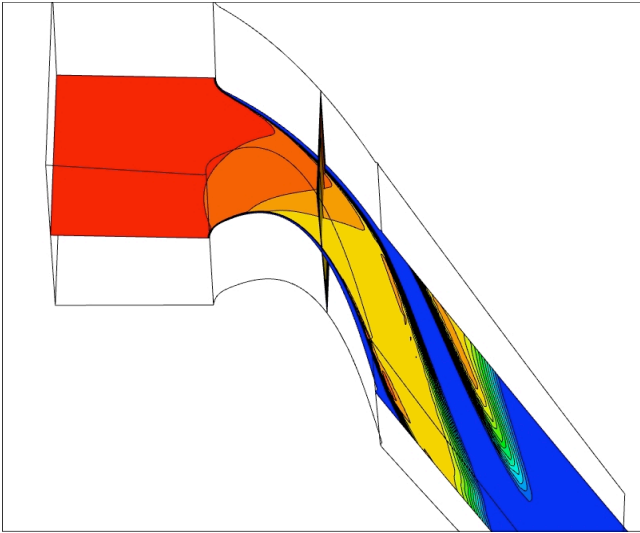
Figure 2.8 Convection of the turbulent kinetic energy through the stator passage simulated using second order upwind discretization

Figure 2.9 shows the distribution of the calculated lateral turbulent kinetic energy distribution at the constant axial cut at about 70% axial chord. This distribution was calculated by the first order simple upwind scheme. At this

axial chord the secondary flow vortices are already developed which generate blockage close to the endwalls at the suction side. The variation in the convective flow velocity generated spatial gradients in the level of the turbulent kinetic energy at this particular cut and time. For example at the boundary layers or close to the secondary flow features there are regions with a deficit in the turbulent kinetic energy level, which could have been balanced by the numerical diffusion inherent in the discretization scheme.

Figure 2.9 The calculated turbulent kinetic energy distribution at 70% axial chord (modeling pure convection via first order upwind scheme)

To evaluate the effect of the numerical diffusion in the distribution of the turbulent kinetic energy the calculated turbulent kinetic energy distributions resulting from two simulations are compared. In one of these simulations the first order simple upwind scheme is utilized and in the other one the second order upwind scheme is used in the discretization of the convective fluxes. Figure 2.10 shows the calculated lateral turbulent kinetic energy distributions at about 70% axial chord for both of the simulations. As expected, the simple upwind discretization leads to a diffused distribution at the secondary flow structures where the second order counterpart leads to much sharper distributions. However, there are also some overshoots of the turbulent kinetic energy which is completely numerical since rise of the

turbulent kinetic energy could only have been possible with a source term in the equations which was neglected for this test. These overshoots in the level of the turbulent kinetic energy are due to the oscillatory behavior of the higher order schemes. As shown here, they decrease the quality of the results moreover they decrease the robustness of the implementation which is especially important in the case of the turbulence model implementations.

Figure 2.10 The calculated turbulent kinetic energy distribution at 70% axial chord (modeling pure convection via first order upwind scheme and the second order upwind scheme)

Limiters

As shown the second order upwind schemes led to local artificial oscillations which affect both the quality of the results and the robustness of the implementation. These oscillations can be prevented by locally limiting the fluxes at the regions where the local gradients go beyond a certain threshold. Thereby the non-oscillatory character of the scheme is ensured. Eq 2.17 presents the limited version of the equation used to approximate

the face value of the unknowns. The limiter functions are functions of R_S which cut off the second order flux contribution depending on the value of the ratio R_S which is a measure of the local spatial gradient.

$$\phi_S = \underbrace{\phi_{i,j}}_{\substack{\text{1st order contribution} \\ \text{(upwind)}}} + \underbrace{\frac{1}{2}\Psi(R_S)(\phi_{i+1,j} - \phi_{i,j})}_{\text{2nd order contribution}}$$
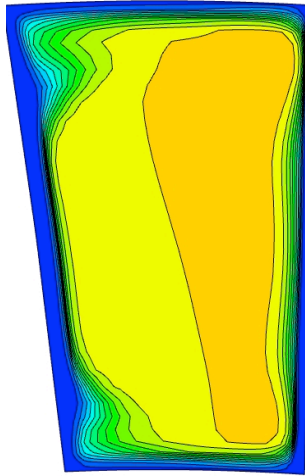
Eq 2.17

Figure 2.11 The calculated turbulent kinetic energy distribution at 70% axial chord (modeling pure convection via unlimited second order upwind scheme and the min-mod limited second order upwind scheme)

Each limiter has a different limiting behavior; some of them directly cut of the flux if the local gradient goes beyond a certain threshold. On the other hand, there are some which limit the fluxes in a continuous manner like Van Leer [52] and Van Albeda [53] limiters. In this work, the "Minmod" and Superbee [54] limiters will be considered. These two limiters represent the two extremes where the "Minmod" limiter has the most diffusive character and the Superbee limiter on the other hand shows the lowest

diffusive character among all the limiters. Integrating these two limiters to the flux calculations, their effect on the flow field can be tested using the same test case. Figure 2.11 shows the calculated lateral turbulent kinetic energy distribution calculated with the second order upwind scheme without applying any limiters and using the min-mod limiter. As shown, the artificial oscillations present near the secondary flow features are removed with the effect of the limiters. In the regions where the overshoots appeared the limiters cut off the second order terms and eliminate the oscillations thereby. In Figure 2.12 the distribution pattern obtained using the Superbee limited second order upwind scheme is compared with the min-mod limited version. Compared to the results obtained with the min-mod limiter Superbee limiter showed a less diffusive character and again without any artificial oscillations. This behavior of the Superbee limiter is due to its character keeping the second order term without limiting up to a higher gradient threshold. So within the limiters providing a non-oscillatory scheme, the min-mod limiter leads to most diffusive results and the Superbee limiter to the least diffusive ones. However, it is also known that the Superbee limiter has a character of over-sharpening of the structures. So in case of smooth structures using the Superbee limiter might not be the most appropriate. This is why in this implementation the Sweby [55] limiter is considered which includes an additional parameter β and thereby can represent infinitely many limiting functions between these two extreme limiting functions. The limiter function is given in Eq 2.18. Setting the $\beta = 0$, it behaves as the "Minmod" limiter and on the other hand, setting $\beta = 2$ the Superbee limiter is recovered. For this implementation the β parameter is set to 1.5. With that the limiter function represents a behavior in-between the two extremes.

$$\Psi\left(R_s\right) = \max\left[0, \min\left(\beta R_s, 1\right), \min\left(R_s, \beta\right)\right], \; \left(1 \le \beta \le 2\right)$$

Eq 2.18
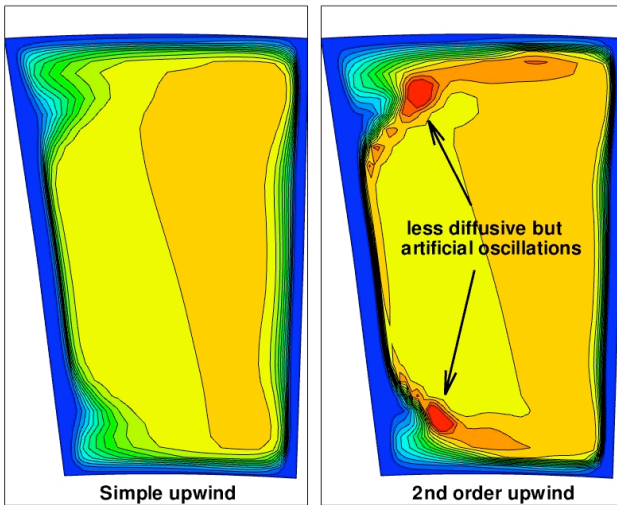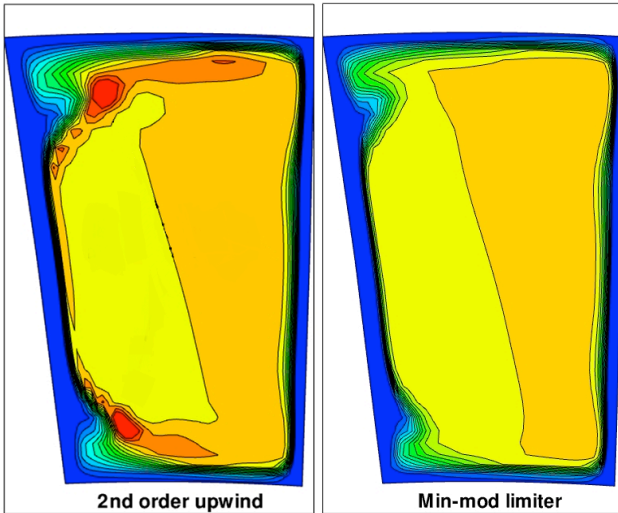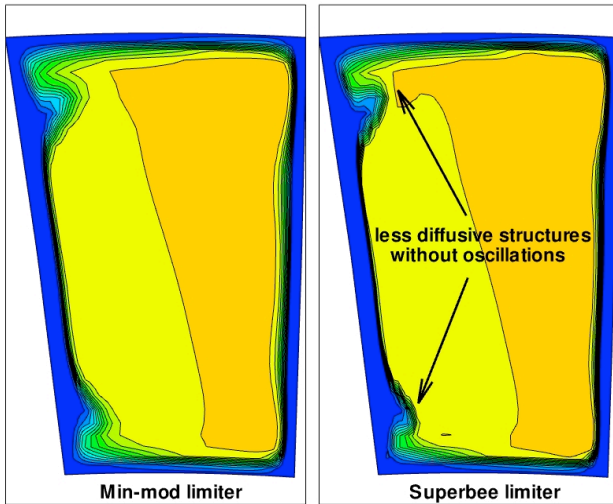
Figure 2.12 The calculated turbulent kinetic energy distribution at 70% axial chord (modeling pure convection via the min-mod limited second order upwind scheme and the Superbee [48] limited second order upwind scheme)

Discretization of the Diffusive Fluxes

The diffusive fluxes of the *k-ω* turbulence model equations are calculated using a central discretization scheme which has a second order accuracy in space and no oscillations are generated due to the diffusion included in the physics itself. The diffusive fluxes are evaluated at the faces of the pseudo cells in a similar way mentioned before. For the computation of the diffusive fluxes the gradients of k and ω are needed which are calculated using the Green-Gauss theorem. They are stored at the cell centers and can be directly used to calculate the diffusive fluxes at the faces of the pseudo cells.

ii) Discretization in Time

Parallel to the time integration of the Navier-Stokes equations an explicit time integration strategy is followed for the k-ω turbulence model equations. However, the negative source terms had to be treated implicitly because of their stiff character. For steady simulations, the time integrations of the convective, diffusive and positive source terms are carried out using the first order explicit Euler method, which is first order accurate in time. For convection dominated problems the explicit Euler time integration is only stable if the convective terms are discretized in space using the first order upwind scheme. As it is the unlimited spatially second order upwind discretization is unstable with this time integration scheme. However, utilizing the limiters that prevent the oscillations the stability of the first order explicit Euler time integration is ensured as long as the CFL number is below 1. [56] For steady simulations the same local time stepping method used for the Navier-Stokes equations is utilized. The low order temporal accuracy of the explicit Euler method is not important when steady state solutions are of interest. The strategy for the time resolved simulations will be covered later on.

As mentioned before due to their stiff character the negative source terms had to be dealt implicitly, because otherwise the allowable time step limit for the k-ω equations is extremely reduced. Generally implicit methods are known for increased computational cost per time step and are also harder to implement than the explicit methods. However, for the implicit integration of the source terms these arguments are not valid. The absence of any spatial gradients in the source terms enables that each equation can be solved independently. So no linear system of equations has to be solved which require high computational effort and memory. In this implementation a basic non-linear Jacobi method has been used. Using this method two second order, algebraic equations are formed for the two components of the turbulent state vector. These equations can be solved algebraically. These two equations are coupled in one way, such that the equation for the turbulent kinetic energy requires the value of ω but not the other way around. So first the second equation is solved for the second component $\rho\omega$ of the turbulent state vector which is then substituted into

the other equation to solve for the first component of the turbulent state vector ρk.

Time-accurate calculations

For the time-resolved simulations dual time stepping method of Jameson [57] is applied. In this method an additional time derivative is added which is discretized using the second order backward Euler time integration scheme. In this method the physical time is separated from the pseudo time where the state variables are iterated until convergence before moving on to the next physical time step.

2.2.2.2.   Boundary Conditions

In turbomachinery applications there are usually four types of domain boundaries. These are the inlet, outlet, periodic faces and the walls. Along these boundaries the turbulent state vector is treated in the following ways. At the domain inlet the turbulent state vector is calculated for a given turbulent intensity and turbulent length scale distribution and imposed in the form of Dirichlet type boundary conditions. At the domain outlet both variables are extrapolated. The residuals of the nodes at one side of the periodic face are accumulated with the residuals of the corresponding nodes from the other periodic face. Moreover, the turbulent state vector is additionally equalized at the corresponding nodes of the periodic faces of the domain. The wall boundary condition is probably the most crucial one among all the others. At the wall the turbulent kinetic energy is set to zero. There are some variations in the way the turbulent dissipation rate $\rho\omega$ is imposed. Following the approach of Wilcox [29] the value of $\rho\omega$ is set only at the wall nodes according to Eq 2.19. In this equation y stands for the perpendicular distance of the first node from the wall. For finer meshes having at least five points within the laminar sub-layer the values of the nodes inside the laminar sublayer can also be imposed which might be the case for the heat transfer simulations.

$$\rho\omega = \frac{6\rho\mu}{\beta y^2}$$

2.2.2.3.   Validation & Discussion

The implementation has been validated on the well-known scenarios such as the developing turbulent boundary layer on flat plate which the turbulence models are best tuned for. The details of this validation study are given in Section 4.6. Moreover, the implemented turbulence model has also been tested on more elaborate flow scenarios such as multi-row, axial turbine simulations. The details of the simulation is explained in Section 4.6.

a)   b)
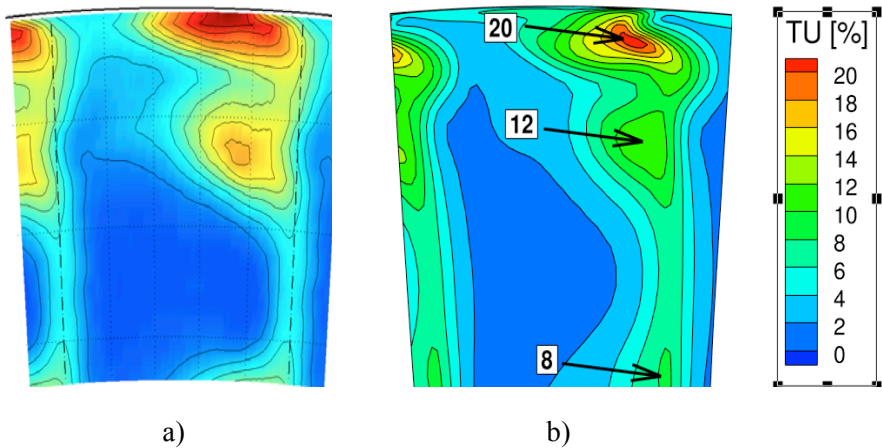
Figure 2.13 The time averaged relative turbulence intensity downstream of the rotor blade – only single rotor blade passage is shown a) Measurement [58] b) CFD prediction using Wilcox k-ω turbulence model

In Figure 2.13 the time averaged relative turbulence intensity predictions downstream of the rotor blade is compared with the experimental measurements. The position of the measurement plane relative to the rotor

is shown in Figure 2.14. Even though there is a qualitative agreement between the experimental and numerical results, quantitatively there is an underestimation of the turbulence intensity levels in CFD relative to the measurements. As it will be discussed more in detail in Section 4.6 the underestimation of the turbulence intensity leads to the underestimation of the turbulence mixing in the near-wake region. A part of this mismatch between the CFD and the measurement can be still due to the numerical dissipation errors related to the mesh density and the order of the numerical scheme. A considerable portion of the numerical dissipation has already been eliminated using a new anisotropic artificial dissipation algorithm. A certain part of these errors are also due to the incapability of the turbulence model to handle the highly three-dimensional flow field inside the secondary flow regions. Similar misbehaviors of the two-equation turbulence models have been reported by Chima [48] and Kulisa and Dano [59] in the near wake region of the compressor and turbine blades respectively.
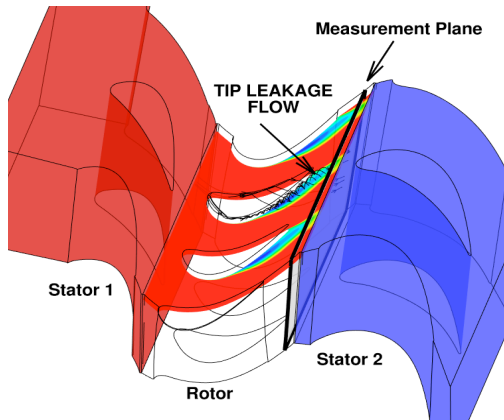
Figure 2.14 The 20° degree section of the one-and-a-half stage turbine configuration showing the location of the measurement plane downstream of the rotor and the tip leakage flow extending to the measurement plane

2.2.3. GPU Acceleration of "MULTI3"

The steep rise in the computational power of the GPU's in the recent years and also the emergence of the high-level programming models enabling to program them easily made a breakthrough in the scientific computing area. The in-house CFD solver "MULTI3" is thoroughly adapted in order to benefit from the computational power of the modern GPU's.

The CUDA programming model that was developed by Nvidia is based on an extended C programming language and enables to deploy the compute intensive loops which are called kernels onto the GPU. The loops that need to be executed on the GPU have to be re-written in CUDA language which requires a considerable effort. After the GPU programming gained some popularization more high level, directive based GPU programming models have emerged. The "PGI Accelerator" [60] programming model is one of these. In this model the kernels are automatically generated by the compiler itself based on the compiler directives added by the user. So, the developers are freed from converting the loops into the kernels and the code development time can be considerably decreased thereby. Moreover, to some level it also deals with the management of the different hierarchical GPU memory levels as well, which otherwise have to be done by the programmer. However, still major re-structuring of the code has to be carried out by the programmers to benefit from the huge performance potentials of the GPUs. One of the most important issues that has to be dealt by the programmers is to minimize the data transfer between the CPU and the graphic card which would kill all the speedup gained if not properly treated. Secondly, the modifications in the organization of the data in the memory that would ensure a coalesced memory access also have a profound impact on the speedup level.

At the time of this study the "PGI Accelerator" [60] programming model has been quite recently developed and was not mature yet, which raised some hesitance about using this programming model. However, the re-structuring of the code had to be dealt anyway using this programming model or any other. In case a good performance was not obtained using this programming model, alternatives could also have been considered which would require the re-structuring of the code as well. Because of the reasons

mentioned above the "PGI Accelerator" programming model has been initially selected for the GPU parallelization of "MULTI3".

In this chapter the fundamentals of the GPU parallelization will be covered. The GPU parallelization project has been undertaken in subsequent steps.

Step 1) Parallelization of the laminar section of the solver (Huber [61])

Step 2) Parallelization of the k - ω turbulence model

Step 3) Parallelization of the other functionalities supporting unsteady, multi row simulations

Step 4) Memory Management

Step 5) Multi GPU support (ongoing development)

First, the laminar portion of the code has been deployed to a single GPU and tested for performance on a laminar, single row, single passage stator simulation. The test showed an impressive 13.6x speedup on a "Fermi" class GPU compared to a single core of the multi core AMD Opteron 2435 CPU using double precision accuracy. The specifications of the hardware are given in Table 2.1. The details of the implementation, code re-structuring and validation of the implementation for the initial step of the parallelization project are found in [61]. Based on the very positive speedup rates achieved, the parallelization is continued using the same programming model to deploy all the other functionalities of the code to the GPU.

Table 2.1 Specifications of the computer hardware used [62]

	AMD Opteron 2435 "Istanbul"	Intel i7-2600 "Sandy Bridge"	Nvidia Tesla C2070 "Fermi"	Nvidia Tesla K20X "Kepler"
SP Performance (Gflops)	124	216	1030	3950
DP Performance (Gflops)	62 / 10 per core	108 / 27 per core	515	1310
Number of cores	6	4	448	2688
Onboard Memory (GB)	16 – 128	16 – 128	6	6
Memory bandwith (GB/s)	24	21	144	250
Approx. Price ($)	-	350	1400	3000

2.2.3.1.   Acceleration of the k-ω turbulence model

The parallelization of the k - ω turbulence model is next considered. As explained in Section 2.2.1, the implementation of the convective part of the k - ω turbulence model equations is based on the high resolution upwind scheme which has a second order accuracy in space and ensures a non-oscillatory character as well. As it has been implemented in the CPU version of the code, the implementation of the convective fluxes causes a major problem for the GPU parallelization. In the implementation of this part of the code conditional statements have been used to decide for the upwind direction depending on the sign of the dot product between the velocity vector and the cell face normal. If the dot product is positive the fluxes are evaluated from the node at one side of the cell face and on the other hand, if it is negative the fluxes are evaluated from the node at the other side of the cell face. However, placing conditional statements within

loops is restrained in the GPU computing if for some indices of the loop one branch of the conditional statement is selected and for the other indices the other one. This requires the parallel running threads within a warp to choose the different branches of the conditional statement which cannot be executed in parallel. Not considering this issue can cause the speedup rate to drop dramatically. So, for the GPU parallelization the algorithm has to be adapted accordingly. In that regard, an alternative method has been developed using the "min" and "max" operators to decide the upwind direction.

2.2.3.2.   Memory Management

Although the GPUs offer very high level of computing power (up to 1 Teraflops) they are connected to a relatively small onboard memory. Parallel to the very widely used comparison GPUs could be resembled to large passenger aircrafts that can take so many passengers but only with one hand baggage for each. None of the passengers are allowed to check in his/her baggage.

In the code re-structuring this important hardware restriction should also been taken into account. The huge computational power of the GPU is only worth to consider if the size of the simulations is also big enough. With meshes that are smaller than a certain size the whole performance of the GPU cannot be utilized. Moreover, running the simulations that would normally take one hour in five minutes is not as considerable as running the simulations that would normally take two weeks in one day even though both of them show the same speedup rates. So, the performance of the GPUs would be more valuable if large size simulations could be carried out with them. This is why sometimes the speedup rate should be sacrificed in order to reduce the memory usage. In that regard all the arrays both the global ones declared in the module and also the local ones declared only within the subroutines are allocated dynamically. However, in "PGI's Accelerator" programming model [60] it turned out that the allocation and de-allocation of the arrays declared in the module with the "mirror" statement creates a very high computational overhead. This is why only the necessary global arrays are declared within the module of the code. All the other temporary arrays are declared locally within the subroutines using the "device" keyword meaning that they are only allocated on the GPU's

global memory and they are de-allocated from the memory once they are not needed any more. The allocation and deallocation of these "device" arrays did not create a considerable overhead. So, the code has been re-structured to reduce the number of the global arrays as much as possible and declare them as temporary arrays within the subroutines.

The second important code restructuring aimed to reduce the memory usage in multi-row simulations. Usually single row simulations easily fit into the memory of the current graphic cards, but the memory limit of the card is easily reached as the row numbers increase. For this reason the code is re-structured in a way that the calculations of the rows are carried out in a subsequent manner; meaning that the state vector of the nodes within the first row is first updated, and then the state vector of the nodes within the second row is next updated and the procedure continues in the same way until the last row. This approach brought the advantage that the temporary arrays could be allocated by the size of the mesh with the maximum number of the nodes among the blade row meshes. With this approach the memory requirement of the code is considerably reduced for the multi-row simulations. Figure 2.15 shows the memory requirements in megabytes per 1k grid nodes for two different simulations using single precision accuracy . The single row calculation requires 1 megabyte of memory per 1k nodes on the other hand; the memory requirement reduces to 0.81 megabytes for the same number of grid nodes for the stage simulation. Using this approach, there was approximately 20% reduction in the GPU memory usage of the solver. With the current state of the solver using the anisotropic artificial dissipation approach, which will be covered in 1, 20° section of a one-and-a half stage axial turbine mesh of 4.5 million grid points requires 3.9 GBytes of graphic card memory using single precision accuracy. A multi-row mesh up to 6 million grid points can fit into the onboard memory of the "Nvidia C2070" graphic card that offers the largest onboard memory size on the market. (6 GBytes of RAM; however, 10% of the memory is dedicated for the memory correction.)
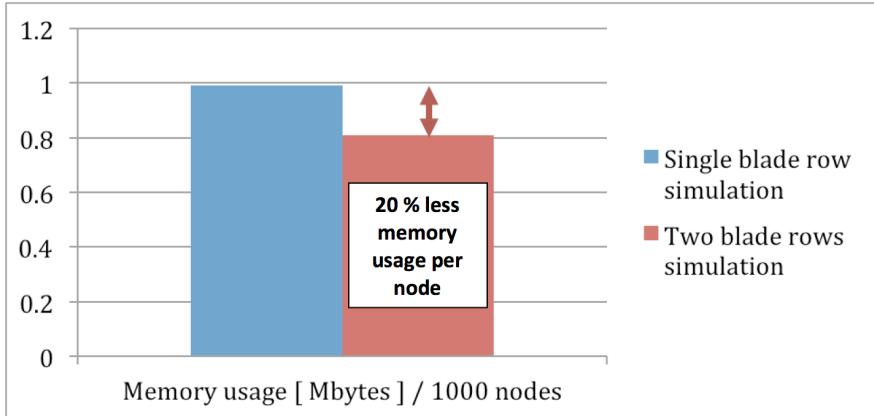
Figure 2.15 The memory usages in MBytes per 1k grid nodes for the single row and the two blade rows simulations using single precision accuracy

Problems larger than this size need to be divided into separate graphic cards. However, meshes that are smaller than a certain size would lead to the under-utilization of the GPU's computational capacity. In the current implementation the inlet and outlet boundary conditions are treated on the CPU which needs the data at the inlet and outlet planes of the domain to be transferred to the CPU. The coarser the mesh is the higher will be the proportion of the nodes at the domain boundaries to the overall mesh size. In conclusion, the relative communication overhead between the CPU and the GPU increases as the mesh size is reduced. Figure 2.16 shows the variation in the GPU utilization for different mesh sizes. Meshes that are smaller than one million nodes cannot effectively utilize the high computational power of the GPU's. This graph should be considered for the multi-GPU parallelization of the solver to determine the optimum number of the GPU's to allocate for a specific problem size.
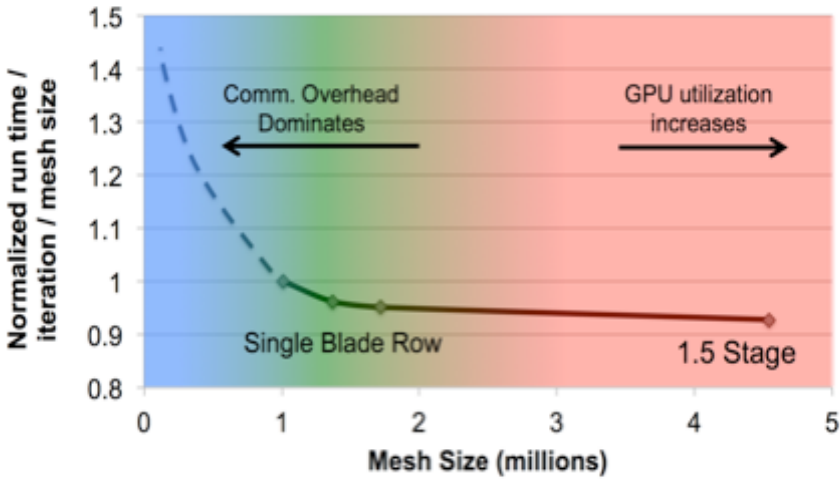
Figure 2.16 Utilization of the computation capacity of the GPU vs. the mesh size

2.2.3.3.   **Performance & Discussion**

The performance of the GPU acceleration of the whole solver including the k-ω turbulence model is tested on a single stator row mesh with 1.7 million mesh points and using the isotropic artificial dissipation scheme. The speed-up rates given in Figure 2.17 are relative to the run time on a single core of the "AMD Opteron 2435" CPU. The speed-up rates achieved with the OpenMP parallelized version of the solver on the multi-core AMD and on the more recent "Intel i7-2600" CPU's are also shown. Using double precision accuracy a 16X reduction in run time is achieved with the "Nvidia C2070" GPU based on the "Fermi" architecture. The more recent "Intel" CPU shows about 2X speed-up compared to the "AMD Opteron 2435" processor. And the recent "Nvidia" GPU based on the "Kepler" architecture shows a 2X speedup on the current scenario over the older "Nvidia" GPU based on the "Fermi" architecture. The specifications of the hardware are given in Table 2.1.
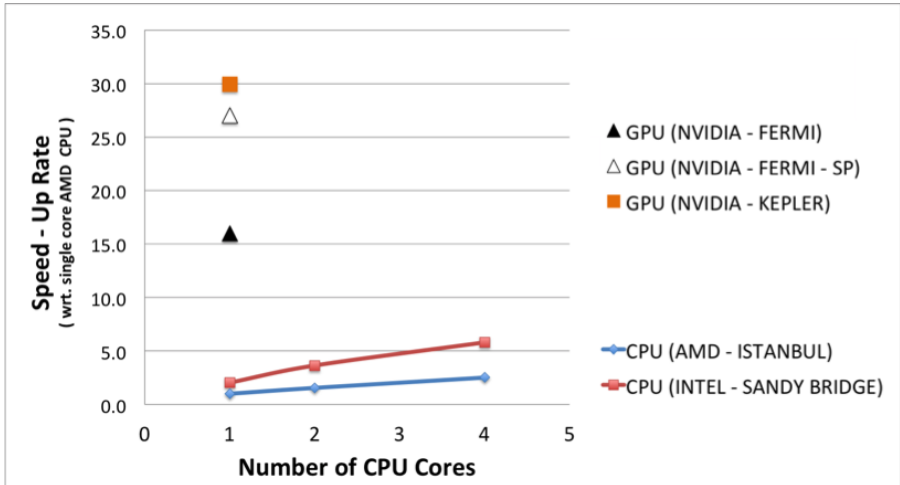
Figure 2.17 Comparison of the measured speed-up rates for the GPU accelerated and OpenMP parallelized versions of the solver (SP : single precision)

Looking at the speedup rates with respect to the single core CPU's one can realize that the rates deviate significantly from the theoretical speed-up rates one could expect comparing the flop rates of the hardware. This is due to the fact that the current numerical algorithm has a moderate computational intensity and the memory bandwidth of the hardware is the limiting factor rather than the flop rate of the GPU. So, due to the fact that the problem is rather memory bandwidth bound the whole computational capacity of the GPU cannot be utilized. On the other hand, CPU's are more tolerant in utilizing the memory bandwidth due to the large cache sizes and it does not require substantial programming effort to utilize those fast memories. However, this is not the case for the current GPU architectures.

One solution to this problem is to explicitly utilize the faster memory levels of the GPU such as the shared memory which are directly placed on the chip and increase thereby the overall memory bandwidth. The more explicit "Cuda Fortran" programming approach allows a direct utilization of these faster memory levels. The performance tests conducted on the subroutine involved in the derivative calculation showed that the "Cuda-Fortran"

approach results in a further 2X speed-up over the implicit "PGI Accelerator" approach. However, this was not the case in all of the subroutines. So, re-programming only of the subroutines which have large intensity of memory operations using "CUDA Fortran" can further increase the performance of the solver but also keep the programming effort relatively low.

2.3.   Unsteady Particle Tracking Tool "UNS-TRACK"

As a complementary tool to the existing in-house CFD capabilities an unsteady particle tracking tool "UNS-TRACK" has been developed with the intent to analyze the unsteady simulation data in a more detailed fashion and thereby to get more insight from the inherently unsteady flow patterns inside the turbine. First, it was developed for simulating the convection of the particles without mass and later on the code was adapted to deal with the particles with mass as well for further numerical studies to model the erosion in turbomachinery imposed to particulate flows.

The particle tracking tool is not integrated into the solver but rather coupled to it as a post-processing tool that runs on the unsteady flow data generated by the solver. Major effort was given in dealing with the particles at the domain boundaries such as the periodics, the row interfaces and the blade walls. It is important to detect that they are at the boundaries and apply the necessary treatments according to the boundary type. Otherwise, quite frequently particles may not stay within the flow passage but move out of the computational domain.

2.3.1. Time Integration

During the unsteady RANS simulations the flow field data is continuously written out in equal time intervals set as an input parameter in the beginning of the simulation. The length of these time intervals depends on the unsteady phenomenon that is investigated and dictated by the flow physics not by the stability constraints of the numerical scheme. In Jameson's [57] dual time stepping approach that the solver makes use of for the unsteady simulations there is an additional time step which is bound to

the CFL stability limit of the explicit numerical scheme. Different from the physical time step this local pseudo time step varies from one position to the other within the mesh.

Similar to the approach used on the solver side the particle tracking tool also makes use of two different time steps. The first time step Δt is dictated by the time interval the unsteady flow data has been written out. In the Eulerian definition the velocity vector at one point in the domain is a function of both space and time. For the numerical integration in physical time the third order Adams Bashforth method has been utilized which is a linear multi step method. The time averaged velocity vector at one point can be easily derived by the local velocity vectors at three subsequent physical time steps. Using Eq 2.20 the time averaged velocity at a particular position can be calculated provided that the flow field data is written in equal time intervals.

$$\bar{u}(x_{part}) = \frac{23u_{t+2}(x_{part}) - 16u_{t+1}(x_{part}) + 5u_{t}(x_{part})}{12}$$

Eq 2.20

There is a second time step $\Delta\tau$ which is similar to the one used in the inner iterations of the dual time stepping approach. This time step criteria should ensure that the particle does not travel a distance more than one cell dimension. If it is violated, particles can deviate from the real flow path considerably and even unphysical situations like migration of the particles into the solid walls might occur. There is a very big variation in the level of this time step within the mesh. Within the boundary layer this time step criterion is very strict because of the small mesh size on the other hand, in the middle of the passage it might be by a few orders of magnitudes larger. The very low time step levels close to the walls increase the cost of the computation. In order to reduce the computational cost this criterion is set to a pre-defined value for all the regions within the mesh. The effect of this approach on the accuracy of the calculation of the particle paths will be analyzed later on. Usually within the scope of this work the numerical time step criteria is set to one fourth of the physical time step.

$$\Delta\tau = 0.25\Delta t$$

<div align="right">Eq 2.21</div>

2.3.2. Interpolation Scheme

The velocity vector data is available at discrete points and to evaluate the velocity vector at one particular point an interpolation scheme has to be used. Different kinds of interpolation schemes exist with varying orders of accuracy and computational cost. The interpolation algorithm is very frequently used within the code and thereby it has a big influence on the computational cost of the particle tracking tool. For this work an inverse distance based interpolation algorithm is preferred because of its rather low computational cost. In this manner the cell whose center is closest to the position of the particle is found out and the velocity vector of the particle is interpolated from the velocity vectors at the vertices of the cell. Also other flow quantities such as the temperature or pressure are also interpolated using the same strategy.

2.3.3. Treatment of the Particles Close to the Walls

The artificial selection of the numerical time step $\Delta\tau$ raised additional complexities for the marching of the particles in the vicinity of the solid walls. The artificial value set for the numerical time step might be well above the time step value dictated by the CFL criterion and might cause some of the particles penetrate into the solid walls which is an unphysical. In order to deal with this numerical issue an impermeability condition is set additionally for the particles within the boundary layer. In that regard, first the particle's velocity vector is decomposed into wall perpendicular and tangential components as shown in Figure 2.18. Afterwards if the particle is very close to the wall its wall perpendicular velocity component is canceled out if it is pointing into the wall. In case that the normal component is directed away from the solid wall it has been kept as it is since there is no danger of collision with the wall in that case. Using this treatment it has been ensured that the particles move parallel to the solid boundary as it is in

reality. This treatment adds additional computational cost but enables to use much higher time step values compared to the one dictated by the CFL criterion and thereby the number of iterations is considerably reduced. So overall, this treatment reduced the computational time considerably. Additionally, this treatment is also very helpful in modeling the impact of the particles with mass with the solid surfaces which can be used in future projects modeling the erosion of the turbomachinery imposed to particulate flow.
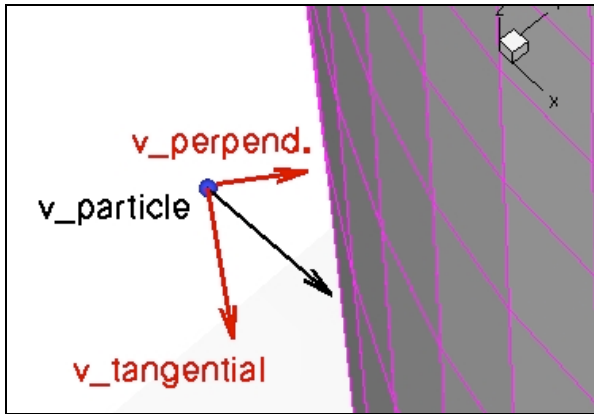
Figure 2.18 Decomposition of the particle's velocity vector into wall perpendicular and into tangential components

2.3.4. Validation

In order to test the accuracy of the numerical method and also the validity of the artificially set numerical time step $\Delta\tau$ a validation study has been conducted where a steady flow field has been considered. In case of steady flows the pathlines corresponds to streamlines by definition which can be drawn by commercial post-processor tools like Tecplot. In Figure 2.19 the predictions of the particle tracking tool are shown with the red dashed lines and the streamlines predicted by Tecplot are in blue. Three streamlines are drawn. Two of these pass close to the suction side of the rotor blades in subsequent passages. And one of them goes through the rotor blade tip gap. The predictions of the in-house tool with the ones of the commercial tool

completely match within the stator passage. Within the rotor the two streamlines moving close to the rotor suction side agree as well. However, there is a deviation in the predictions of these two tools for the other streamline after it has entered the blade tip gap. The high flow gradients and also small mesh sizes require much smaller time steps than the artificially set value. This why the in-house predicted streamline cannot capture the rotation within the tip leakage vortex but rather follows a roughly straight line through the core of it. Depending on the requirements this level of accuracy in the predictions might be low or satisfactory. Within the scope of this work the migration patterns to the rotor blade tip are under investigation rather than the exact paths they follow within the tip gap and downstream. Taking into account that the two predictions match up to the point they reach the rotor tip gap one can say this numerical approach would serve the level of accuracy needed.
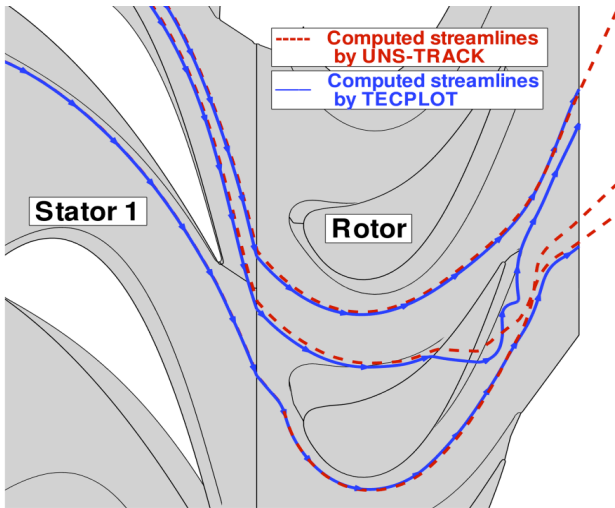

Figure 2.19 The predicted streamlines by "UNS-TRACK" and also by the commercial tool "Tecplot"

3. Experimental Methods

Accompanying this numerical study experimental measurements have been conducted. The experimental data was used both as the inlet boundary conditions and also to validate the predictions of the numerical model. The experimental measurements were conducted in the axial research turbine facility "LISA" at the Laboratory for Energy Conversion at ETH Zurich.

3.1. Axial Turbine Facility "LISA"

The drawing of the experimental facility is shown in Figure 3.1 and its important parts are indicated. The operation conditions of the facility for the turbine geometries used in this study are given in Table 3.1. Further details of the experimental facility are presented by Behr et al. [58] In this study two one-and-a-half stage turbine geometries are considered. The unshrouded turbine geometries are representative of the film cooled HP turbines. The two turbine geometries only differ in the endwall designs of their first stators. In the "LISA-D" case turbine geometry conventional axisymmetric endwall designs have been used in all the three blade rows. On the other hand, in the "LISA-M1" case turbine geometry non-axisymmetric endwall profiling has been applied at the first stator only. The applied profiling at the hub endwall of the first stator is shown in Figure 3.2. The two different first stator designs have the same blade profiles but differ very slightly in their stackings. Because of the additional bumps added at the endwalls the stator with non-axisymmetric endwalls had to be very slightly re-staggered to preserve the position of the throat. The design aspects of the endwall profiling are given by Germain et. al. [21]. In the "LISA-M1" case geometry the rotor and the second stator designs are kept unchanged as they are in the "LISA-D" case. Some details that are shared by both turbine geometries are given in Table 3.2.

For the current experimental study on hot streaks an inlet temperature distortion generator was added to the existing configuration. The layout of the turbine with the positions of the measurement planes and also the

 position of the hot streak generator is shown in Figure 3.3. Time resolved aerodynamic and temperature measurements were carried out at the
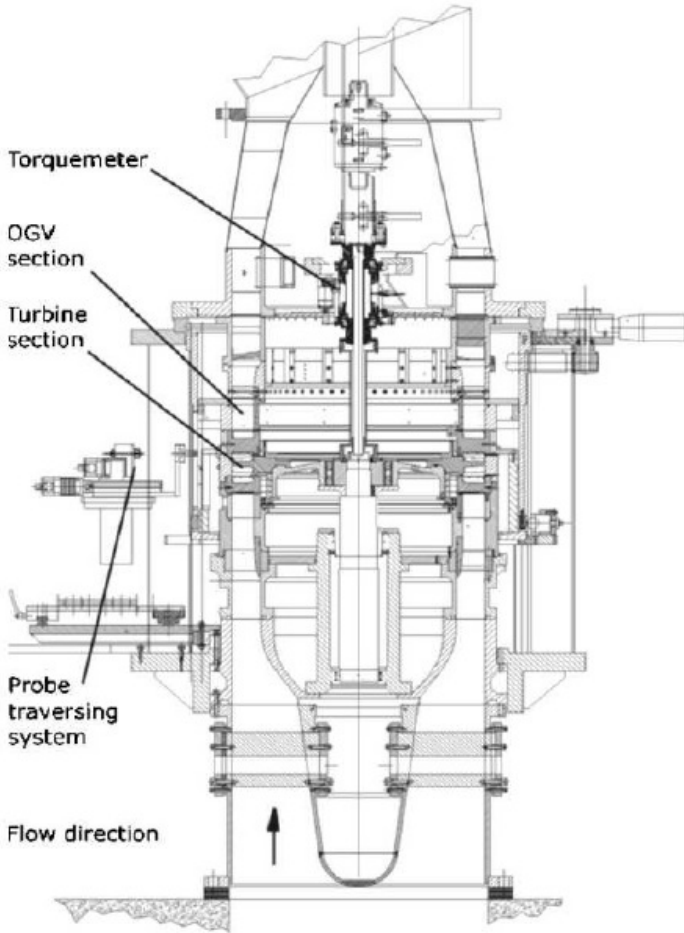

Figure 3.1 Axial Turbine Facility "LISA"

stationary planes indicated by the letters. The measurements at the plane A has been used as the inlet boundary conditions for the solver and the

measurements at the plane C will be used for the validation of the numerical results. Different in-house developed probe technologies have been utilized in the experimental measurements. The Fast Response Entropy Probe "FENT" [63] is capable of measuring the unsteady temperature, pressure and the flow angles but the operating range of the probe is limited to about 110°C. On the other hand, a recent developed High Temperature Fast Response Aerodynamic Probe "FRAP-HT" [64] is capable of conducting unsteady aerodynamic measurements up to 260°C. But it can conduct only steady temperature measurements. Due to the different capabilities and limitations of each of these probe technologies both of them have been used in a collaborative manner.

Table 3.1 Operating conditions of the turbine for the present study

	Variable	Value	Unit
Turbine	Rotor Speed (Ω)	2700	rpm
	Pressure Ratio (1.5 Stage, total–to–static)	1.65	-
	Total Inlet Pressure	1.4	bar
	Mass flow	11.8	kg/s
	Shaft Power	292	kW
	Hub / Tip diameter	660. / 800.	mm
1st stage	Pressure ratio (total–to–total)	1.35	-
	Degree of reaction	0.39	-
	Stage loading coefficient $\Psi = \Delta h_0 / (r\Omega)^2$	2.36	-
	Flow Coefficient $\phi = V_x / (r\Omega)$	0.65	-
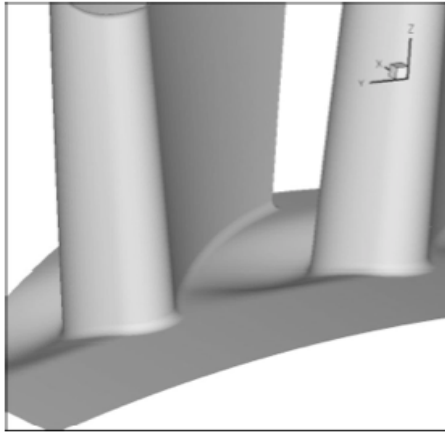
Figure 3.2 Non-axisymmetric endwall profiling design applied to the hub endwall of the stator 1 in the "LISA-M1" geometry [21]

Table 3.2 Specifications of the "LISA-D" case turbine geometry

	Stator 1	Rotor	Stator 2
Number of blades	36	54	36
Inlet flow angle	0°	54°	-42°
Outlet flow angle	73°	-67°	64°
Solidity (chord / pitch)	1.27	1.41	1.34
Aspect ratio (span / chord)	0.87	1.17	0.82
Exit Mach number	0.54	0.50	0.48
Reynolds number	7.1×10^5	3.8×10^5	5.1×10^5
Blade Span	70 mm	69.3 mm	70 mm
Clearance / Span	0 %	1 %	0 %

3.2. Hot Streak Generator

Details of the design of the hot streak generator are given in [65]. The outlet pipe of the hot streak generator is designed to be dismountable enabling mounting of the different tube geometries. In this manner different hot streak shapes could be generated. In this study two different hot streak shapes have been considered. Their specifications and the intents of their designs are explained below.

Figure 3.3 Layout of the turbine with the measurement planes and the hot streak generator

3.2.1. Circular Hot Streak

For the first experimental campaign two circular hot streak shapes at two different peak temperature levels have been considered. The low and the high temperature hot streaks have the peak to mean temperature ratios of about 1.18 and 1.30 respectively. Time resolved temperature and
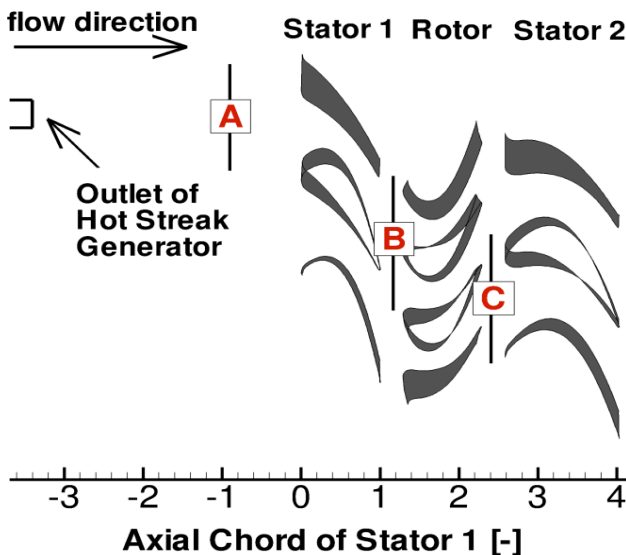
aerodynamic measurements have been conducted using the "FENT" probe technology for the low temperature hot streak case. Due to the temperature limitation of this probe, the "FRAP-HT" probe has been utilized for the measurements with the high temperature hot streak. "FRAP-HT" has a much higher temperature range but can only deliver steady temperature measurements. The experimentally measured, time averaged, total temperature distribution measured upstream of the turbine at the A-plane has been shown in Figure 3.4 for the low temperature hot streak case. The circumferentially mass averaged, experimentally measured total temperature profiles are shown in Figure 3.5 for both of the hot streak cases.

Circular hot streaks with different sizes and temperature ratios have been considered in the literature. In a recent study by Povey and Qureshi [8] about the development of a combustor simulator, the real temperature distribution downstream of the combustor of a modern aircraft engine is taken as a basis. The present hot streaks generated in this study are compared with the same data from the real combustor measurement. In the data published by Povey and Qureshi [8] the peak to mean temperature ratio is shown to be 1.21. In this aspect both of the circular hot streaks are similar to the real engine data. Among all the other aspects the peak-to-mean temperature ratio is the most dominant one affecting the hot streak migration physics. The circumferentially mass averaged temperature profile is another important aspect to consider. As shown in Figure 3.5 the peaks reach a temperature ratio of 1.05 at 46% blade span for the low temperature hot streak case and reach a temperature ratio of 1.08 at 49% blade span for high temperature ratio hot streak case. However, the same temperature ratio reaches to about 1.17 at 58% blade span in the real engine data. The lower ratios of the generated circular hot streaks are due to their relatively small sizes compared to the one in the real engine. Also the hot streaks are positioned at slightly lower spanwise positions compared to the data given in [8]. However, despite the differences of the generated hot streaks from the real engine data they can serve very well for the purpose of studying the fundamentals of the hot streak migration within the turbine stage.
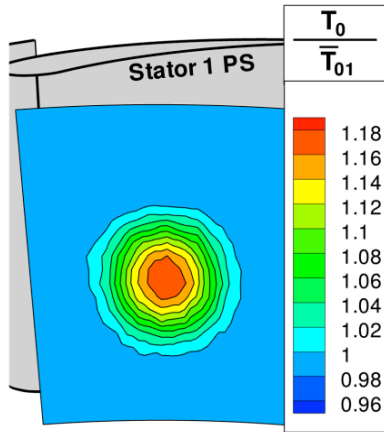
Figure 3.4 Time averaged, measured total temperature distribution upstream of the turbine (plane A) visualizing the low temperature hot streak
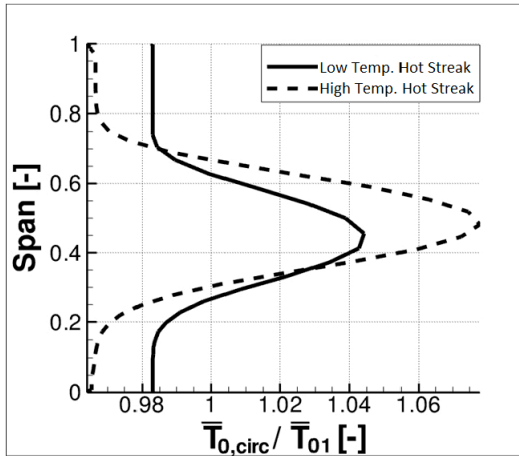

Figure 3.5 Circumferentially mass averaged total temperature profiles for both hot streaks generated

3.2.2. Non-symmetric Hot Streak Shape

For the second experiment a non-symmetric hot streak shape has been considered. The motivation behind the non-symmetric hot streak shape was the reduction in the combustor outlet circumferential temperature gradients especially around the midspan over the recent years. The advances in the combustor technology to ensure a low NOx operation character enforced more uniform temperature distributions at the combustor outlet. As mentioned before, the combustor outlet temperature distributions depend on the type of application and vary from one combustor type to another. However, the scarce data on the real combustor outlet temperature distributions published in the open literature confirms the trend in the reduction in the circumferential temperature gradients. Barringer et. al. [66] have designed a combustor simulator that generated a variety of turbine inlet profiles representative of the actual engine conditions. On the contrary of the circular hot streak shapes mainly considered in the literature where the temperature gradients in circumferential and radial directions are comparable the generated temperature distributions had stronger radial gradients compared than the circumferential ones. At mid-span the circumferential variations for the total temperature reached a maximum of only ± 0.5%. In the numerical work of Tarasov et. al. [67] about the analysis of the combustor outlet temperature non-uniformity a section of the modern double annular combustor used in mid-power class stationary gas turbine has been simulated. In Figure 3.6 the 20° section of the annular combustor is shown. 60 fuel injectors are distributed around the two rings. This configuration is developed to ensure a low NOx operation character at different load levels. All the fuel injectors have been placed in a common liner ensuring a more uniform circumferential temperature distribution. The numerical predictions of the NOx level and also the temperature distribution have been validated with the measurements. Figure 3.7 shows the numerically predicted temperature distribution at the combustor outlet at peak load. The peak temperatures are around 1900K. The test section which was simulated has 10 fuel injectors distributed into two rows. Their traces are also visible in the temperature distribution downstream of the combustor. Along the midspan weak temperature gradients are present but closer to the endwalls the gradients increase both in circumferential and in radial directions. Close to the shroud a wavy pattern in the temperature

distribution is observed which shows a periodicity with the number of the fuel injectors. As the temperature gradients are relatively pronounced at this region a local modification in the temperature distribution might be considered that would have a beneficial effect on the aerothermal performance of the turbine and the life time of the rotor blade tips.

Figure 3.6 20° model of a real double annular combustor used in mid-power range stationary gas turbines [67]
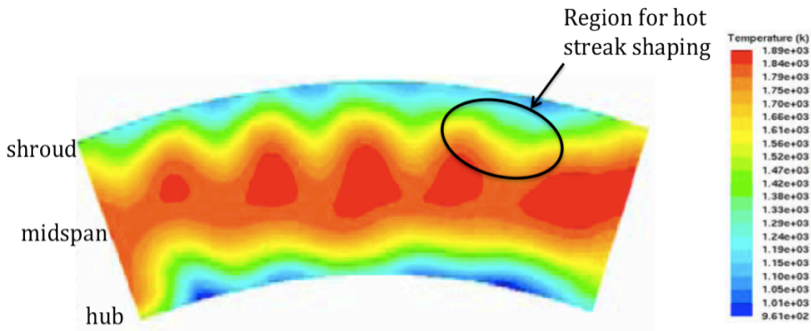
Figure 3.7 Simulated temperature field at the exit of the combustor section [67]
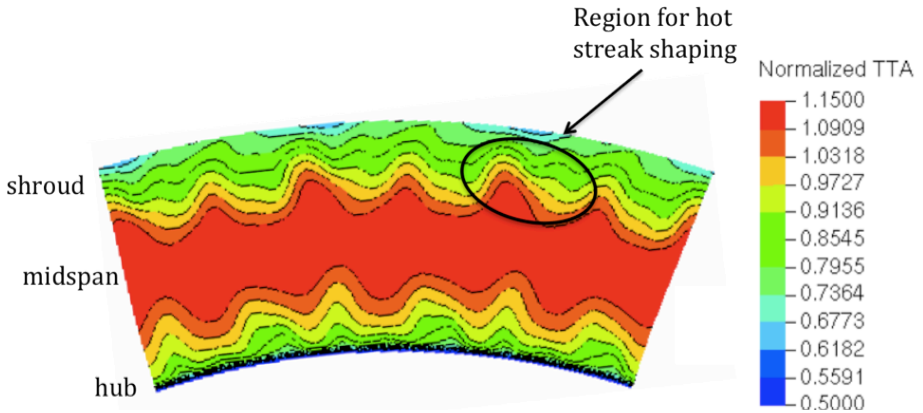
Figure 3.8 Combustor exit temperature distribution obtained via General Electric's proprietary combustion software CONCERT-3D [68]

In another numerical work Felten et. al. [68] have considered the effect of the two-dimensional realistic combustor exit conditions on the turbine of a modern aircraft engine. The temperature distribution that they have used in their simulations is shown in Figure 3.8 which resulted from their in-house combustor simulator. There are similarities between the two temperature distributions shown in Figure 3.7 and Figure 3.8. Along the midspan very low temperature gradients exist but they become considerable close to the endwalls. Moreover, a similar wavy pattern also exists in both of the figures where the temperature distribution can be modified in favor of the turbine performance and life time. The consistency of the temperature distributions in the aspects mentioned above motivated to generate a non-symmetric hot streak shape modeling the wavy pattern in the temperature distribution close to the endwalls. In that regard a new outlet duct has been designed for the hot streak generator shown in Figure 3.9 that would result in a non-symmetric temperature distribution at the turbine inlet. The details of the design of the new outlet tube for the hot streak generator are given in [69].
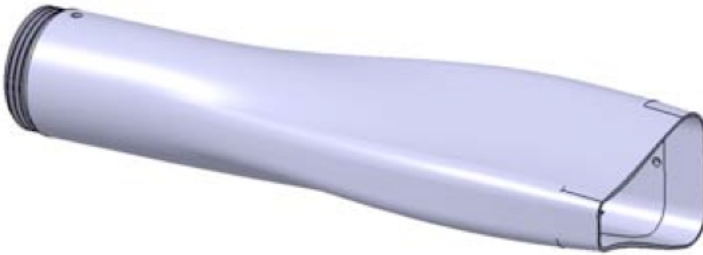
Figure 3.9 Outlet duct of the hot streak generator designed for the non-axisymmetric hot streak shape
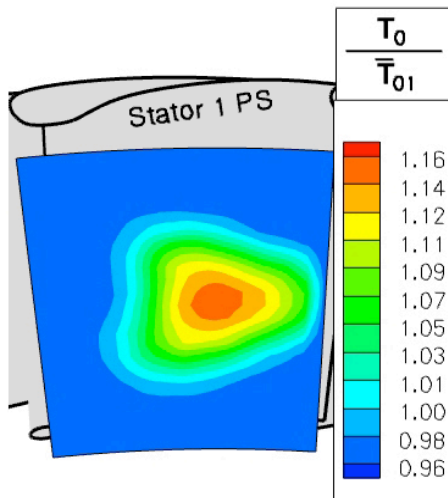
Figure 3.10 Experimentally measured total temperature distribution upstream of the turbine (plane A)

The temperature distribution measured upstream of the turbine at the plane A is shown in Figure 3.10. The temperature gradients at midspan are reduced compared to the circular hot streak and get more pronounced close to the endwalls due to its non-symmetric shape similar to the temperature distributions shown in Figure 3.7 and Figure 3.8. For the experimental

study the hot streak shape is adjusted such that its spanwise larger part impinges on the pressure side of the stator. The peak to mean temperature ratio is about 1.16 and in terms of the size the hot streak covers an area two times the size of the circular hot streak shown in Figure 3.4. With these characteristics it resembles to the temperature non-uniformities observed in modern full annular combustors.

4.   A New, Anisotropic Scaling Approach for Artificial Dissipation

Modeling of the high Reynolds number flows is numerically challenging. Due to the low level of the physical diffusion the errors can build up during the iteration unless they are numerically damped. Therefore a certain level of artificial diffusion has to be present in the numerical scheme to ensure the stability of the method. Nevertheless, the introduction of the artificial numerical dissipation can severely affect the accuracy of the scheme if it is not done with care. Minimizing the level of artificial diffusion without sacrificing from the stability of the solver is a key issue for the accuracy of the solvers. For example, due to the highly diffusive character the use of the first order upwind scheme is severely restricted in the modern CFD solvers in spite of its high stability. On the other hand, the spatially second order schemes have a much lower inherent diffusive character but they may lack the required numerical stability unless additional numerical dissipation is added.

There are two main approaches for adding the artificial smoothing. The so called modern high resolution schemes rely on the flux limiters. In this method the fluxes are calculated from a combination of the non-oscillatory first order upwind discretization and an oscillatory second order contribution. In smooth regions the contribution of the second order terms are kept and the second order spatial accuracy of the solver is preserved. On the other hand, in the vicinity of the discontinuities the second order terms are limited via limiting functions and in extreme they are completely omitted. In that case the space discretization is locally switched to first order upwind scheme and the numerical oscillations are prevented. In this approach, the artificial numerical diffusion is added in an implicit way by using the inherent diffusive character of the first order upwind scheme.

In the other main approach, artificial numerical diffusion is added in an explicit manner usually in the form of second order and fourth order spatial derivatives. This approach has been mainly used for the schemes utilizing the central space discretization that inherently does not include any numerical damping. This is why it has to be introduced in an explicit way. The high frequency artificial oscillations occurring in smooth regions can be damped via fourth order numerical smoothing. This way the second order spatial accuracy of the scheme is kept in smooth regions of the domain since the added fourth order smoothing has a third order spatial accuracy. On the other hand, in the vicinity of the discontinuities the second order smoothing is activated via a switch and second order smoothing is applied which effectively modifies the central space discretization into the first order upwind discretization and numerical oscillations are prevented. This form of non-linear artificial dissipation, known as the JST scheme, has been developed by Jameson, Schmidt and Turkel [70] and successfully applied to the fourth order Pulliam [71] time integration scheme for solving the Euler equations. The scheme showed excellent shock capturing properties and became very popular for the aerospace applications. Later on the same formulation has been applied by Pulliam and Steger [62] into the Beam and Warming scheme. [72]

Each of these schemes has its advantages and disadvantages. With the flux limiting approach there is a more direct control on the amount of numerical diffusion for each of the flow variables. Because of this reason, this method is known to be superior for resolving the shocks. However, since this approach is based on the first order upwind discretization the fluxes have to be split according to the direction of the characteristics which is computationally expensive. Secondly, the limiter functions do not take into account the local physical diffusion present in the flow. In RANS approach turbulence is modeled as an additional form of viscosity called the eddy viscosity that might reduce the need to the numerical diffusion.

Compared to the flux limiting approach central schemes with the addition of the explicit form of numerical smoothing are computationally much less expensive. Unlike in the upwind space discretization the direction of the characteristics has not to be taken into account in the central space discretization. In this method the coefficients for the artificial numerical smoothing have to be set by the user. Unfortunately, depending on the mesh

quality and the flow scenario these coefficients might need to be altered. Coefficients that might work well for a mesh might not be high enough for another one or they might lead to excessive smoothing for some other cases. So the user has to be aware of that and play with these coefficients when needed. This additional user input is the main disadvantage of this method and requires more educated users to reach to the best accuracy. Additionally, this approach is usually less accurate resolving the discontinuities like shock waves compared to the flux limiting approach. More accurate versions of this scalar dissipation approach known as matrix dissipation schemes can be found in the literature [73]. They show very similar shock resolving characteristics with the upwind schemes. But the computational cost is also considerable increased.

In this chapter an anisotropic method for the scaling of the high order smoothing coefficient of the scalar, non-linear artificial dissipation scheme of Jameson, Schmidt and Turkel [70] has been developed and applied to Ni's Lax-Wendroff scheme. [39] The method has been developed to increase the level of the accuracy of the RANS simulations in high aspect ratio boundary layer cells and also in shear dominated regions especially in internal flow simulations such as the secondary flow features inside multi-row turbomachinery. The developed method has been tested for accuracy on the laminar and turbulent flat plate scenarios and also on multi-row axial turbomachinery flows.

4.1. Isotropic Artificial Dissipation Scheme - (Baseline Approach)

The in-house compressible RANS solver "MULTI3" is based on the Ni-Lax-Wendroff [39] algorithm offering a second order accuracy both in time and in space. The scheme is derived carrying out a Taylor expansion in time where only the first and second order terms are kept. The first order time derivatives are calculated carrying out a flux balance around the cell boundaries using the central space discretization. Without the second order time derivatives the scheme is equal to the unconditionally, unstable central scheme. Via the second order time derivatives numerical diffusion is introduced and the scheme becomes numerically stable by itself. However, under certain conditions which will be explained more in detail the scheme

might require external artificial numerical smoothing to ensure stability. To damp the high frequency oscillations that may arise due to the central space discretization in Ni's Lax-Wendroff discretization a fourth order artificial dissipation is added in smooth portions of the solution. However, in the vicinity of the shocks it is replaced by the second order artificial dissipation. The shocks are detected by a switch proposed by Von Neumann and Richtmeyer [74]. The second order smoothing coefficient is calculated as

$$\kappa^{(2)} = \varepsilon^{(2)} \left\{ \begin{array}{ll} \rho M^2 \left| div\left(\vec{v}\right) \right|, & div\left(\vec{v}\right) < 0 \\ 0, & div\left(\vec{v}\right) \geq 0 \end{array} \right\}$$

Eq 4.1

In smooth regions of the flow the high order artificial dissipation is dominant. To reduce the excessive dissipation inside the boundary layers the smoothing coefficient is scaled with the local Mach number as shown in Eq 4.2.

$$\kappa^{(4)} = \varepsilon^{(4)} \left(M / M_{ref} \right)^2$$

Eq 4.2

The contribution of the cell A to the residual of the cell vertex i,j due to the artificial dissipation is calculated as

$$\delta Q_{(i,j)A} = \left(\frac{\Delta t}{V} \right)_{i,j} \left\{ \kappa_A^{(2)} \left(\frac{V}{\Delta t} \right)_A \left(\overline{\rho_A} - \rho_{i,j} \right) - \kappa_A^{(4)} \left(\frac{V}{\Delta t} \right)_A \left(\overline{\nabla^2 \rho_A} - \nabla^2 \rho_{i,j} \right) \right\}$$

Eq 4.3

In the isotropic smoothing approach the $(V/\Delta t)$ ratio is used for the scaling of the smoothing coefficients which is a cell based quantity. Moreoever, the difference operators are also calculated based on the cell averaged states and the local values at the cell vertices. Cell averaged states for the state vector itself and its Laplacian is calculated as

$$\overline{Q_A} = \frac{1}{4}\left(Q_{i,j} + Q_{i+1,j} + Q_{i,j+1} + Q_{i+1,j-1}\right)$$

$$\overline{\nabla^2 Q_A} = \frac{1}{4}\left(\nabla^2 Q_{i,j} + \nabla^2 Q_{i+1,j} + \nabla^2 Q_{i,j+1} + \nabla^2 Q_{i+1,j-1}\right)$$

Eq 4.4

Laplacians are calculated using the approach of Holmes and Connell [75]. The weights introduced into Eq 4.5 are to account for the non-uniformities in the mesh. For a fairly smooth mesh the weights for the stencil are close to 1.

$$\nabla^2 Q_{i,j} = \psi_{i+1,j}Q_{i+1,j} + \psi_{i-1,j}Q_{i-1,j} + \psi_{i,j+1}Q_{i,j+1} + \psi_{i,j-1}Q_{i,j-1} - 4Q_{i,j}$$

Eq 4.5

Further details of the scheme and its implementation can be found in [76].

4.1.1. Inaccuracies about the Isotropic Artificial Dissipation Scheme

Later on, the code is converted to a viscous solver and accordingly minor modifications related to the reduction of the numerical smoothing in boundary layers have been added to the smoothing algorithm. The smoothing coefficients are scaled according to the square of the local Mach number. This simplistic approach is used to prevent excessive numerical smoothing within the boundary layers. One of the major differences of the viscous simulations from the inviscid ones is the presence of the boundary layers which are usually resolved by cells stretched in the streamwise direction. The high aspect ratio cells are used inside the O-grids where the mesh is very far from isotropy. Utilizing an isotropic smoothing algorithm within the anisotropic regions of the mesh can seriously decrease the accuracy of the solver. Even though the velocity profiles within the boundary layers can be calculated reasonably well with this approach, it is especially difficult to get the wall shear stress level correct. Usually, the stress level at the wall shows severe artificial oscillations and increasing the

smoothing coefficients do not also help since in that case the stress level at the wall is underpredicted. The inaccuracy of the solver especially at the wall severely restricts the use of the solver for the heat transfer simulations unless the cell aspect ratios are kept low which is usually computationally infeasible.

The problem related to the wall shear is demonstrated on the viscous, laminar flow on a no-slip flat plate. Figure 4.1 shows the calculated shear along the flat plate alongside the analytical solution. As shown, the result starts to become oscillatory after a certain streamwise position. Due to the expansion of the cells in streamwise direction the cell aspect ratios are increased from the inlet to the outlet of the domain. And after a certain aspect ratio the isotropic smoothing algorithms cannot handle both the stability and the accuracy and oscillations start to grow. This situation is even more severe in turbulent boundary layers where the cell aspect ratios are much higher.
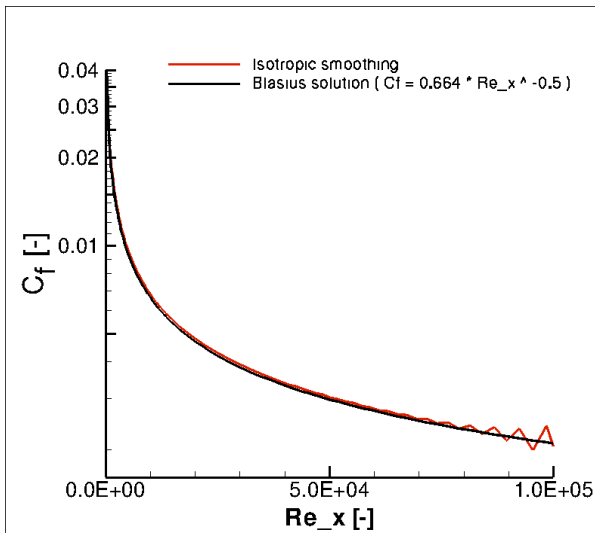

Figure 4.1 Evolution of the wall shear along the flat plate simulated with the Mach number scaled isotropic smoothing approach

4.2. A New, Anisotropic Scaling Approach for the Scalar Artificial Dissipation Scheme

A new anisotropic approach for the scaling of the smoothing coefficients is next developed for the JST [70] type scalar, nonlinear artificial dissipation scheme and applied to the Ni's Lax –Wendroff scheme. First, the JST artificial dissipation scheme modified by Swanson, Radespiel and Turkel [77] to improve the accuracy for the viscous simulations is briefly discussed. In this approach the dissipation is composed of second and fourth order central differencing operators. Fourth order dissipation is needed to damp the high frequency oscillations that the central differencing is prone to. In the vicinity of the shocks the second order artificial dissipation is activated and the shocks are sensed by the pressure sensor defined as

$$\nu_{i,j} = \left| \frac{p_{i+1,j} - 2p_{i,j} + p_{i-1,j}}{p_{i+1,j} + 2p_{i,j} + p_{i-1,j}} \right|$$

Eq 4.6

Moreover, in regions where the second order artificial dissipation is activated the high order smoothing is locally deactivated. Accordingly, the two smoothing coefficients are calculated as

$$\kappa^{(2)}_{i+\frac{1}{2},j} = \varepsilon^{(2)} \max(\nu_{i+1,j}, \nu_{i,j}) \qquad \kappa^{(4)}_{i+\frac{1}{2},j} = \max(0, \varepsilon^{(4)} - \kappa^{(2)}_{i+\frac{1}{2},j})$$

Eq 4.7

The contribution of the cell A to the residual of the cell vertex i,j due to the artificial dissipation is calculated as

$$\delta Q_{(i,j)A} = \left(\frac{\Delta t}{V}\right)_{i,j} \left\{ \kappa^{(2)}_{i+\frac{1}{2},j} \lambda_{i+\frac{1}{2},j} \left(Q_{i+1,j} - Q_{i-1,j}\right) + \kappa^{(2)}_{i,j+\frac{1}{2}} \lambda_{i,j+\frac{1}{2}} \left(Q_{i,j+1} - Q_{i,j-1}\right) \right\}$$

$$- \left(\frac{\Delta t}{V}\right)_{i,j} \left\{ \kappa^{(4)}_{i+\frac{1}{2},j} \lambda_{i+\frac{1}{2},j} \left(\nabla^2 Q_{i+1,j} - \nabla^2 Q_{i-1,j}\right) - \kappa^{(4)}_{i,j+\frac{1}{2}} \lambda_{i,j+\frac{1}{2}} \left(\nabla^2 Q_{i,j+1} - \nabla^2 Q_{i,j-1}\right) \right\}$$

<div align="right">Eq 4.8</div>

In the anisotropic scaling approach the differences are calculated separately along the different cell directions. For the scaling of the smoothing coefficients the largest absolute eigenvalue of the flux Jacobian matrix is used instead of the (V/Δt) ratio which was used in the isotropic smoothing approach. For low aspect cells both scaling methods are comparable.

$$\lambda_{i+\frac{1}{2},j} = \left(\left|vS_x - uS_y\right| + c\sqrt{S_x^2 + S_y^2}\right)_{i+\frac{1}{2},j} \quad \text{for the i-direction}$$

$$\lambda_{i,j+\frac{1}{2}} = \left(\left|vS_x - uS_y\right| + c\sqrt{S_x^2 + S_y^2}\right)_{i,j+\frac{1}{2}} \quad \text{for the j direction}$$

<div align="right">Eq 4.9</div>

For the high aspect ratio cells an anisotropy in the calculation of the smoothing coefficients has to be introduced. In the individual eigenvalue scaling approach [78] [79] the smoothing coefficients in a cell direction are scaled only with the eigenvalue calculated in that particular cell direction. However, this approach may lead to excessive dissipation along the squeezed cell direction and to very low amount of dissipation along the elongated cell direction. In [77] the individual eigenvalue scaling is combined with the isotropic eigenvalue scaling where the three eigenvalues calculated in each cell directions are averaged out. This way the eigenvalue along the squeezed cell direction is reduced and the eigenvalue calculated in elongated cell direction is increased. However, in the present study a complete individual eigenvalue scaling approach is followed and the issue with the scaling of the smoothing coefficients in high aspect ratio cells is dealt by adjusting the level of the higher order smoothing coefficient $\kappa^{(4)}$

itself after investigating the damping characteristics of the numerical scheme used.

4.3. Damping Characteristics of Lax-Wendroff Scheme

The damping characteristics of the Lax-Wendroff method are evaluated on the one-dimensional, linear convection equation.

One-dimensional Linear Convection Equation :

$$u_t + au_x = 0$$

Eq 4.10

The Lax-Wendroff scheme leads to the following discretized form.

$$u_i^{n+1} = u_i^n - \frac{a\Delta t}{2\Delta x}\left(u_{i+1}^n - u_{i-1}^n\right) + \frac{a^2\Delta t^2}{2\Delta x^2}\left(u_{i+1}^n - 2u_i^n + u_{i-1}^n\right)$$

Eq 4.11

Using the definition for the CFL number $\sigma = a\,\Delta t/\Delta x$

$$u_i^{n+1} = u_i^n - \sigma\left[\frac{1}{2}\left(u_{i+1}^n - u_{i-1}^n\right) - \frac{\sigma}{2}\left(u_{i+1}^n - 2u_i^n + u_{i-1}^n\right)\right]$$

Eq 4.12

The last term on the right hand side of Eq 4.12 is the contribution of the second order time derivative and stabilizes the scheme due to its diffusive character. Without this term the scheme would be equal to the unstable central scheme. As one can see the diffusive character of the scheme depends on the CFL number. In the extreme case σ = 1 the scheme is converted to the first order upwind scheme. The first order upwind discretization for this linear partial differential equation is shown in Eq 4.13.

$$u_i^{n+1} = u_i^n - \sigma\left[\frac{1}{2}\left(u_{i+1}^n - u_{i-1}^n\right) + \frac{1}{2}\left(u_{i+1}^n - 2u_i^n + u_{i-1}^n\right)\right]$$

Eq 4.13

One can analyze the damping characteristics of the schemes for this linear convection equation via Von Neumann analysis. In this analysis the solution at any time step n+k is decomposed into its harmonics. A particular harmonic can be represented as shown in Eq 4.14 where V_j^{n+k} represents the amplitude of a particular harmonics j at the time step n+k.

$$u_{i+m}^{n+k} = V_j^{n+k} e^{I(i+m)\phi_j}$$

Eq 4.14

In Eq 4.14 Φ_j is the phase angle for a particular harmonics j and defined as

$$\phi_j = k_j \pi / N$$

N: *the number of the cells,*

k_j: *the wave number.*

Substituting the Eq 4.14 into the discretized form of the Lax-Wendroff equation shown in Eq 4.12 one can calculate the change in the amplitude of all the harmonics present in the domain.

$$V_j^{n+1} e^{Ii\phi_j} = V_j^n e^{Ii\phi_j} - \frac{\sigma}{2}\left(V_j^n e^{I(i+1)\phi_j} - V_j^n e^{I(i-1)\phi_j}\right) + \frac{\sigma^2}{2}\left(V_j^n e^{I(i+1)\phi_j} - 2V_j^n e^{Ii\phi_j} + V_j^n e^{I(i-1)\phi_j}\right)$$

Eq 4.15

Using the definition of the amplification factor

$$G_j = \frac{V_j^{n+1}}{V_j^n} = 1 - \frac{\sigma}{2}\left(e^{I\phi_j} - e^{-I\phi_j}\right) + \frac{\sigma^2}{2}\left(e^{I\phi_j} - 2 + e^{-I\phi_j}\right)$$

The amplification factor G can be written in the polar form as

$$G_j = \frac{V_j^{n+1}}{V_j^n} = 1 - I\sigma\sin(\phi_j) + \sigma^2\left(\cos(\phi_j)-1\right)$$
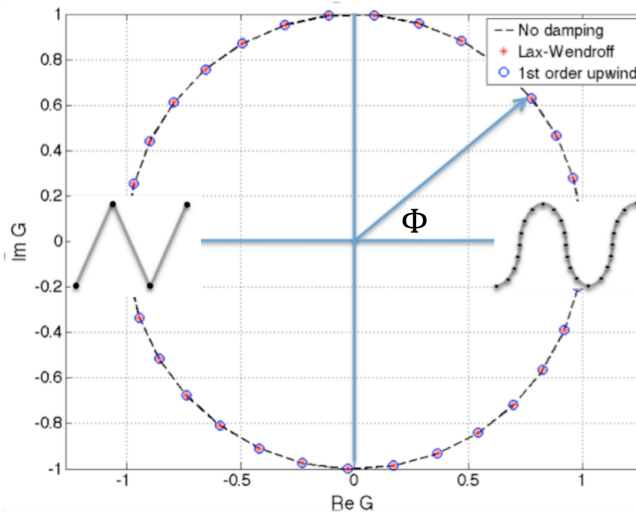
Eq 4.16

Figure 4.2 Damping characteristics of the Lax-Wendroff and first order upwind schemes at CFL = 1.0

In Figure 4.2 the amplification factors for the Lax-Wendroff and for the first order upwind schemes are plotted in the complex plane for all the possible phase angles ($0 \leq \Phi_j \leq \pi$) for $\sigma = 1$. Small values of Φ_j represent the waves resolved with a large number of grid nodes and large values of Φ_j represent the waves that are resolved with a few grid points. The highest resolvable frequency is reached at $\Phi_N = \pi$ where the wave is resolved with only two cells. For the stability of the scheme the following condition has to be fulfilled.

$$|G| \leq 1.0$$

In Figure 4.2 the boundary of the stability region $|G|=1$ is shown with the dashed circle. According to the stability condition the amplification factor G should not go beyond the borders of the dashed circle. At $\sigma = 1$ both schemes do not show amplitude damping for any of the harmonics even for the highest one. However, at this limit both schemes are non-oscillatory; high frequency oscillations do not form unless they were introduced in the initial solution. As the CFL number is reduced especially the amplitude of the higher harmonics start to be damped by the inherent dissipation within the schemes. Even though both schemes behave the same at $\sigma = 1$, at lower CFL numbers the Lax-Wendroff scheme preserves the amplitude of the low frequency waves to a larger extent due to its second order character. However, it also loses the non-oscillatory character whereas the upwind scheme keeps even at low CFL numbers. The lower the CFL number the higher is its tendency to develop spurious oscillations.
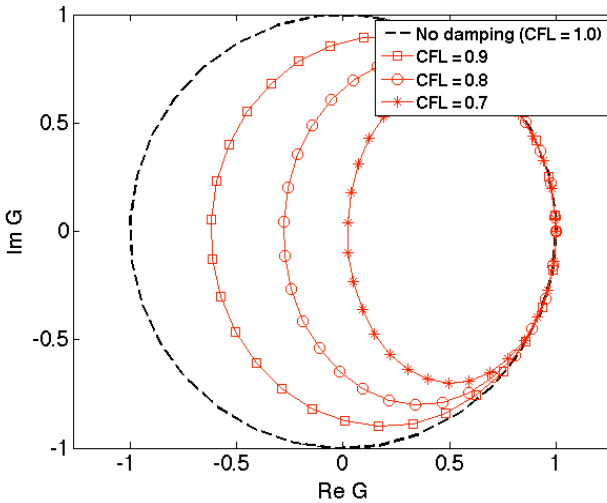

Figure 4.3 Damping characteristics of the Lax-Wendroff scheme for high CFL numbers

In Figure 4.3 and in Figure 4.4 the damping characteristics for CFL > 0.7 are shown for the Lax-Wendroff and for the first order upwind schemes respectively. At high CFL numbers $(0.7 < \sigma < 1.0)$ the Lax-Wendorff

scheme increasingly damps the amplitudes of the high frequency waves (Φ = π) as the CFL number is reduced. In the complex plane representation the circle representing the amplification factor at σ = 1.0 deforms into an ellipse shifted towards the positive real axis. And at about σ = 0.7 the damping for the high frequency waves reaches to a maximum. On the other hand, maximum damping for the high frequency modes is reached at σ = 0.5 for the first order upwind scheme showing a more gradual change in the damping behavior.
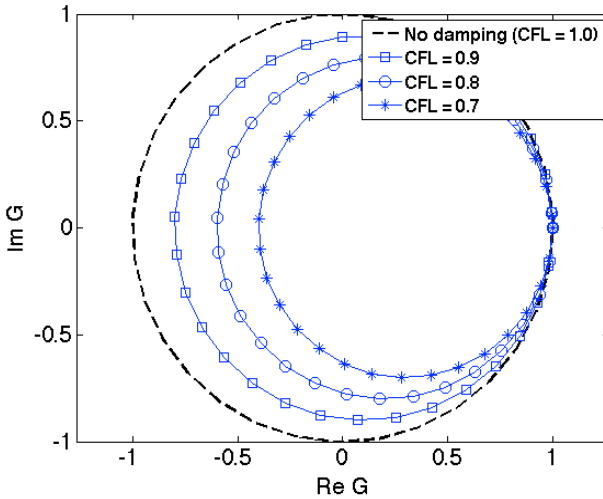
Figure 4.4 Damping characteristics of the first order upwind scheme for high CFL numbers

For σ < 0.7 the ellipse is confined to the right hand side of the imaginary axis and the amplitudes of all the harmonics are less and less damped as the CFL number is reduced. This is because the dissipation term in the Lax-Wendroff scheme is proportional to the CFL number and as the CFL number is reduced its effect become less dominant and the scheme approaches to the unconditionally unstable central scheme. At these low CFL numbers artificial higher order oscillations might appear due to the reduction in the inherent damping characteristics of the scheme. In this case explicit higher order smoothing is explicitly needed to damp the

oscillations. In Figure 4.5 the damping characteristics for the Lax-Wendroff scheme for the low CFL numbers are shown.
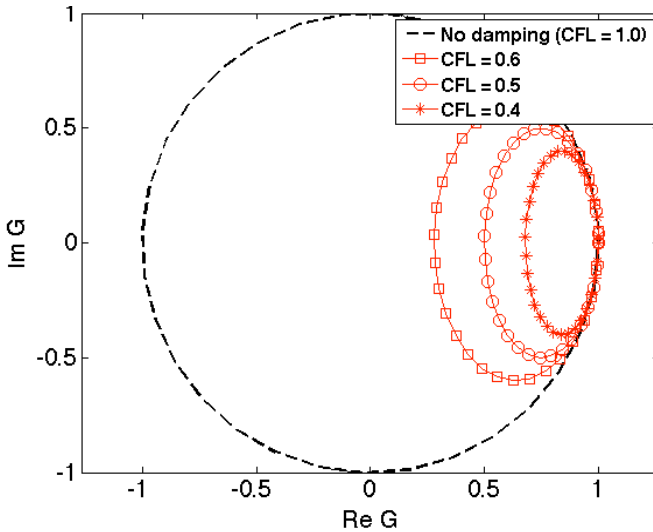

Figure 4.5 Damping characteristics of the Lax-Wendroff scheme for low CFL numbers

The outcomes of this linear stability analysis are next tested on the non-linear Navier-Stokes equations on a simple test problem. In this regard, the flow inside a three-dimensional rectangular domain is numerically calculated at different CFL numbers without using any explicit artificial numerical smoothing. A uniform, Cartesian mesh without any clustering has been used. The dimensions of the flow domain and the number of the cells at each dimension are given in Figure 4.6. A uniform, axial flow conditions are imposed at the inlet boundary. The Mach number is set to 0.15. Slip wall boundary conditions are imposed at the two walls in the XY plane. At the sides of the domain periodic boundary conditions have been imposed. The Reynolds number is kept high to have negligible viscous effects. The same flow scenario has been simulated at three different CFL numbers (0.6, 0.3 and 0.13). The number of iterations is increased anti-proportionally with the CFL number such that all the simulations reach to

the same time. The solutions are compared with respect to the analytical solution of this 1D problem. Figure 4.7 shows the relative error distribution in the Mach number level at the XZ plane for all the three cases. Even though the level of the error is quite low for all the three cases the high frequency errors increase considerably as the CFL number is decreased. This observation is consistent with the findings of the linear stability analysis. These high frequency errors are formed due to the uncoupling of the even and the odd mesh points. The only mechanism that can counteract this behavior is the inherent numerical dissipation of the scheme. At high CFL numbers the dissipation is quite effective in damping these high frequency waves. However, at low CFL numbers the damping of the scheme reduces and they become more and more visible in the solution. Unless explicit high order artificial dissipation is applied they won't be damped by the scheme itself.
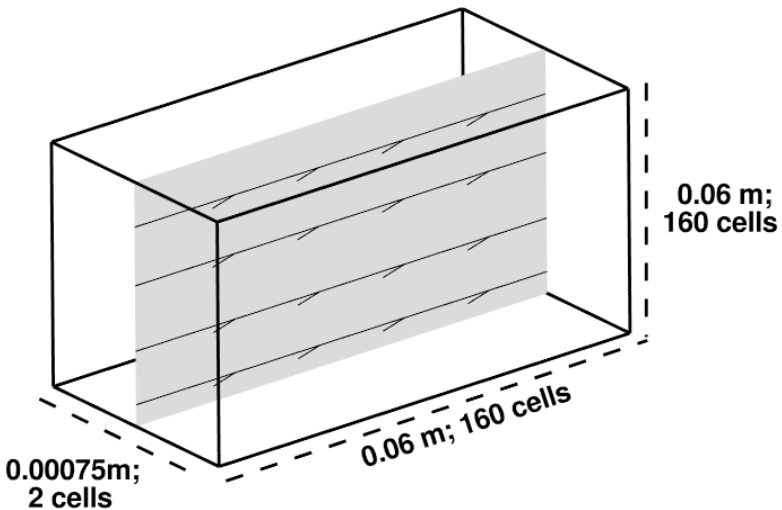
Figure 4.6 Computational domain dimensions
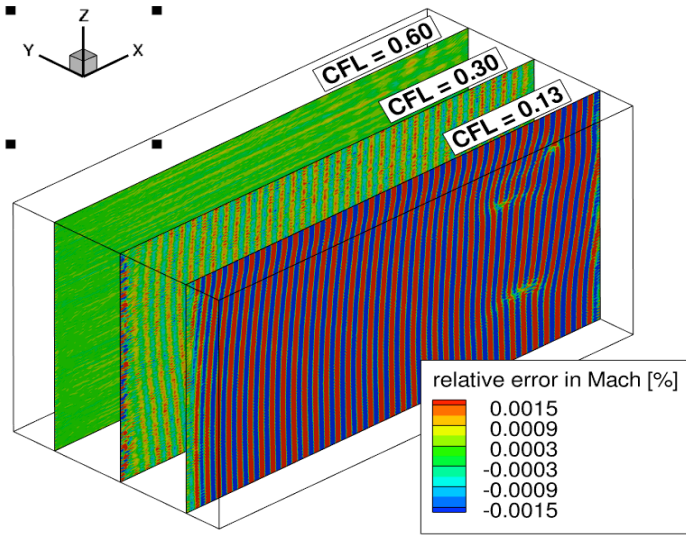
Figure 4.7 Error distribution of the u-momentum at the x-z plane for different CFL (without explicit artificial smoothing)

One-dimensional Linear Convection Equation (with explicit artificial dissipation) :

Before adding the artificial dissipation to the linear convection equation its discretized form is reformulated as

$$u_i^{n+1} = u_i^n - \left(\frac{a\Delta t}{\Delta x_i}\right)\left[\frac{1}{2}\left(u_{i+1}^n - u_{i-1}^n\right) - \frac{a\Delta t}{2\Delta x_i}\left(u_{i+1}^n - 2u_i^n + u_{i-1}^n\right)\right]$$

The high order smoothing term is added as shown in Eq 4.17.

$$u_i^{n+1} = u_i^n - \left(\frac{\Delta t}{\Delta x_i}\right)\left[\frac{a}{2}\left(u_{i+1}^n - u_{i-1}^n\right) - \frac{a^2\Delta t}{2\Delta x_i}\left(u_{i+1}^n - 2u_i^n + u_{i-1}^n\right) + \varepsilon^{(4)}\lambda_{i+\frac{1}{2}}\left(u_{i+2}^n - 4u_{i-1}^n + 6u_i^n - 4u_{i-1}^n + u_{i-2}^n\right)\right]$$

Eq 4.17

The central difference operator representing the fourth order derivative is multiplied with the predetermined smoothing coefficient and also with the eigenvalue of the flux Jacobian which is equal to the advection speed in the linear convection equation.

$$u_i^{n+1} = u_i^n - \left(\frac{\Delta t}{\Delta x_i}\right)\left[\frac{a}{2}\left(u_{i+1}^n - u_{i-1}^n\right) - \frac{a^2\Delta t}{2\Delta x_i}\left(u_{i+1}^n - 2u_i^n + u_{i-1}^n\right) + \varepsilon^{(4)}a\left(u_{i+2}^n - 4u_{i-1}^n + 6u_i^n - 4u_{i-1}^n + u_{i-2}^n\right)\right]$$

Eq 4.18

Using the definition for the CFL number $\sigma = a\,\Delta t/\Delta x$

$$u_i^{n+1} = u_i^n - \sigma\left[\frac{1}{2}\left(u_{i+1}^n - u_{i-1}^n\right) - \frac{\sigma}{2}\left(u_{i+1}^n - 2u_i^n + u_{i-1}^n\right) + \varepsilon^{(4)}\left(u_{i+2}^n - 4u_{i-1}^n + 6u_i^n - 4u_{i-1}^n + u_{i-2}^n\right)\right]$$

Eq 4.19

Conducting the Von Neumann analysis the amplification factors for the harmonics represented in the mesh are calculated as

$$G_j = \frac{V_j^{n+1}}{V_j^n} = 1 - I\sigma\sin(\phi_j) + \sigma^2\left(\cos(\phi_j) - 1\right) - \varepsilon^{(4)}\sigma\left(2\cos(2\phi_j) + 6 - 8\cos(\phi_j)\right)$$
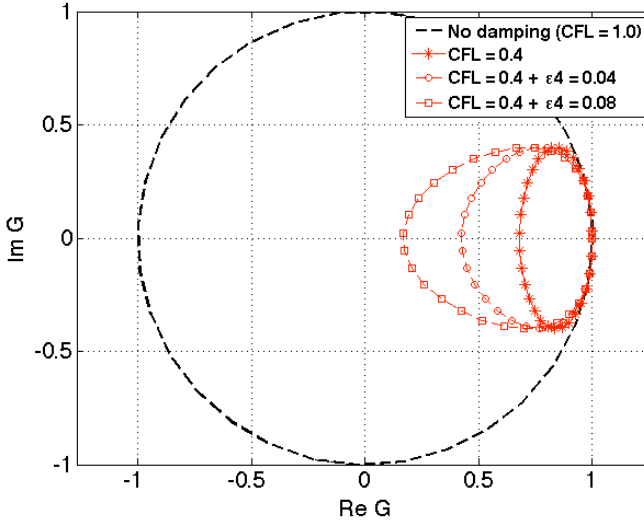
Eq 4.20

Figure 4.8 Representation of the amplification factor G in the complex plane for the Lax-Wendroff scheme at σ = 0.4 and at two different smoothing coefficients

In Figure 4.8 the amplification factor G is plotted in the complex plane. As shown, the addition of the artificial dissipation enhances the damping of the high frequency waves which are not sufficiently damped by the scheme itself. However, it may also smear out some of the flow features especially when the local mesh resolution is low. Scaling of the high order smoothing coefficients is very important for the solution accuracy and solver's stability. On the other hand, high order dissipation has a very minor influence on the well resolved waves.

4.4.   A local CFL Dependent Anisotropic Scaling for the High Order Artificial Dissipation

It has been shown that the damping properties of the Lax-Wendroff scheme have a considerable dependency on the CFL number. As shown in Figure 4.7 there is no or very little amount of artificial dissipation needed at high

CFL numbers. On the other hand, low CFL numbers lead to high frequency oscillations and can severely delay the convergence and deteriorate the stability. The oscillatory behavior of the scheme at low CFL numbers is particularly relevant for the high aspect ratio boundary layer cells used in RANS simulations. In these boundary layer cells the CFL limit is dictated by the grid dimension perpendicular to the wall. Consequently, the local CFL numbers along the wall direction can drop to very low values. The discrepancy in the CFL numbers in the different grid directions reflects also on the damping characteristics of the scheme. And this has to be taken into account in developing the scaling of the artificial dissipation scheme. An isotropic scaling approach would lead either to the contamination of the boundary layers or it would lead to oscillations at the wall. Accordingly, a CFL dependent anisotropic scaling approach is next developed. The stable CFL range of the scheme is divided into three regions and the scaling strategies for each of these regions are separately discussed.

i) Scaling of the Smoothing Coefficient at High CFL Numbers ($0.7 \leq \sigma \leq 1.0$)

This is the CFL range where the inherent numerical diffusion of the Lax-Wendroff scheme is quite considerable for the high frequency waves. The scheme is even more dissipative than the first order upwind scheme for the high frequency waves ($\Phi = \pi$). Therefore, any additional high order artificial dissipation should not be needed at this CFL range. Moreover, introducing artificial smoothing would even reduce the damping characteristics of the scheme for the high frequency waves. In Figure 4.9 the effect of the artificial dissipation on the damping characteristics of the Lax-Wendroff scheme is shown at $\sigma = 0.9$. As shown, applying a positive smoothing coefficient would even grow the amplitudes of the high frequency modes. The scheme's damping characteristics extends beyond the stability region shown by the dashed black curve. Moreover, setting a positive smoothing coefficient would also increase the damping for the low frequency waves which is very undesirable. In Figure 4.9 the amplitudes of the waves with the phase angles smaller than the one indicated with the letter "A" would be more strongly damped. So using a positive smoothing coefficient at this CFL range would reduce the damping of the high frequency waves and would increase the damping of the low frequency

waves. However, the appropriate smoothing should behave exactly in the opposite way. On the other hand, when the negative of the same coefficient is applied the scheme preserves its stability staying well within the stability region and also the amplitude of the low frequency waves are better preserved. As a conclusion, using a positive smoothing coefficient at this CFL range is absolutely inappropriate in terms of its effect on the damping characteristics of the scheme. Using a negative smoothing coefficient would be an option but in this work this option is not considered and therefore the high order smoothing coefficient is set to $\varepsilon^{(4)} = 0$.

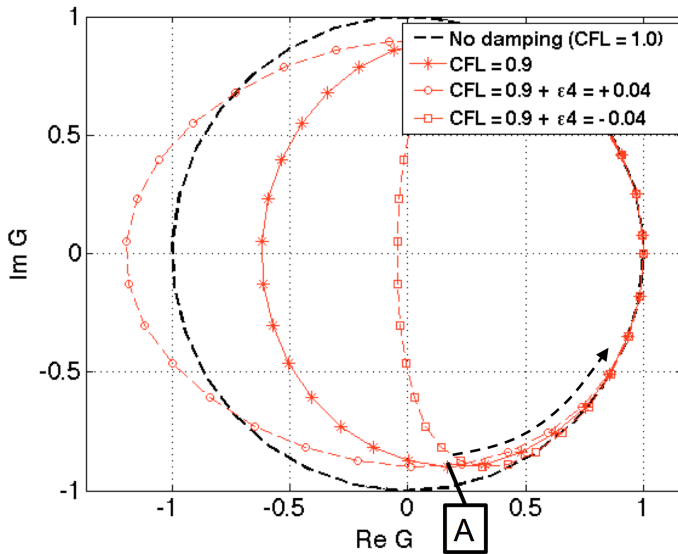Figure 4.9 Influence of the high order smoothing on the damping characteristics of the Lax-Wendroff scheme at σ = 0.9

ii) Scaling of the Smoothing Coefficient at the CFL Range (0.02 < σ < 0.7)

Depending on the flow conditions and the cell aspect ratio the CFL number in one cell direction might be well below 1 even if it is close to 1 in the other cell directions. In this range of the CFL numbers the scheme's

damping for the high frequency waves sharply drop with the decrease in the CFL number and the scheme itself cannot satisfy an oscillation-free solution. So an explicit high order artificial dissipation needs to be introduced. Moreover, the smoothing coefficient has to be scaled up with the decrease in the CFL number. To develop a function that scales the smoothing coefficient as a function of the CFL number first a pivot point is selected. At the pivot point $\sigma = 0.5$ the smoothing coefficient $\varepsilon^{(4)}$ is set to 0.001. Later on the convection of a wave that is resolved with 12 cells across its period is simulated. This case corresponds to the phase angle $\Phi = \pi/6$. Waves represented with at least this amount of points are usually accurately captured by the spatially second order schemes. [80] After carrying out a single iteration with the specified CFL number and the specified smoothing coefficient at the pivot point the amplitude of the wave drops to 99.83 % of its original value. Then the same study is repeated with lower CFL numbers. Parallel to the drop in the CFL numbers the number of the iterations is also increased to reach to the same physical time. Then the smoothing coefficients are varied until the same amplitude value at the pivot point ($\sigma = 0.5$) is reached. Increasing the smoothing coefficients as shown in Table 4.1 a constant damping for the waves at this phase angle can be achieved within this CFL range. As expected, due to the reduction in the damping characteristics of the scheme the smoothing coefficient needs to be increased as the CFL number drops. As shown in Table 4.1, the coefficients increase sharply between the CFL numbers 0.5 and 0.1. For CFL numbers lower than 0.1 the dependency of the smoothing coefficient on the CFL number is much lower. This is because below this CFL number the scheme's diffusive term which scales with the CFL number is almost negligible and the high order artificial dissipation becomes the dominant source of dissipation which does not have a CFL dependency. So the scheme's damping characteristics become uncoupled from the CFL number.

Table 4.1 The scaling of the smoothing coefficient based on the local CFL number to keep the amplitude constant; V : Amplitude and θ : phase angle

σ [-]	$\varepsilon^{(4)}$ [-]	$V^{(0.5/\sigma)}$	Φ [rad]
0.60	0.000	0.99828	π/6
0.50 (pivot)	*0.001*	*0.99828*	*π/6*
0.40	0.006	0.99828	π/6
0.25	0.019	0.99828	π/6
0.10	0.036	0.99827	π/6
0.05	0.042	0.99827	π/6
0.02	0.046	0.99826	π/6

Figure 4.10 Comparison of the amplitude damping for the wave with the phase angle Φ = π/6 using a constant smoothing coefficient versus a CFL dependent variable smoothing coefficient approach

Figure 4.10 compares the amplitude damping for the wave with the phase angle Φ = π/6 using a constant smoothing coefficient $\varepsilon^{(4)}$ = 0.001 and using a CFL dependent varying smoothing coefficient. For high CFL numbers the variable smoothing coefficient approach leads to a lower damping due to having the smoothing coefficient set to zero. For CFL < 0.6 the amplitude damping is kept constant varying the smoothing coefficient according to Table 4.1. On the other hand, using a constant smoothing coefficient leads

to a reduced damping as the CFL is reduced and might lead to oscillations at low CFL numbers. To prevent them a higher overall smoothing coefficient would be needed which would increase the damping of the low frequency waves as well. Therefore, in this variable smoothing coefficient approach the amplitudes of the well resolved waves won't be excessively diffused.
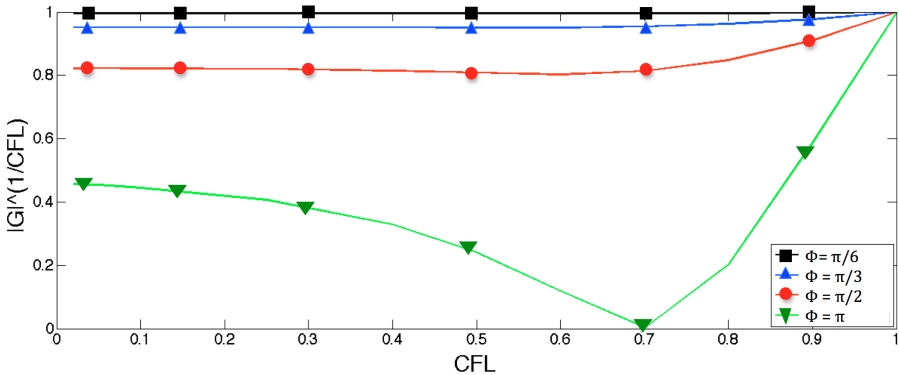

Figure 4.11 Amplitude damping for the waves with different phase angles using the CFL dependent variable smoothing coefficient approach

Figure 4.11 compares the amplitude damping of the waves with different phase angles as a function of the CFL number. As shown, with this CFL dependent scaling approach a constant damping could be achieved for waves with the phase angles up to $\Phi = \pi/2$. However, for the high frequency waves ($\Phi = \pi$) the amplitudes are less and less damped as the CFL number is reduced ($\sigma < 0.5$) even though the smoothing coefficients are increased according to Table 4.1, because this scaling approach has been tuned to deliver a constant dissipation for the phase angle $\theta = \pi/6$. To clarify, this approach still does not guarantee an oscillation-free solution but it gives a method of scaling the smoothing coefficients which accounts for the reduction in the diffusion character of the Lax-Wendroff scheme at low CFL numbers.

iii) Scaling of the Smoothing Coefficient at Very Low CFL Numbers (σ ≤ 0.02)

In RANS simulations cells with very high aspect ratios in the order of O(1000) are very common inside the O-grids. These cells are used because of the major difference in the mean flow physics in each direction. Perpendicular to the wall the grid has to be very fine to capture the very thin boundary layers, but having the same resolution in the streamwise direction is not needed if resolving the mean flow quantities is of interest. Once a CFL condition is set for a cell this has to be based on the smallest dimension of the cell. Accordingly, the CFL number in the streamwise direction has to drop almost to zero where the inherent damping characteristics of the Lax-Wendroff are negligible. At this very low CFL numbers the Lax-Wendroff scheme behaves very oscillatory. In [81] the behavior of the leapfrog scheme is compared with the Lax-Wendroff scheme at σ = 0.01 for the one-dimensional linear convection equation. The two schemes led to the same oscillatory behavior and require additional high order artificial dissipation to damp them. At very low CFL numbers setting the smoothing coefficient according to Table 4.1 does not damp the high frequency oscillations. The scaling shown in Table 4.1 ensures a low level of damping for the well resolved waves. As shown in Figure 4.11 the damping of the high frequency waves are reduced as the CFL number approaches to zero even though the smoothing coefficient is scaled up as shown in Table 4.1. To prevent the even-odd decoupling along the stretched cell dimension the smoothing coefficient needs to be further increased. In this work the smoothing coefficients are scaled anti-proportionally to the local CFL number.

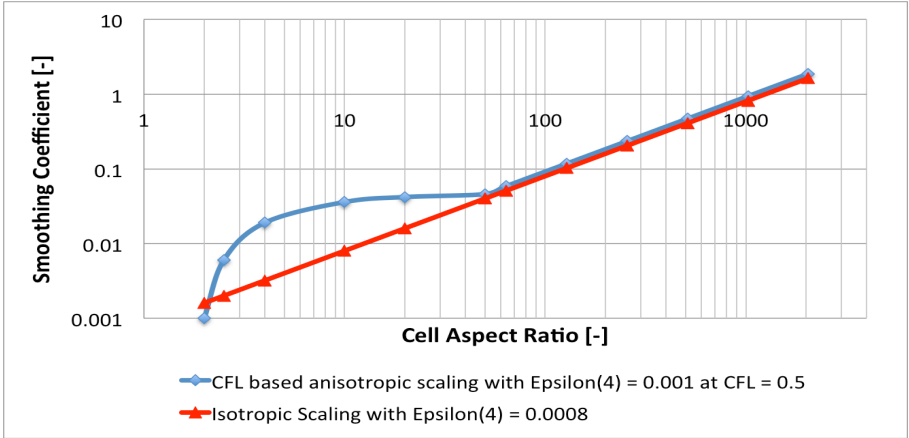$$\varepsilon^{(4)} = \frac{\varepsilon^{(4)}_{@\sigma=0.02} 0.02}{\sigma}$$

Eq 4.21

Figure 4.12 The variation of the smoothing coefficient with respect to the cell aspect ratio (for anisotropic approach this scaling is applied only along the elongated cell direction)
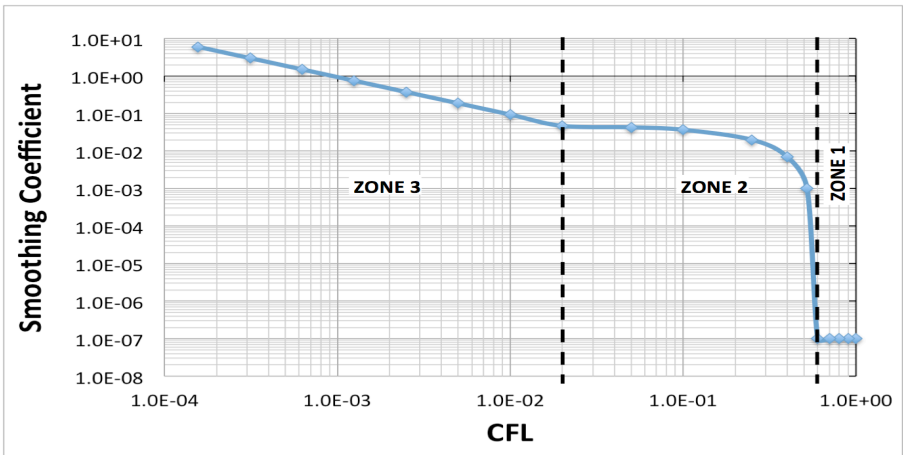

Figure 4.13 The scaling of the high order artificial dissipation coefficient for different CFL values within the stability range of the Lax-Wendroff scheme

This scaling approach is similar to the isotropic scaling approach where the smoothing coefficients are inversely scaled with the time scale Δt as shown in Eq 4.3 or similar to the one proposed by Swanson, Radespiel and Turkel [77]. Increasing the cell aspect ratio the time step limit has to be decreased and the smoothing coefficient increases accordingly. Figure 4.12 shows the variation of the smoothing coefficient with respect to the cell aspect ratio both for the isotropic and the present anisotropic approach. For the anisotropic scaling approach the smoothing coefficients are only scaled up along the elongated cell direction but for the isotropic approach they were applied along the all directions. As shown, a similar scaling is followed for the cells whose aspect ratios are beyond 50. As shown, in general the anisotropic approach applies a higher level of smoothing for the high aspect ratio cells but the higher level of the accuracy that the anisotropic artificial dissipation provides is due to the very low level of artificial dissipation applied along the squeezed cell direction. Nevertheless, the level of the artificial dissipation could be further reduced for the anisotropic approach.

The scaling of the smoothing coefficients within the stability region of the scheme is given in Figure 4.13. In this work the upper CFL limit for the Zone 3 is set to $\sigma = 0.02$. However, this limit is case dependent. For different flow scenarios there might be a need to increase the CFL limit for improved stability at the wall.

4.5.   Effect of the Physical Diffusion

The physical diffusion in viscous simulations has a stabilizing effect on the numerical scheme. Therefore, it may reduce the need for the artificial dissipation. In the RANS modeling approach the physical diffusion is usually very low except at the boundary layers. However, inside the turbulent boundary layers the effect of turbulence is modeled as an additional source of viscosity via the eddy viscosity hypothesis. This modeled viscosity is usually at very high levels compared to the physical viscosity. It adds a stabilizing effect on the simulations and reduces locally the need for the additional artificial dissipation. Shalman et. al.[82] have developed a damping function to reduce the high order smoothing coefficients only inside the turbulent boundary layers and tested its effect on attached and separated boundary layers in external flow applications.

However, unlike in external flows the effect of the turbulence is not confined to boundary layers in internal flow problems. For example, in multi-row turbomachinery the turbulence generated at the very upstream rows convects downstream and affects the aerodynamics of the downstream rows. For the efficiency prediction of the multi-row turbomachinery an accurate modeling of these highly turbulent regions such as the blade wakes and secondary flow features are very crucial. So, considering the effect of the modeled eddy diffusion in the scaling of the smoothing coefficient might be important especially for the internal flow problems.

The indicator for the level of the diffusion (physical + modeled) is the cell Reynolds number. Cell Reynolds number scales linearly with the cell dimensions and the advection velocity and is anti-proportional to the viscosity level. At low cell Reynolds numbers the diffusion becomes dominant and the scheme might be stable without additional artificial dissipation. Wang and Hutter [81] have evaluated the accuracy of the Lax-Wendroff scheme at a very low CFL number ($\sigma < 0.01$) and at different cell Reynolds numbers for the linear convection-diffusion equation. At very low CFL numbers the inherent artificial dissipation of the numerical scheme is almost zero and the only dissipation source is the added viscosity. They have shown that the level of diffusion indicated by the cell Reynolds number (or Peclet number) is very effective on the error up to $Re_{cell} = 40$. Above this level the effect of the diffusion is rather low and numerical dissipation has to be introduced for stability and accuracy. In this work the dependency of the smoothing coefficient on the cell Reynolds number is investigated on the linear convection-diffusion equation.

<u>One-dimensional Linear Convection – Diffusion Equation</u>

$$u_t + au_x = \alpha u_{xx}$$

Eq 4.22

The discretized form of Eq 4.22 is given below.

$$u_i^{n+1} = u_i^n - \frac{a\Delta t}{\Delta x}\left[\frac{1}{2}\left(u_{i+1}^n - u_{i-1}^n\right) - \left(\frac{a\Delta t}{2\Delta x} + \frac{\alpha}{a\Delta x}\right)\left(u_{i+1}^n - 2u_i^n + u_{i-1}^n\right)\right]$$

Eq 4.23

By using the following definition of the cell Reynolds number one can end up with Eq 4.24.

$$\mathrm{Re} = a\Delta x/\alpha$$

$$u^{n+1} = u^n - \sigma\left[\frac{1}{2}\left(u_{i+1}^n - u_{i-1}^n\right) - \left(\frac{\sigma + 2/\mathrm{Re}}{2}\right)\left(u_{i+1}^n - 2u_i^n + u_{i-1}^n\right)\right]$$

Eq 4.24

As shown in Eq 4.24, the cell Reynolds number acts as an additional coefficient for the diffusive term in the numerical scheme. So the overall diffusion is the sum of the numerical diffusion proportional to the local CFL number and the physical diffusion combined with the modeled eddy diffusion anti-proportional to the local cell Reynolds number. Since a local CFL number based scaling of the high order artificial dissipation coefficient has already been developed the effect of the cell Reynolds number can be incorporated into this approach as well.

Table 4.2 Dependency of the smoothing coefficient on the cell Reynolds number at $\sigma = 0.02$

Re_{Cell}	$\sigma + 2/\mathrm{Re}_{Cell}$	$\varepsilon^{(4)}$
100.	0.02 + 0.020	0.043
50.	0.02 + 0.040	0.041
25.	0.02 + 0.080	0.036
10.	0.02 + 0.200	0.021
2.	**0.02 + 1.000**	**0.000**

Table 4.2 shows the scaling of the smoothing coefficient based on the local cell Reynolds number at a local CFL number of 0.02. For cell Reynolds numbers below 2 the diffusion (physical + modeled) is so high such that even the Lax-Wendroff's inherent diffusive term is not needed. At this low cell Reynolds numbers the explicit central scheme with first order time integration would also be stable. Figure 4.14 shows the scaling of the smoothing coefficient based on the cell Reynolds number for two different CFL values. As shown, for cell Reynolds numbers below 50 there is a considerable dependency of the high order smoothing coefficient on the cell Reynolds number. And as the CFL number is decreased this dependency is also enhanced.
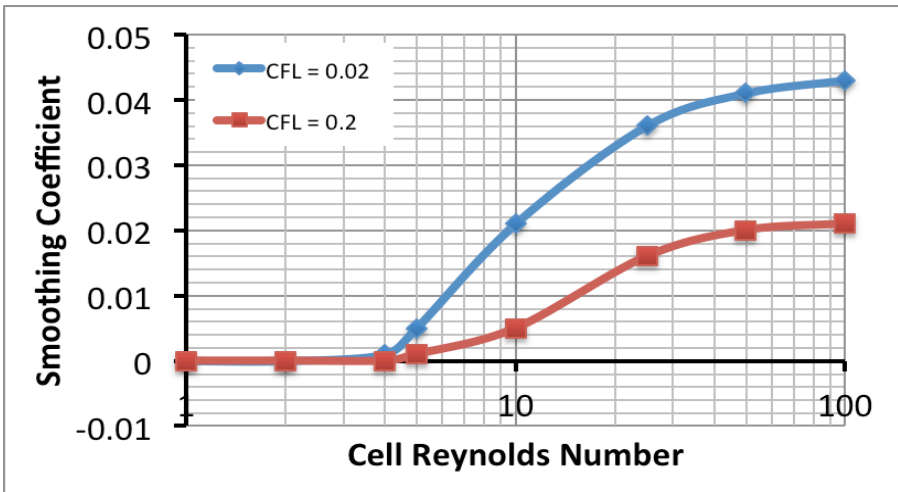

Figure 4.14 Dependency of the smoothing coefficient on the cell Reynolds number

4.6. Effect of the Smoothing on the Solver's Accuracy

The new smoothing algorithm developed on the basis of the Von Neumann stability analysis is implemented to the in-house compressible RANS solver "MULTI3". The solver uses the Ni's Lax-Wendroff scheme to solve the

three-dimensional, time dependent Navier-Stokes equations. The turbulence is modeled via Wilcox's k-ω [29] turbulence model. The solver is GPU accelerated. The new smoothing algorithm is tested on laminar and turbulent flat plate scenarios and on unsteady, multi-row high pressure turbine simulations. The turbulent flat plate scenarios and the turbine simulations are conducted with the isotropic and anisotropic artificial dissipation approaches. The coefficients used are shown in Table 4.3. The smoothing coefficients used for the isotropic smoothing approach are at the limit of the stability for the turbine simulations. In these test cases shocks are not considered. Accordingly, the level of the second order dissipation is negligible.

Table 4.3 Coefficients for the artificial dissipation schemes used in the numerical test

Smoothing Types	$\varepsilon^{(2)}$	$\varepsilon^{(4)}$	Scaling
Isotropic Smoothing	0.012	0.0008	Mach Number
Anisotropic Smoothing	0.0625	Local CFL based (0.001@ σ = 0.5)	Cell Reynolds Number

4.6.1. Laminar Flat Plate

In this study the flow over a flat plate is simulated with no-slip wall boundary conditions imposed at the wall and the parameters of the developing boundary layer are compared with the well-known Blasius solution. A three-dimensional rectangular flow domain is used with the dimensions being 0.04 m, 0.04 m and 0.004 m in length, height and width respectively. Three Cartesian meshes with varying number of cells inside the boundary layer are generated. The sizes of the meshes are given in Table 4.4 The coarsest mesh has only 4 cells in the boundary layer at the outlet of the domain and the others have 8 and 16 cells. Inside the boundary layer a uniform mesh spacing is used perpendicular to the wall and outside of the boundary layer the mesh spacing is increased with a constant

expansion ratio. The mesh is only refined in the wall perpendicular direction not in the longitudinal direction of the flow domain. Normally, in the grid refinement studies the mesh has to be refined in all directions by the same ratio. In that case the cells aspect ratios are also conserved. However, this can only be realized on very simple and mostly 2D scenarios. The core of the study is to evaluate the performance of the smoothing algorithm for more elaborate scenarios used in the real practice where grid refinement studies ever done could be performed only in one direction.

Table 4.4 The number of the grid points used along the axis of the flow domain for the meshes used in the grid sensitivity study

	No of cells inside BL	No of grid points in x-dir	No of grid points in y-dir	No of grid points in z-dir
Mesh 1	4	128	3	42
Mesh 2	8	128	3	48
Mesh 3	16	128	3	64

At the inlet of the domain total conditions and the flow angles are defined and at the outlet the static pressure is set to have an inlet Mach number of 0.15. At the upper wall of the domain a slip wall boundary condition is set and at the sides periodicity is imposed. At the domain outlet the thickness of the boundary layer reaches to about 1% of the height of the flow domain. The calculated boundary layer profiles at $Re_x = 100,000$ are compared with the Blasius solution in Figure 4.15-a.Visually a grid independent solution is reached even with 8 cells inside the boundary layer. The extreme coarse mesh with four cells inside the boundary layer shows some deviations from the reference solution. However, even at this mesh resolution the shape of the boundary layer is quite reasonably predicted. The errors in the displacement thickness and the momentum thickness are given in Table 4.5.

Next, the calculated wall shears are compared with the Blasius solution. In Figure 4.16 the variations in the wall shear stress levels are shown for the same meshes. As shown, the mesh resolutions for the mesh 1 and 2 are not high enough to resolve the developing boundary layer at the domain entrance and leads to heavily underestimated wall shear stress levels. As the boundary layer develops even the coarse meshes start to be capable of

resolving the boundary layer and the wall shear stress predictions become more accurate downstream of the inlet. The errors in the wall shear stress levels at $Re_x = 100{,}000$ are given in Table 4.5.

Table 4.5 The error in the wall shear stress, displacement thickness and momentum thickness of the forming boundary layer resolved with different number of cells calculated with the cell Reynolds scaled, anisotropic smoothing approach.

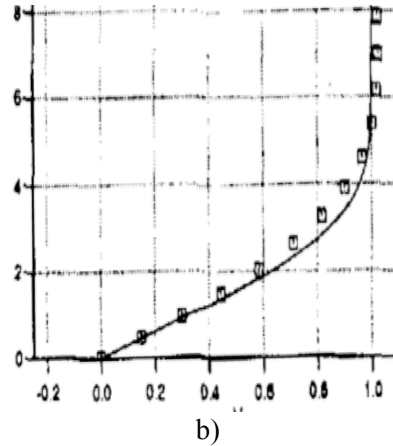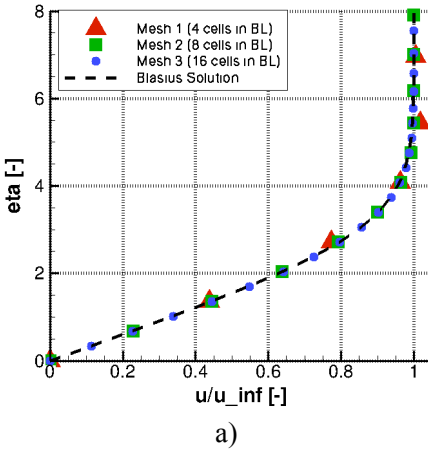| ERROR [%] @ $Re_x = 100{,}000$	No of cells in BL	C_f	Displacement thickness	Momentum thickness
Mesh 1	4	2.44	4.12	9.37
Mesh 2	8	1.87	0.19	1.42
Mesh 3	16	1.87	0.32	0.07

Figure 4.15 The non-dimensional laminar velocity profiles a) present scalar anisotropic artificial dissipation scheme at $Re_x = 100{,}000$; Mach = 0.2 b) scalar anisotropic artificial dissipation scheme at $Re = 2.96 \times 10^5$; Mach = 0.8 [84]
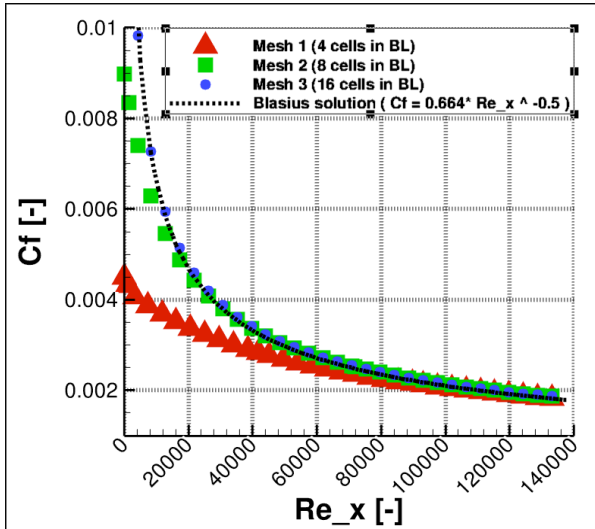
Figure 4.16 The wall shear stress along the flat plate calculated with the indicated mesh resolutions and using the cell Reynolds scaled anisotropic smoothing approach (the scatter points show the position of the grid points – every four is shown)

A two-dimensional grid sensitivity study has been conducted by Tatsumi, Martinelli and Jameson [83] on a comparable flow scenario where the Reynolds number and the Mach number are the same with the ones in this study. They have compared the errors in the different aspects of the boundary layer for different numerical schemes. Compared to their central scheme the levels of the errors resulted for the same grid resolutions are considerably lower with the present scheme. Another similar laminar flat plate study has been conducted by Mackenzie [84] where Mach = 0.8 and $Re = 2.96 \times 10^5$. In the computation the Ni-Lax Wendroff scheme is utilized with different kinds of scalar dissipation schemes and even also with the more costly matrix dissipation scheme. Among the scalar dissipation schemes the isotropic and the anisotropic versions accompanied with the local Mach number scaling for reducing the excessive dissipation inside the boundary layers have been considered. Even though no quantitative error analysis has been conducted the velocity profile deviates

considerably from the Blasius solution even using 10 cells within the boundary layer. The non-dimensional velocity profile is shown Figure 4.15-b. The accuracy level reached with the present dissipation scheme in resolving the boundary layer profile with 4 cells is higher than the one reached in [84] with 10 cells. The present scheme also shows a much higher accuracy resolving the laminar boundary layers compared to the scalar, anisotropic dissipation scheme by Swanson, Radespiel and Turkel [77] where even with 16 cells a grid independent solution was not achieved.

4.6.2. Turbulent Flat Plate

Similar to the laminar flat plate study discussed previously the development of the turbulent boundary layer on a flat plate is investigated. In case of turbulent boundary layers cells with aspect ratios in the order of 1000's are quite common. Under these circumstances the quality of the smoothing algorithm is very crucial especially for the wall shear stress prediction. A three-dimensional rectangular flow domain is used with the dimensions being 2 m, 1 m and 0.05 m in length, height and width respectively. The mesh is clustered both in the longitudinal direction and also in the wall perpendicular direction. 30 cells have been placed within the boundary layer. In this study the Wilcox k-ω turbulence model is utilized for the closure of the RANS equations. At the domain inlet a uniform velocity profile with a Mach = 0.2 is imposed.

The evaluation of the wall shear stress along the flat plate is given in Figure 4.17 alongside with the empirical correlations for the wall shear stress depending on the character of the boundary layer. As shown in Figure 4.17 in both portions of the boundary layer (laminar and turbulent) the shear stress variation matches with the correlations without showing any artificial fluctuations. Moreover, the natural transition of the boundary layer from laminar to turbulent is also captured.
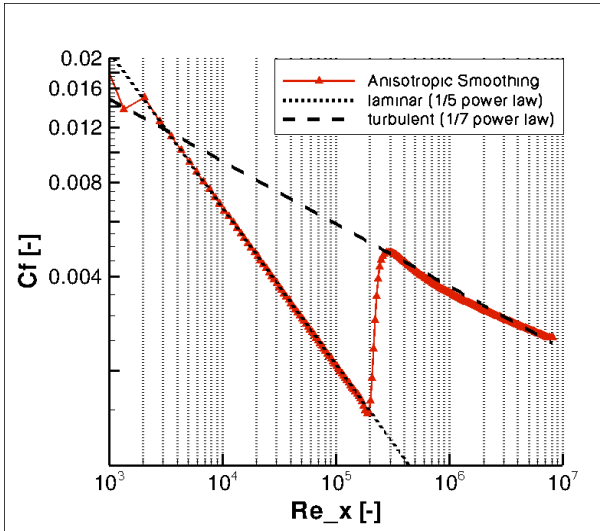
Figure 4.17 The wall shear along the flat plate calculated with the cell Reynolds scaled, anisotropic smoothing approach (The scatter points indicate the grid points along the flat plate)

On the other hand, simulating the same flow scenario with an isotropic smoothing leads to serious oscillations at the wall shear stress along the wall. Figure 4.18 shows the wall shear stress distribution obtained with the isotropic smoothing algorithm. The oscillations at the laminar portion of the boundary layer might be due to the effect of the stagnation point at the leading edge of the flat plate. The disturbance generated there leads to oscillations which decay slowly downstream of the leading edge. There are also oscillations downstream of the transition point and their intensities grow significantly towards the outlet of the flow domain, where the cell dimensions grow in longitudinal direction. In Figure 4.12 it has been shown that both artificial dissipation schemes have the same level of smoothing coefficient in high aspect ratio cells. The issue that the isotropic artificial dissipation leads to oscillations and the anisotropic one not is due to the incorporated Mach number scaling approach into the isotropic artificial dissipation scheme to reduce the contamination of the boundary layers. Even though this approach does prevent the excessive dissipation of the

boundary layers in wall perpendicular direction, the same level of smoothing coefficient is not enough to damp the oscillations along the wall. Also the non-dimensional velocity profiles calculated by the isotropic and anisotropic smoothing algorithms are compared in Figure 4.19 against the empirical data representing the so-called wall of the law. The scatter points on the curves indicate the position of the mesh points. As shown, there is a complete match between the two profiles at the inner and buffer layer of the turbulent boundary layer. However, there is a slight difference between these two results at the end of the outer layer where the free stream velocity is recovered. The isotropic smoothing leads to over- and undershoots in the non-dimensional velocity level whereas this behavior is damped with the anisotropic smoothing. There are no artificial overshoots are observed at the edge of the boundary layer.
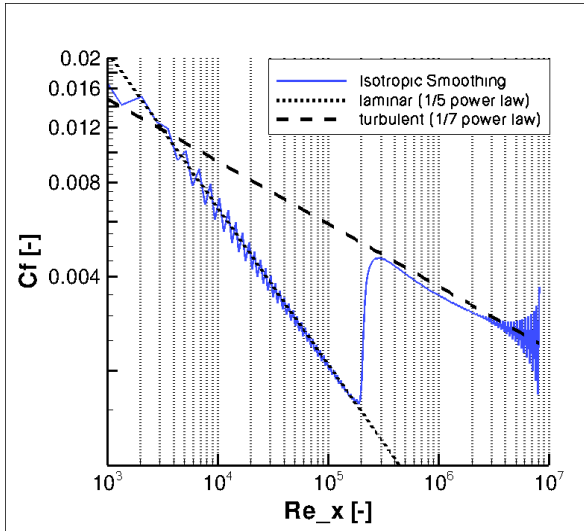
Figure 4.18 The wall shear along the flat plate calculated with the Mach number scaled isotropic smoothing approach
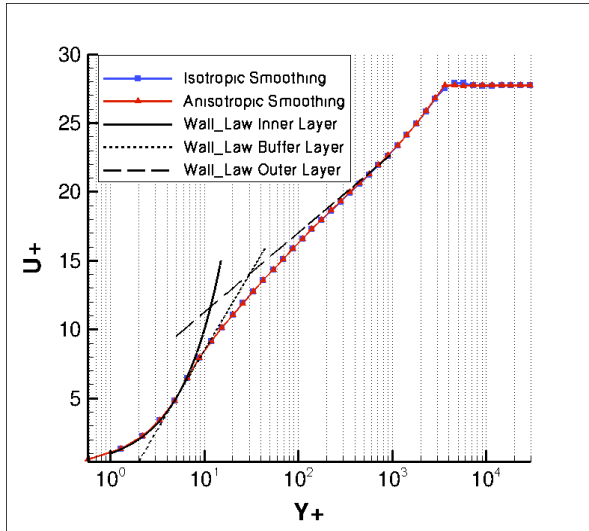
Figure 4.19 The wall law at 80% longitudinal position of the flat plate calculated with the cell Reynolds scaled, anisotropic smoothing and Mach number scaled isotropic smoothing approaches

4.6.3. Turbulent Flat Plate (with wall functions)

The present artificial dissipation scheme has also been tested on turbulent boundary layers modeled using the wall function approach. In the wall function approach the mesh does not resolve the different portions of the boundary layer but models it using the law of the wall. In this study the first node above the wall is positioned at $y^+ = 200$. For the closure of the RANS equations the Wilcox [29] k-ω turbulence model has been utilized.
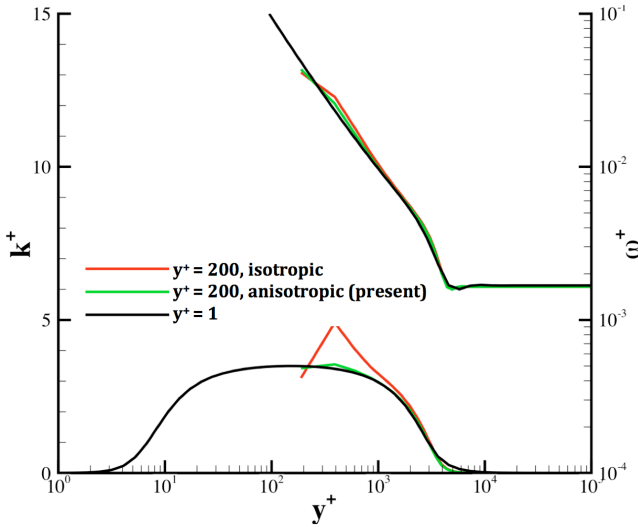
Figure 4.20 Calculated non-dimensional k^+ & ω^+ profiles within the turbulent boundary layer using wall function approach

In Figure 4.20 the profiles of the non-dimensional turbulent kinetic energy "k^+" and the non-dimensional turbulent dissipation "ω^+" are shown. The profiles obtained using a low Reynolds number mesh where the first node above the wall has a y^+ value of 1 are taken as the reference data as plotted in black in Figure 4.20. As shown, the present artificial dissipation scheme predicts the "k^+" profile closer to the reference data than the isotropic dissipation scheme does. The low mesh densities used in wall function approach has enhanced the effect of the artificial numerical dissipation scheme which would not be as pronounced if high mesh densities were used as in the low Reynolds approach. A similar deviation from the resolved "k^+" profile is also observed in [85] where it was clearly shown that it is due to the numerical error related to the low grid resolution used. The present numerical scheme reduces the numerical dissipation errors and increases the accuracy substantially especially in coarse grids.

4.6.4. Multi-row, Axial Turbine Aerodynamics

The effect of the developed smoothing algorithm is tested on the multi-row, unsteady turbine aerodynamics. For this study the in-house developed "D-case" turbine geometry has been used. The turbine consists of one-and-a-half stages and is representative of cooled HP turbines. The specifications of the turbine geometry are given in 1.

A low Reynolds number, multi-block, structured mesh has been generated with the in-house mesh generator "Meshbound". As shown in Figure 4.21 the mesh included all the three blade rows covering 20° section of the whole annulus. Parallel to the ratios of the blades in subsequent rows, the mesh included two stator passages in the first row, three rotor passages downstream and two stators in the last row. The dimensions of the mesh for each blade row are given in Table 4.6. The overall mesh consists of about 4.5 million nodes

Table 4.6 The number of the grid points used in each direction (The meshes have a multi-block structure)

Flow Domains	No. of grid points in spanwise dir.	No. of grid points in streamwise dir.	No. of grid points in circumf. dir.	Total mesh size (millions)
Stator 1	86	95	67	0.7
Rotor	66 + 20 (blade + clearance)	117	45	0.65
Stator 2	86	96	58	0.7

The inlet boundary conditions are taken from the experimental measurements conducted approximately one blade chord upstream of the stator 1, where the circumferential variations due to the effect of the stator potential field are negligible. The radially varying incoming flow properties are defined by the total pressure and total temperature distributions alongside of the flow angle distributions. The turbulence intensity is also derived from the measurements showing a low intensity of turbulence of 1 % at the midspan. Towards the endwalls the turbulence intensity rises to

about 10%. The details of the turbulence measurements are given by Behr [58].

However, the flow field within the boundary layers cannot be completely resolved. The remaining parts of the boundary layer profiles are derived from additional numerical study where the upstream inlet duct is prolonged until the boundary layer thickness reaches to the level measured upstream of the stator 1 and this numerical data is blended to the experimental data outside of the endwall boundary layers. In addition to these a uniform turbulent length scale of 0.0001 m is imposed.

Additionally, no slip, adiabatic wall boundary conditions are applied at the solid walls. At the turbine outlet the average static pressure level at the hub endwall is specified to keep the total to static pressure ratio at 1.65. This value is kept constantly at that level during the measurement in the test rig. Assigned to these boundary conditions unsteady simulations are conducted utilizing the Jameson's dual time stepping approach. The period of the passing of the three rotor blades is divided into 100 time steps. 100 sub-iterations have been conducted at each physical time step at a CFL number of 0.85. The periodicity of the solution is checked via the monitoring points positioned at the periodic faces between the blade rows. It took about 800 time steps to reach a periodic solution which corresponds to 160° rotation of the rotor disk.

For the closure of the RANS equations Wilcox k-ω [29] turbulence model equations are used. For the data transfer between the rows the sliding interface approach has been utilized. In this approach all the seven variables at the interface are interpolated from the data at the upstream and downstream nodes. Thanks to the GPU acceleration the simulation can be completed within 24 hours with the present anisotropic dissipation scheme.
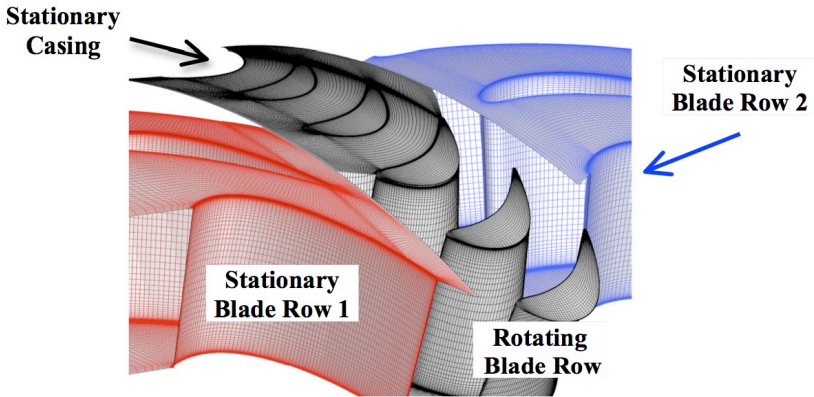
Figure 4.21 The wall mesh of the one-and-half stage axial turbine

Convergence Monitoring:

For deciding on the convergence of the unsteady runs the periodicity of the static pressure at the monitoring points is monitored. These monitoring points are positioned at the periodic faces at the two axial interfaces. (between the stator1 and the rotor and between the rotor and the stator 2) Figure 4.22 shows the time history of the static pressure for the last two periods. As shown, the level of the correlation for the monitoring points downstream of the first stator is higher than the one observed downstream of the rotor.
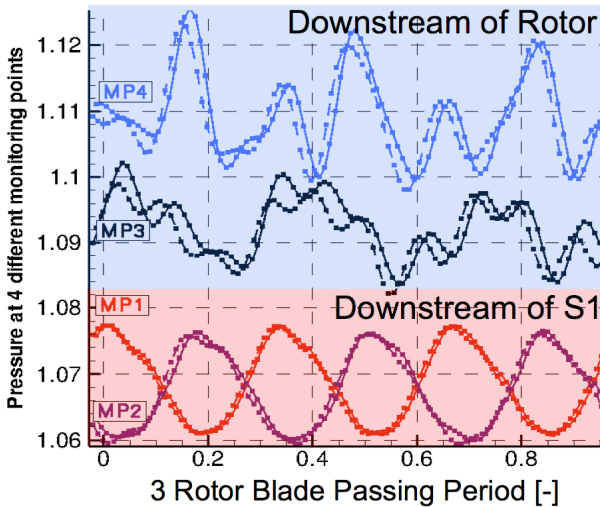
Figure 4.22 The time history of the static pressure at the monitoring points downstream of the stator 1 and the rotor

Figure 4.23 shows the delta RMS levels between the two subsequent periods. As shown, with increasing number of periods the delta RMS levels are dropping. In addition to monitoring of the pressure signal, the time averaged relative total pressure distribution downstream of the rotor blade is also checked for subsequent periods since it is actually the quantity of interest to measure the losses and calculate the efficiency of the turbine.

RESULTS

The simulations have been conducted using the existing Mach number scaled isotropic smoothing algorithm and the two versions of the anisotropic smoothing algorithm. In one of the anisotropic smoothing approaches the scaling of the high order smoothing coefficient $\varepsilon^{(4)}$ purely depends on the local CFL number and in the other one the local cell Reynolds number is also taken into account in the scaling of the smoothing coefficient. For the isotropic artificial dissipation the value of the high order smoothing coefficient $\varepsilon^{(4)}$ is kept at 0.0008 as it was in the turbulent flat

plate study. At lower smoothing coefficients the solver was not stable for this specific problem and mesh density. Moreover, its level is lower than the one used in [76] by a factor of three.
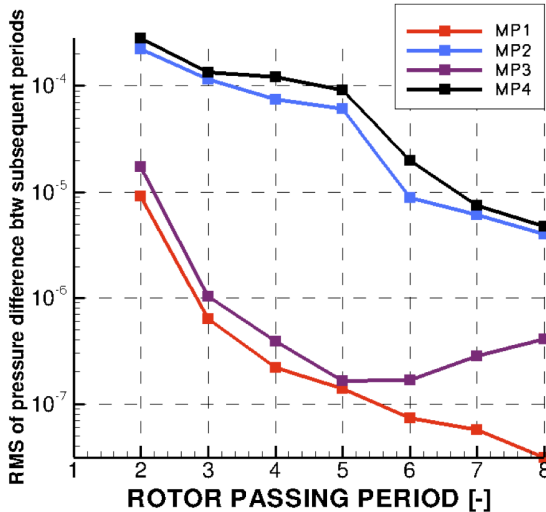
Figure 4.23 The RMS of the difference between the respective pressure levels at the two subsequent periods

i) Downstream of the Stator 1 (B-plane) :

In Figure 4.24 the calculated, time averaged absolute total pressure distributions downstream of the first stator are shown alongside the experimental measurement at the same position. Low zones of the relative total pressure indicate loss. All the numerical results are not far from each other. In all of the results the levels of the total pressure inside the passage vortices are slightly underestimated. Also compared to the measurements the spanwise position of the hub passage vortex is overestimated in all of the numerical results. However, with the cell Reynolds scaled anisotropic smoothing approach the passage vortices are radially less diffused and their radial extents are closer to the measurements. Overall, the new artificial

dissipation scheme does not show a major advantage in the loss predictions downstream of the stator.
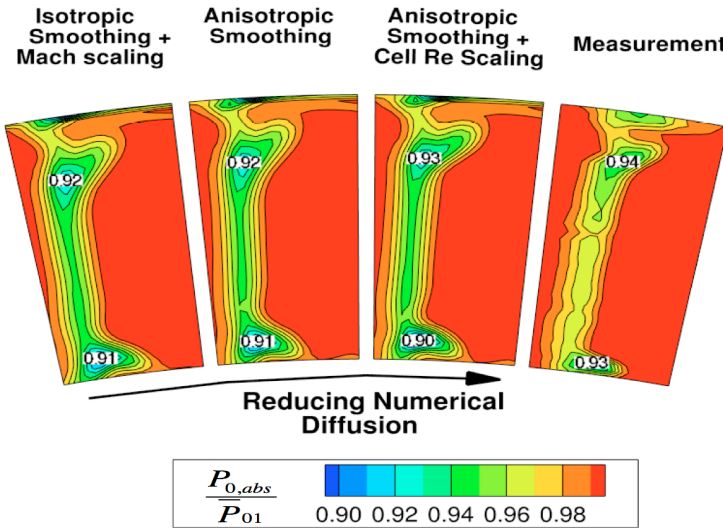
Figure 4.24 The time averaged absolute total pressure distributions downstream of the stator 1 alongside the measurement

ii) Downstream of the rotor (C-plane) :

The calculated time averaged relative total pressure distributions downstream of the rotating blade rows are shown in Figure 4.25. Low zones of the relative total pressure indicate loss. In all the simulation results and also in the experimental measurements three distinct loss structures can be seen which are the tip leakage vortex, passage vortices and the wake. The tip leakage vortex develops as a strong jet like structure forming between the tip of the rotor blade and the stationary casing and rolls into a vortex after it leaves the tip clearance gap. The two passage vortices are formed due to the slipping of the incoming endwall boundary layers by the effect of the transverse pressure gradient across the two sides of the rotor blade. These passage vortices migrate towards the midspan and mix with the wake of the airfoil. Comparing the simulation results with the

measurements one can see that there is a substantial increase in the level of the prediction accuracy of the tip leakage vortex as the artificial dissipation level is reduced. This region of the domain includes high aspect ratio cells and also a considerable high level of eddy viscosity reaching up to 700 times of the physical viscosity levels. In Figure 4.25 the effects of only CFL scaled anisotropic scaling approach and also the additional cell Reynolds number scaling approach are separately shown. There is a gradual increase in the accuracy of the results as the level of the artificial dissipation is reduced. The effect of the present artificial dissipation approach is relatively low in the prediction of the other loss structures where the aspect ratio of the cells are not as high as in the tip leakage region. However, still some minor improvement is observed in the accuracy of the prediction of the passage vortices relative to the measurements. For example, as the numerical dissipation is reduced the two passage vortices are predicted well separated from each other as it is in the measurements.
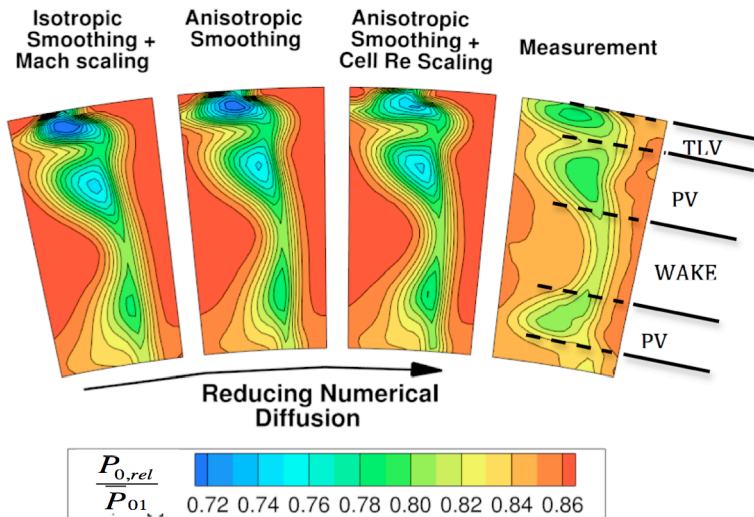
Figure 4.25 The non-dimensional time averaged relative total pressure distributions downstream of the rotor row alongside the measurement
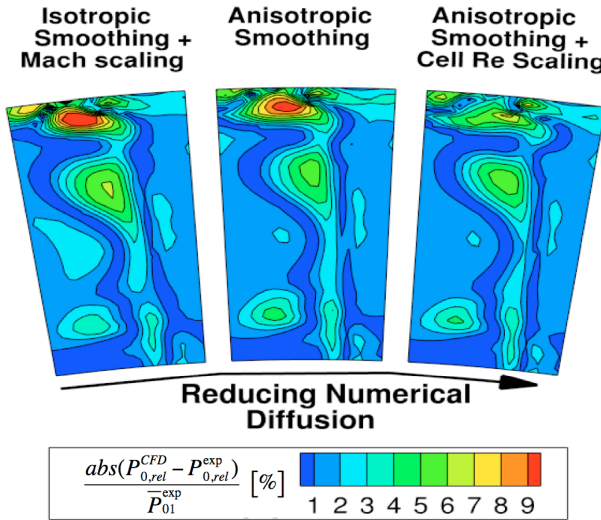
Figure 4.26 The error in the time averaged relative total pressure distributions downstream of the rotor row relative to the measurement

Figure 4.26 shows the error in the simulation results relative to the measurements. As shown, the peak error is observed inside the tip leakage vortex core reaching values up to 11 % with the isotropic artificial dissipation approach and it reduces down to about 6 % with the anisotropic artificial dissipation approach scaled both with the local CFL and the cell Reynolds number. The reduction in the relative error is much less at the other loss structures.

Interaction of the Artificial Dissipation with the k-ω Turbulence Model:

Figure 4.27 shows the time averaged relative Mach number levels downstream of the rotor blade rows for the three different simulation results and for the measurements. The minimum Mach number levels in the core of the tip leakage vortices are additionally indicated. In general, all the three simulations under-predict the Mach number levels at the near-wake

region. However, the reduction in the level of the artificial dissipation led to a faster recovery of the low momentum regions especially inside the tip leakage vortex. But also in the wake of the blade (shown by black arrows) a faster recovery is observed reducing the level of the artificial dissipation. This behavior has to do with the increase in the level of the local diffusion which is a combined effect of the physical diffusion, modeled eddy diffusion and the numerical dissipation. However, since the numerical dissipation is reduced the additional rise in the diffusion can only be due to the rise in the modeled eddy viscosity since the level of the physical viscosity is negligible. Moreover, the very similar temperature fields between these simulations should predict the same level of physical viscosity via the Sutherland law.
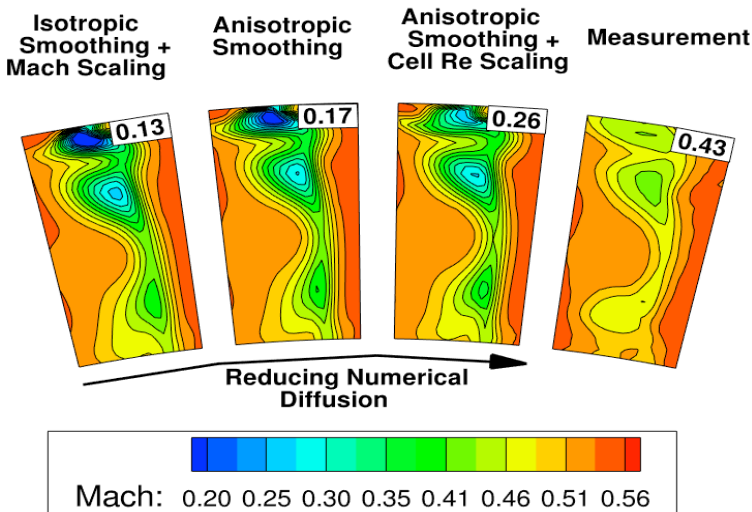
Figure 4.27 The time averaged relative Mach number predictions downstream of the rotor row alongside the measurement (the Mach number levels at the cores of the tip leakage vortices are indicated)

Figure 4.28 shows the time averaged eddy viscosity levels at the same axial position downstream of the rotating blade rows for the two different versions of the anisotropic artificial dissipation approaches. As shown, the

cell Reynolds scaled anisotropic artificial dissipation approach leads to a higher level of modeled eddy viscosity compared to the only CFL scaled anisotropic artificial dissipation approach especially in the tip leakage vortex region. The reduction in the level of the artificial dissipation leads to a more accurate modeling of the turbulence field which as a result reflects into the accuracy of the results considerably. This study shows the strong interaction between the artificial dissipation scheme used in the solvers and the turbulence model itself. Even though the eddy viscosity level is increased with reducing the level of the artificial dissipation the mixing inside the secondary flow regions and also in the wake is still underestimated. In Figure 2.13 the level of the calculated turbulence intensity was compared with the one in the measurements.

Figure 4.28 The time averaged eddy viscosity ratios downstream of the rotor row predicted with the anisotropic artificial dissipation approaches where the cell Reynolds scaling is additionally incorporated in one of them

Effect of the Artificial Dissipation on the Tip Leakage Flow Prediction :

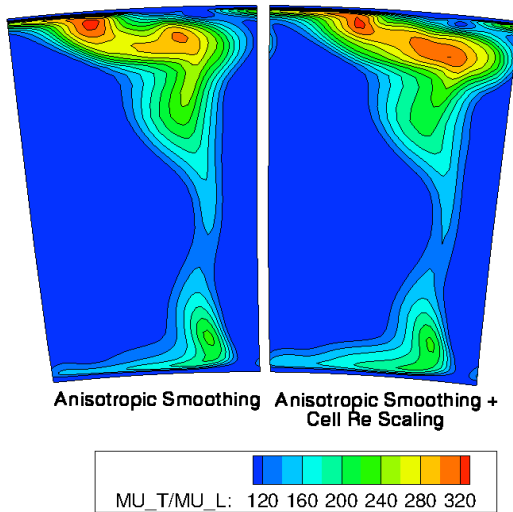As it was shown in Figure 4.27 there was a considerable dependence of the Mach number predictions inside the tip leakage vortex downstream of the rotor blade on the artificial dissipation scheme used. However, it is difficult to draw conclusions on the predicted tip leakage mass flow rates for the different artificial dissipation schemes used. Figure 4.29 shows the absolute circumferential Mach number distributions predicted with the three different artificial dissipation approaches along the axial chord of the rotor blade at 50 % of the tip clearance height at the suction side of the blade. As shown, the Mach number level is more or less constant down to 75% of the axial chord and from this point on it shows a steep drop because the loading on the blade is decreasing which drives the tip leakage mass flow. There is a slight difference in the predicted Mach number levels between the isotropic and anisotropic artificial dissipation approaches especially around the 50% of the axial chord. At this region the rotor blade is relatively thick and the viscous effects are more considerable compared to the thinner regions of the blade such as the leading and the trailing edges. In Figure 4.30 the circumferential velocity profile at the 50 % axial chord at the suction side edge of the rotor blade tip across the tip clearance is shown. As shown the velocity profile is mostly dominated by the casing boundary layer. The boundary layer at the rotor blade tip covers only a very small portion of the tip clearance height. The anisotropic artificial dissipation scheme predicts a slightly higher velocity level compared to the isotropic dissipation scheme.
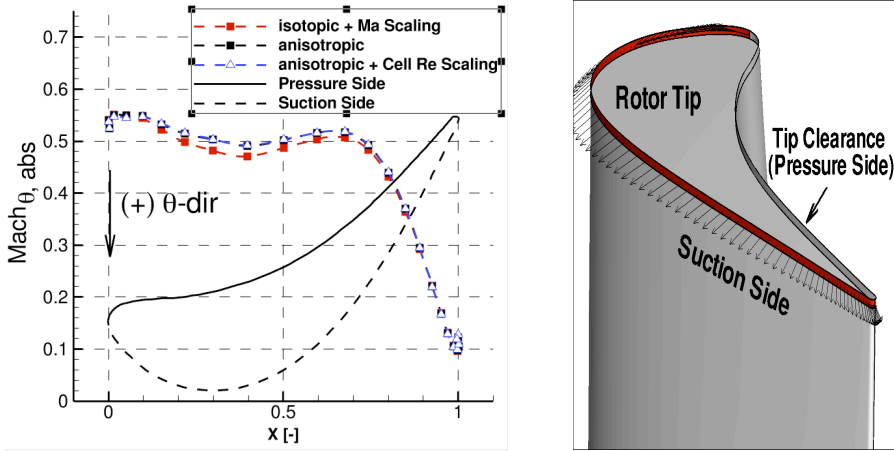
Figure 4.29 The absolute circumferential Mach number distribution along the axial chord of the rotor at 50 % of the tip clearance height at the suction side of the blade
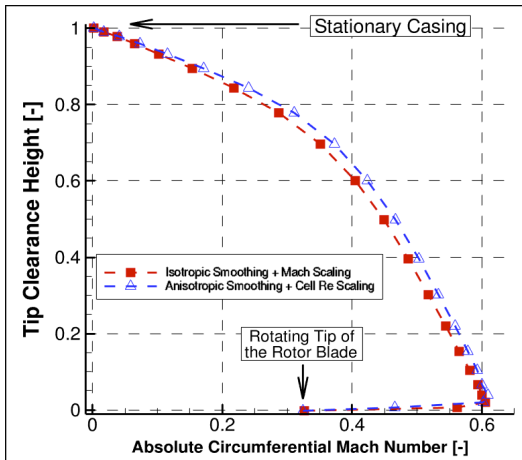

Figure 4.30 The absolute circumferential Mach number distribution across the tip clearance height at 50% of the axial chord at the suction side of the rotor blade

Table 4.7 compares the tip leakage mass flow levels predicted with the three different artificial dissipation approaches. As shown in Table 4.7 and also in Figure 4.29 there is no difference between the predictions of the two anisotropic dissipation approaches, even though there was a considerable difference in the Mach number levels predicted by these two schemes downstream of the rotor blade in the center of the tip leakage vortex core. The difference in the Mach number levels downstream of the rotor blade inside the tip leakage vortex between these two anisotropic artificial dissipation schemes (shown in Figure 4.27) is only due to the difference in the prediction of the mixing behavior of the tip clearance jet after it has emerged from the tip clearance of the rotor blade. The reason that the two anisotropic artificial dissipation schemes lead to the same result inside the tip clearance is thought to be due to the fact that the numerical dissipation in wall perpendicular direction inside the tip clearance is completely cut by the local CFL scaling only because the local CFL number along this direction is very close to 1. So adding a cell Reynolds scaling does not reduce the numerical dissipation further since it has been already completely cut by the CFL scaling only unless the solver has been run at CFL numbers lower than 0.5.

Table 4.7 The tip leakage mass flow rates predicted with different artificial dissipation schemes

Smoothing Type	Tip Leakage Mass Flow / Total Mass Flow [%]
Isotropic + Mach Scaling	2.56
Anisotropic	2.62
Anisotropic + Cell Re Scaling	2.62

Effect on the Stage Efficiency :

Finally, the effect of the artificial dissipation scheme on the stage efficiency prediction is evaluated. The stage efficiencies are calculated using the time

averaged 2D-plane data upstream and downstream of the stage. Table 4.8 shows the calculated efficiency values with the experimental value at the last row. As shown, all the efficiency predictions are lower than the experimental value. However, with the reduction in the artificial dissipation the estimations come considerably closer to the measured value.

Table 4.8 The stage efficiencies calculated with the different artificial dissipation approaches alongside the measured value

Smoothing Type	Total – to – total Efficiency [%]
Isotropic + Mach Number Scaling	90.3
Anisotropic	90.4
Anisotropic + Cell Reynolds Scaling	90.6
Measurement [86]	**91.0**

4.6.5. Unsteady Turbine Aerodynamics with Temperature Non-Uniformity

The developed anisotropic scaling approach for the artificial dissipation scheme is next tested on the multi-row, unsteady turbine aerodynamics including the migration of the temperature non-uniformities termed as hot streaks. For this study the "M1-case" turbine geometry has been used which is adapted from the "D-case" geometry by adding endwall profiling to the first stator. The specifications of the turbine geometry are given in 1. A low Reynolds number, multi-block, structured mesh has been generated with the in-house mesh generator "Meshbound". The mesh included only the first two blade rows covering 20° section of the whole annulus. Parallel to the ratios of the blades in subsequent rows, the mesh included two stator passages in the first row, three rotor passages downstream. The parameters

of the mesh are very similar to the one shown in Table 4.6. The overall mesh consists of about 3.2 million nodes.
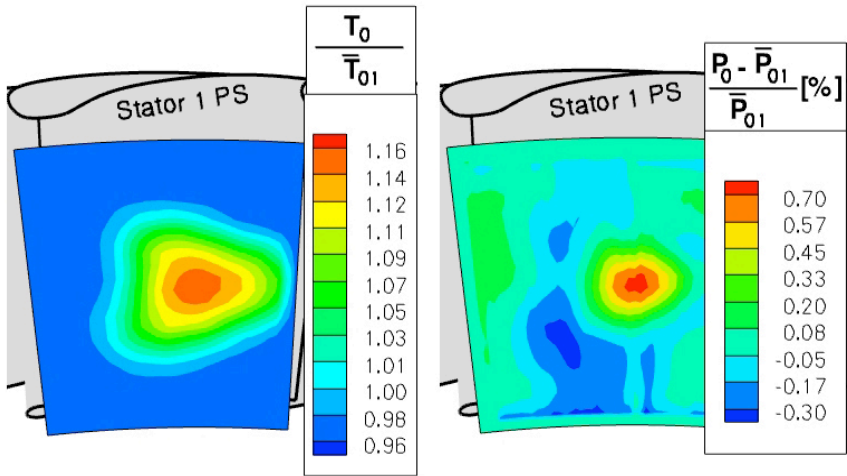
Figure 4.31 Measured, time averaged total temperature distribution upstream of the turbine (A-plane) and the deviation of the measured total pressure from the mean level

At the inlet the experimentally measured flow field is imposed. Figure 4.31 shows the measured total temperature and total pressure distributions averaged in time. Additionally, the measured flow angles are also imposed at the inlet plane. The turbulence intensity at the turbine inlet is considerably increased by the presence of the hot streak generator. As shown in Figure 4.32, the measurements show a peak intensity level of 10% within the hot streak. As provided by the measurement the turbulence intensity distribution is imposed at the inlet as well. However, there is an uncertainty about the value of the turbulent length scale which was not available in the experimental measurements. In this study the value of the turbulent length scale is set according to the length scale estimations within the fully developed pipe flows. Accordingly, the turbulent length scale is set to 3.8% of the hydraulic diameter of the non-circular hot streak injector which results in 2mm for the current study.

Additionally, no slip, adiabatic wall boundary conditions are applied at the solid walls. At the rotor outlet the average static pressure level at the hub endwall is specified according to the total–to-static pressure ratio of the first stage of the turbine. During the measurement this ratio is kept constant. Further settings of the simulation are the same as the one in Section 4.6.4. In this study the GPU accelerated version of "MULTI3" is used along with the developed anisotropic artificial dissipation scheme.
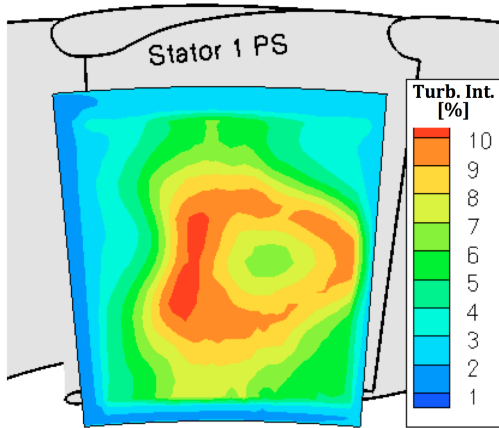
Figure 4.32 The time averaged turbulence intensity levels at the turbine inlet

RESULTS

The simulations have been conducted using the existing Mach number scaled isotropic artificial dissipation algorithm and using the cell Reynolds scaled anisotropic artificial dissipation algorithm. The level of the smoothing coefficients used for the isotropic and anisotropic artificial dissipation approaches are given in Table 4.3.

i) Downstream of the Stator (B-plane) - Effect of Turbulence on Mixing

The flow upstream of the turbine is highly turbulent which affects the mixing of the hot streak considerably. Figure 4.33 shows the measured, time averaged total temperature distribution downstream of the stator. Simulations neglecting the turbulence content of the incoming flow field underestimates the mixing of the hot streak within the stator. Figure 4.34 shows the resulting total temperature distribution downstream of the stator without considering the upstream turbulence field. As shown, the peak temperature within the hot streak is considerably overestimated due to the missing effect of the turbulence. On the other hand, imposing the turbulence intensity as measured and assigning the length scale as discussed the temperature field downstream of the stator is predicted quite close to the measurements. Figure 4.35 shows the predicted time averaged, total temperature field downstream of the stator.
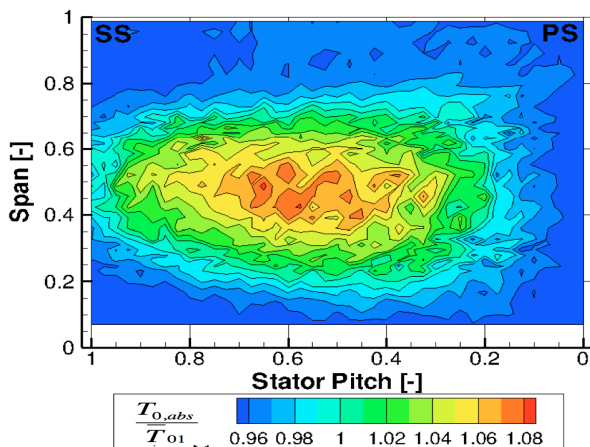
Figure 4.33 The measured, time averaged absolute total temperature distribution downstream of the stator (non-dimensionalized with respect to the mean total temperature at the turbine inlet – A plane)
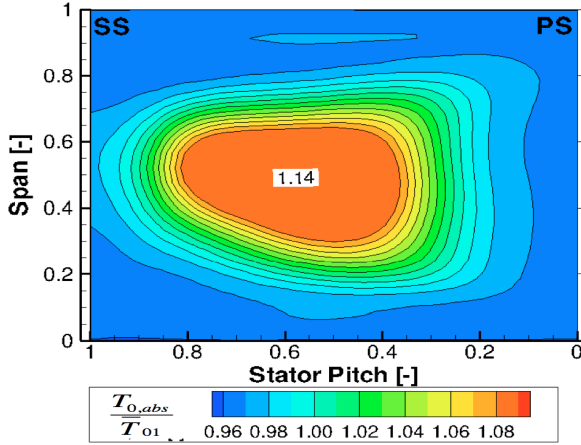
Figure 4.34 The calculated (without considering turbulence field upstream of the stator), time averaged absolute total temperature distribution downstream of the stator (non-dimensionalized with respect to the mean total temperature at the turbine inlet – A plane)
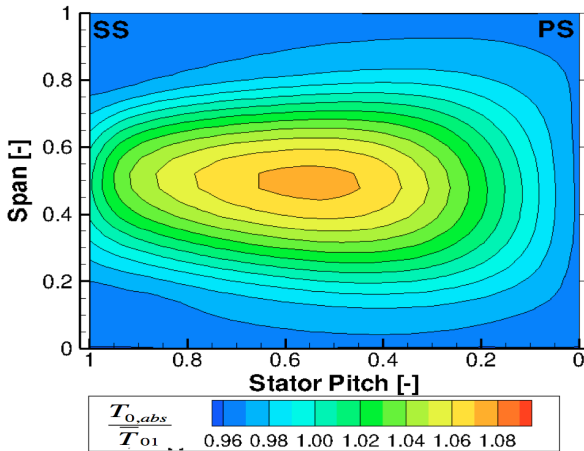
Figure 4.35 The calculated (considering turbulence field upstream of the stator), time averaged absolute total temperature distribution downstream of the stator (non-dimensionalized with respect to the mean total temperature at the turbine inlet – A plane)

ii) Downstream of the Rotor (C-plane)

The footprint of the hot streak downstream of the rotor blade is investigated in relative frame of reference. The time resolved temperature measurements enables to convert the measurement data into the rotor relative frame of reference. In this manner the distribution of the hot streak within the rotor pitch can be visualized.

Figure 4.36 The time averaged, relative total temperature distribution downstream of the rotor in rotor relative frame of reference (C-plane); the experimental measurement on the left and the numerical prediction on the right

Figure 4.36 shows the relative total temperature distributions time averaged in the rotor relative frame of reference over a time period equal for the rotor blade to pass one stator pitch. The simulation result is obtained using the cell Reynolds scaled anisotropic artificial dissipation. In general, the simulation captures the main features about the hot streak distribution within the rotor blade quite accurately. In both of the results the peak

temperature levels are positioned closer to the pressure side of the rotor blade which is in accordance with the previously developed theories about the hot streak migration physics. As explained with the Kerrobrock-Mikolajczek [11] principle, due to their larger relative flow angles hot streaks impinge on the rotor pressure side. Also the spanwise migration of the hot streak at the rotor pressure and the migration oft he hot streak into the tip leakage vortex are quite accurately captured in the simulations. However, the level of the peak temperature is underestimated in the computational results. The difference is 0.6 % of the mean total temperature level at the turbine inlet. This would correspond to about 12 K underestimation of the peak temperatures in engine realistic conditions. The mismatch in the peak temperature levels is due to the overestimation of the turbulence mixing. The temperature levels inside the secondary flows are accordingly overestimated.
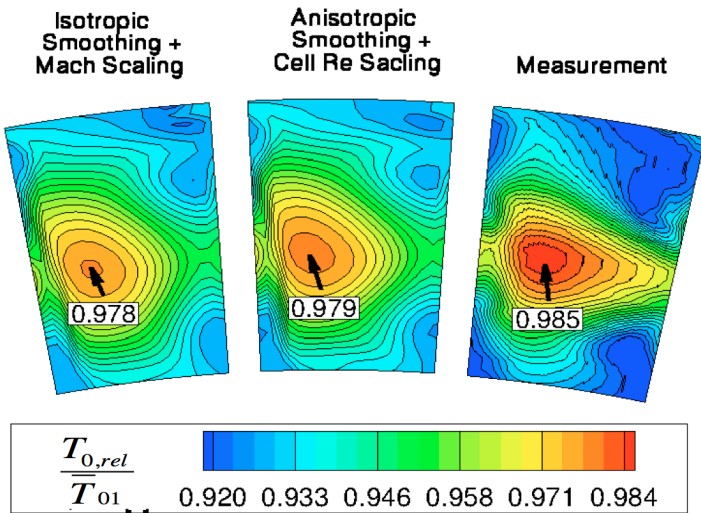
Figure 4.37 The time averaged relative total temperature predictions downstream of the rotor row alongside the measurement
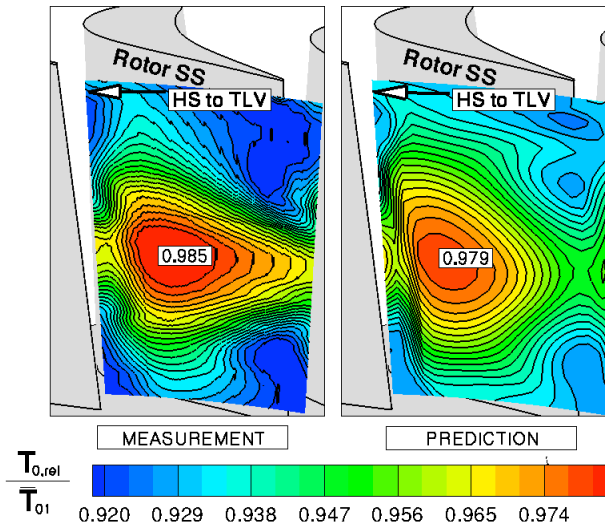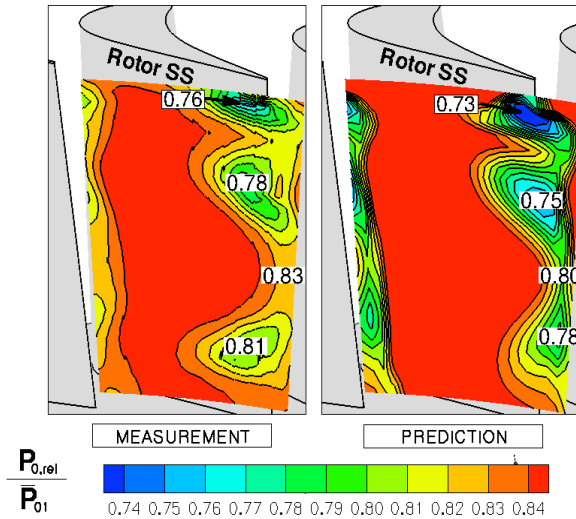
Figure 4.38 The time averaged, relative total pressure distribution downstream of the rotor in rotor relative frame of reference (C-plane); the experimental measurement on the left and the numerical prediction on the right

Figure 4.37 shows the temperature distributions downstream of the rotor plane calculated both with the isotopic artificial dissipation algorithm and also with the cell Reynolds scaled anisotropic artificial dissipation algorithm. As shown, the anisotropic artificial dissipation predicts the peak temperature slightly closer to the experiments. However, the effect of the artificial dissipation scheme is not as pronounced as it was in the loss predictions downstream of the rotor shown in Figure 4.25. The similarity between the two predictions indicates that both dissipation schemes add a comparable level of numerical diffusion away from the walls where the cell aspect ratios are close to 1 as opposed to the cells inside the O-grids. So, the advantage of the anisotropic smoothing is reduced but it still remains. Figure 4.38 shows the time averaged relative total pressure prediction alongside the measurements. Consistent with the predictions in the previous study in Section 4.6.4 the level of the total pressure is underestimated in the simulations.

4.7.   Concluding Remarks and Computational Cost

Adjusting the level of the artificial dissipation is crucial for the accuracy and the stability of the numerical schemes. Although the added artificial dissipation does not reduce the order of the numerical scheme it can still have considerable effect on the accuracy if the mesh insensitive solution is not reached. Depending on the type of the artificial dissipation scheme used the required mesh resolution for the mesh-insensitive result differs. Using a higher fidelity dissipation scheme ensures the mesh-insensitive solution to be reached at a lower grid resolution than the simplistic dissipation schemes can reach. Schemes that can alleviate the minimum mesh resolution needed for a mesh-independent solution without sacrificing from the stability are highly desired for the CFD community.

In this regard a new anisotropic approach for the scaling of the smoothing coefficients has been developed to be used in JST type scalar, non-linear artificial dissipation schemes. For the scaling of the smoothing coefficients the local CFL number in each cell directions and as well as the level of the modeled eddy viscosity have been taken into account. This approach has been applied to Ni's Lax-Wendroff scheme which has its stability limit at σ = 1.0. The scheme's stability region is divided into three zones where a different scaling approach has been applied for each of the three zones. No artificial dissipation is required for the Lax-Wendroff scheme for local $\sigma >$ 0.7. It is important to keep the CFL number as close as possible to the stability limit to make use of the inherent diffusive characteristics of the scheme itself without requiring any additional artificial dissipation.

It has been demonstrated that this approach has increased the accuracy of the scheme on resolving and modeling of both the laminar and turbulent boundary layers. The effect of including the modeled eddy viscosity in the scaling of the smoothing coefficients is clearly demonstrated on the multi-row, axial turbine simulations where the flow in downstream blade rows is dominated by considerably high eddy viscosity levels. The developed anisotropic scaling approach is not limited to the Ni's Lax-Wendroff scheme and might be also beneficial for other time integration schemes such as Runge-Kutta as long as the scheme's inherent damping characteristics depend on the CFL number.

The additional accuracy of the present dissipation scheme leads to about 30% increase in the computational time over the simplistic isotropic artificial dissipation schemes on the modern GPU architectures. However, the additional cost over the existing anisotropic dissipation schemes in the literature [77] is less than 5% where only additionally the local CFL numbers and the cell Reynolds numbers in the three cell directions have to be calculated.

5. Hot Streak Migration in HP Turbine with Axisymmetric Endwalls

In this chapter the hot streak migration pattern within the HP turbine stage is numerically investigated using an unsteady, multi-row particle tracking tool in conjunction with the unsteady simulations. All the simulations have been conducted with the in-house URANS solver "MULTI3". The inlet boundary conditions are taken from the hot streak experiment conducted in the axial research turbine facility "LISA" at ETH Zurich. Numerical results are validated extensively with the aid of the measurement data.

In this chapter two circular hot streaks with the same size but with different temperature ratios have been considered. The experimentally generated flow scenarios and their purpose of usage in this numerical study are summarized in Table 5.1. The measurements were conducted with the in-house developed fast response probe technologies "FENT" [63] and "FRAP-HT" [64]. The fast response entropy probe "FENT" enables to measure both the pressure and the temperature and as well as the yaw angle in a time-resolved manner. However, due to its maximum temperature limitation this probe could only be used for the low temperature hot streak case, where the max-to-mean temperature ratio was about 1.18. Due to the availability of the time resolved data this hot streak is used for the code validation study. For the high temperature hot streak measurements the fast response aerodynamic probe "FRAP-HT" was used which delivers time-resolved pressure and flow angle data but can conduct a steady temperature field measurement. Due to its higher temperature ratio this hot streak case is expected to have a more pronounced effect on the turbine aerodynamics which is investigated in detail with the aid of the unsteady particle tracking tool.

Using the lessons learned from the detailed study of the hot streak migration pattern, attempts in modifying the turbine inlet boundary

conditions are considered that would reduce the incident heat load on the rotor blade tip.

Table 5.1 Experimentally generated flow scenarios and their purpose of usage in the numerical study

	T_{peak} / T_{mean}	Measurement Techniques	Usage in this numerical study
Low temp. hot streak	1.18	FENT	Code Validation
High temp. hot streak	1.30	FRAP - HT	Particle Tracking Study

5.1. Turbine Geometry

In this study "LISA-D" case turbine geometry has been used. The high work turbine consists of two stationary rows having 36 stator blades each and a rotating row composed of 54 rotor blades. First stage stator has a constant exit angle design and stacked radially along its leading edge. The profile shape, with a large leading edge radius and large profile thickness was chosen to model the shape of an internally cooled high-pressure gas turbine vane. Details of the geometry are given in Chapter 1.

5.2. Numerical Model

For this numerical study one stage of the one-and-a half stage turbine is modeled. Due to its integer stator – rotor ratio only $1/18^{th}$ of the whole annulus is included in the mesh, which consists of two stator blade passages and three rotor blade passages. The rotor blade has a flat blade tip with a tip clearance gap of about 1% of the rotor blade span.

The computational mesh has been generated with the in-house multi-block mesh generator "MEHSBOUND" [41]. The stator and rotor passages have been meshed separately. The tip clearance gap is also included in the rotor mesh. The separately meshed rows are merged afterwards in a multi-pitch and multi-row arrangement. The wall mesh of the computational model is shown in Figure 5.1.

| STATOR 1 | ROTOR |

| ROTOR TIP LEADING EDGE | ROTOR TIP TRAILING EDGE |
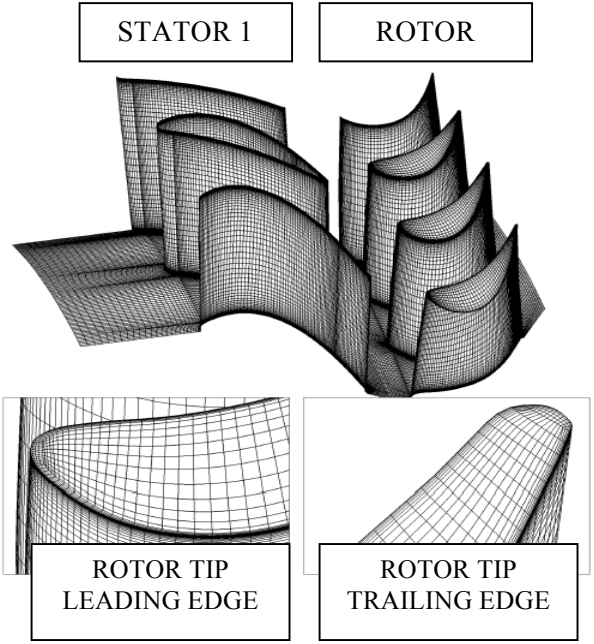
Figure 5.1 The generated structured, multi-block low Reynolds mesh with the rotor tip leading and trailing edges zoomed in

In order to decide for the required mesh size and the wall resolution, a grid sensitivity study has been conducted. For that purpose, three different meshes with different wall resolutions have been generated. The total number of nodes for the multi-row meshes and the average y+ values of the first grid nodes from the walls are shown in Table 5.2.

Table 5.2 The wall resolutions of the meshes generated and their cell sizes

Mesh	y^+ (rotor tip)	y^+ (side walls)	# of cells (millions)
coarse	6.2	1.6	2.7
intermediate	4.9	1.6	3.3
fine	3.3	1.2	3.4

In this study the algebraic Baldwin-Lomax [45] turbulence model has been used. This model is favorable in terms of its robustness and low computation cost and is widely used in aerospace applications. It gives quite accurate predictions within the boundary layer. However, far from the boundary layers the model is unable of capturing the turbulent flow physics due to the lack of governing equations of turbulent flow.

The time resolved simulations have been conducted via dual time stepping method first used by Jameson et. al. [57] which uses a second order backward Euler time integration. At the interface between the rows a sliding interface algorithm has been used to transfer the computational data between the rows. One period, the time required for the rotor to rotate two stator passages, is divided into 100 physical time steps and in each physical time step 120 sub-iterations have been conducted.

5.2.1. Convergence and Run Time

The runs have been conducted on the computer cluster Brutus which is a joint cluster built by the shares of different labs and departments within ETHZ. OpenMP parallelized version of "MULTI3" can run parallel on shared memory architectures with a reasonable efficiency up to 8 cores. With the negligible computational cost of the zero-equation Baldwin-Lomax turbulence model each iteration took about 5 seconds on 8 CPU cores for the fine mesh composed of 3.4 million cells.

To decide for the convergence of the unsteady runs the periodicity of the pressure field at the row interface has been monitored. In that regard, monitoring points have been placed at the periodic faces at the row interface. Figure 5.2 shows the variation of the static pressure at one of

those monitoring points placed in the rotating rotor domain at the row interface where periodic fluctuations in the pressure level are observed due to the relative backward rotation of the stator blades. After 500 time steps corresponding to a time frame of 15 rotor blade passings a periodic pressure field at the row interface has been captured.
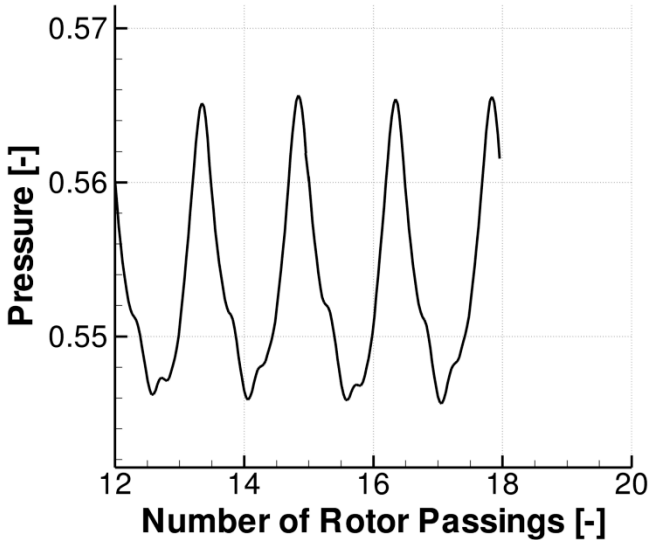
Figure 5.2 The static pressure fluctuations at one of the monitoring points positioned in the stator domain at the stator - rotor interface

5.2.2. Grid Sensitivity Study

For the grid sensitivity study time resolved simulations have been conducted using the three different meshes with the specifications given in Table 5.2 and utilizing the inlet boundary conditions taken from the measurements. The calculated loss coefficients downstream of the rotor row are compared afterwards with the measurement data at the same plane. Figure 5.3 shows the circumferentially mass averaged relative loss coefficients in spanwise direction derived from the simulations and from the measurement data. Comparing the numerical results with the experimental data a qualitative match in the loss distributions is observed.

The three main secondary loss structures such as the tip leakage vortex and the two passage vortices (upper and lower) have been captured with all of the meshes. However, there are slight variations in the spanwise positions and in the loss intensities predicted. It can be concluded that the fine mesh leads to the closest results relative to the measurements especially in the upper passage vortex area. Moreover, the marginal difference in the loss predictions between the medium and the large mesh indicates that a grid insensitive solution is captured. Based on the loss distribution predictions, the fine mesh has been used for all the simulations which will be shown in the remaining part of this chapter.
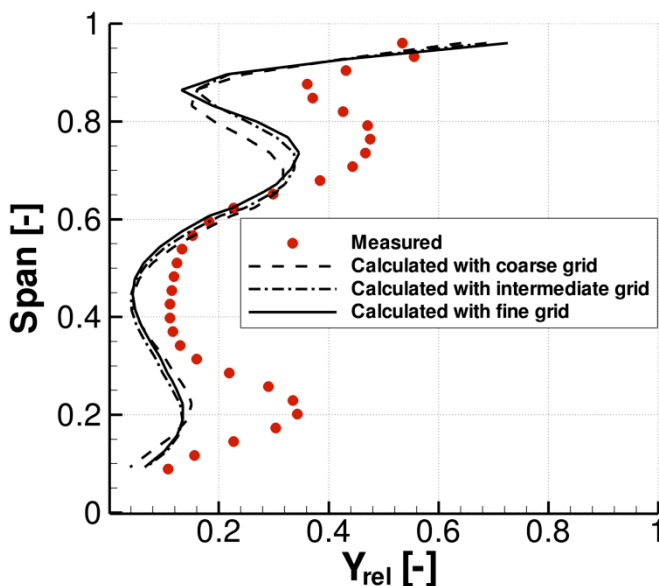
Figure 5.3 The numerically predicted relative total pressure loss coefficients using different mesh sizes vs. the experimental measurements ($Y_{rel} = (P_{02,rel} - P_{03,rel})/(P_{03,rel} - P_3)$)

5.2.3. Validation Study

For the code validation the low temperature hot streak has been used for

which time resolved temperature measurements have been conducted. In that regard the measured flow field data upstream of the turbine is imposed as the inlet boundary condition and predictions of the solver will be compared with the measurements downstream of the rotor blade.

5.2.3.1.   Inlet Boundary Conditions

At the domain inlet total pressure, total temperature, and flow angle distributions measured upstream of the stator have been imposed. The total pressure and total temperature distributions are shown in Figure 5.4.
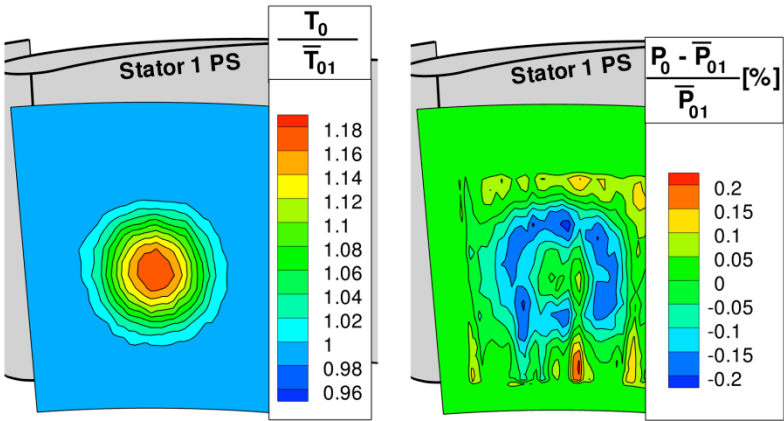
Figure 5.4 The experimentally measured total temperature distribution on the left and the deviation of the measured total pressure in percentage from the mean level on the right

The generated hot streak has a circular shape with a peak to mean temperature ratio of about 1.18. Additionally, the total pressure distribution is shown in terms of the percentage deviation from the mean pressure level, where the wake of the injector tube is shown with a deficit in total pressure distribution which is about 0.2% of the mean pressure level in magnitude. As it is in the experiment a single hot streak is imposed upstream of one of the stators present in the domain. However, different from the experiment

this configuration corresponds to a ratio of one hot streak per two stator blades, because a circumferential periodicity is imposed on the sides of the domain. But the small size of the hot streak prevented it to interact with the other hot streak emerged as a result of the periodic boundary condition. So the isolated hot streak can be simulated within the 20° section of the turbine stage. Otherwise, the circumferential extent of the domain had to be doubled which would increase the computational cost.

5.2.3.2.   Rotor Exit Flow Field

Time-resolved simulations have been conducted with the inlet boundary conditions mentioned above and the results are compared with the measurements downstream of the rotor row in terms of accuracy. The two most important quantities that will be used in the validation study are the total pressure and total temperature distributions which are measured in stationary plane of reference in a time resolved manner. However, the availability of the time resolved temperature data for the low temperature hot streak case enables the conversion of the raw data present in stationary frame of reference into the rotor relative frame of reference.
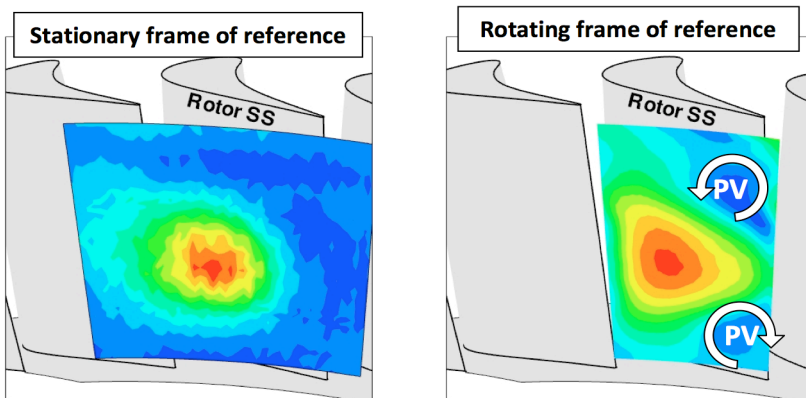
Figure 5.5 Time averaged, measured relative total temperature distributions downstream of the rotor (in stationary frame of reference on the left and in rotating frame of reference on the right)

In Figure 5.5 on the left hand side the measured, time averaged, relative total temperature distribution is shown downstream of the rotor blade in absolute frame of reference and on the right hand side the same data has been converted into the rotor relative frame of reference. As shown, plotting the flow field in the rotor relative frame gives a deeper insight about the flow patterns within the rotor passage.

Figure 5.6 The time averaged, relative total temperature distribution downstream of the rotor in rotor relative frame of reference (plane C); the experimental measurement on the left and the numerical prediction on the right (TLV : tip leakage vortex; PV : passage vortex)

Figure 5.6 shows both the predicted and the measured relative total temperature distributions downstream of the rotor plane in the relative frame of reference. These distributions have been averaged over a time frame equal for the rotor blade to pass the stator pitch which the hot streak was migrating through. In both of the results the peak temperature levels are positioned closer to the pressure side of the rotor blade which is in accordance with the previously developed theories about the hot streak migration physics. As explained with the Kerrobrock- Mikolajczek [11]

principle, due to their larger relative flow angles hot streaks impinge on the
rotor pressure side which can be observed in Figure 5.6 with the position of
the peak temperature region being closer to the pressure side downstream
of the rotor passage. The essence of this principle is shown schematically in
Figure 5.7.
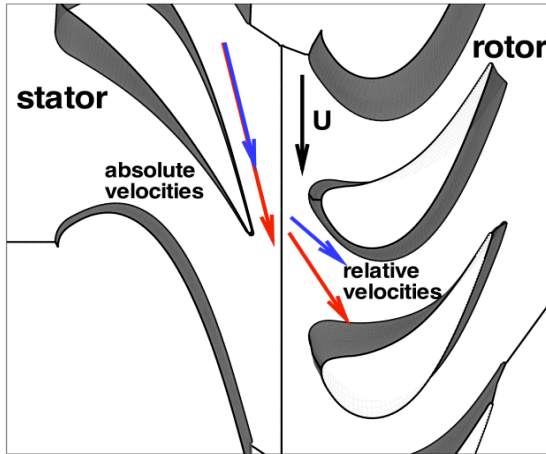
Figure 5.7 Schematic of the Kerrobrock- Mikolajczek [11] principle
explaining the migration of hot streaks towards the rotor pressure side

Secondly, when compared to the suction side there is a larger spanwise
coverage of the hot streak at the rotor pressure side. This is due to the
inherent secondary flow patterns within the rotor passage and the
interaction of the hot streak secondary flows with these. In contrary to the
behavior at the pressure side the hot streak is accumulated in between the
two passage vortices at about the mid-span. The passage vortices located at
the suction side of the rotor blade which are marked with reduced relative
total temperature regions prevent the hot streak from migrating towards the
endwalls. The lower relative total temperature levels in the secondary loss
cores are due to the dissipation of heat from the relatively hot loss cores to
the surrounding. Both in the CFD prediction and also in the measurements
no major hot streak migration to the tip leakage vortex was observed.
Figure 5.8 shows both the predicted and the measured relative total pressure
distributions downstream of the rotor plane in the relative frame of

reference. As shown, the main distinct loss structures are qualitatively predicted by the solver. The footprints of the loss structures are more prominent in the numerical results which indicates an underestimation of turbulent mixing in the near wake region of the blade. One reason of the underprediction of the size of the hub passage vortex is due to the absence of the rim seal cavity in the computational model.
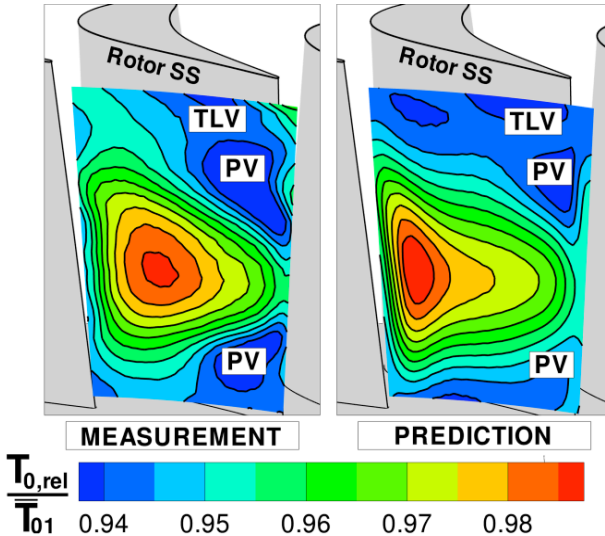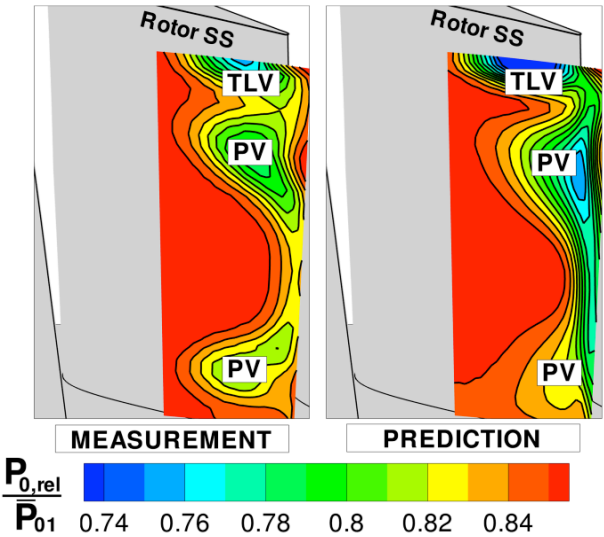

Figure 5.8 The time averaged, relative total pressure distribution downstream of the rotor in rotor relative frame of reference (plane C); the experimental measurement on the left and the numerical prediction on the right (TLV : tip leakage vortex, PV : passage vortex)

5.3. Analysis of the Hot Streak Migration Pattern in the HP Turbine Stage via Unsteady Particle Tracking Tool

Hot streak migration in HP turbine is an unsteady phenomenon which necessitates a three-dimensional and unsteady simulation for capturing the correct flow physics [15]. These computationally very intense simulations

generate large amount of data which is difficult to analyze and extract the essence of. With the aid of the in-house developed particle tracking tool the hot streak migration pattern in the HP turbine is analyzed and practical benefits for the designers are aimed to come up with.
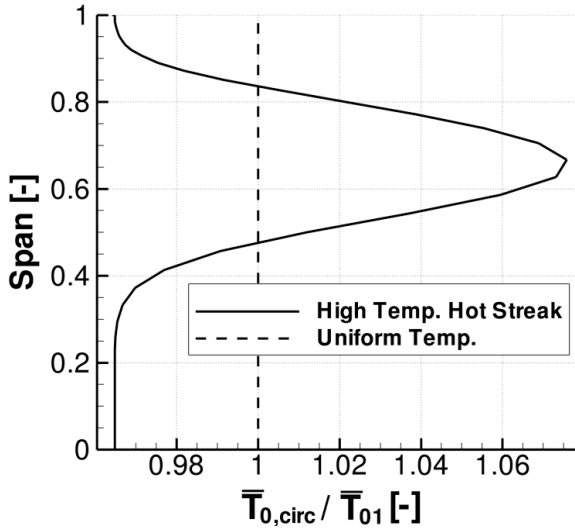
Figure 5.9 The circumferentially mass averaged total temperature profiles used as the inlet boundary conditions for the simulations conducted to study the migration patterns inside the turbine

5.3.1. Boundary Conditions and Settings for the Particle Tracking Study

The hot streak migration pattern analysis is conducted with the high temperature hot streak case. It is expected that due to the higher temperature ratio, it will have a more pronounced effect on the turbine aerodynamics. Moreover, the spanwise position of the peak temperature point is raised to 65% span to enhance the effect of the hot streak on the rotor blade tip, since no considerable hot streak migration to the rotor tip leakage vortex was observed in the measurements. Additionally, for comparison the same study has also been conducted with a uniform total

temperature distribution imposed at the turbine inlet and the temperature level was selected in a manner such that both cases have the same mass averaged turbine inlet total temperature levels. The circumferentially mass averaged temperature profiles are shown in Figure 5.9. Besides, both of the cases have the same uniform inlet total pressure distributions and an axial inflow condition is set at the inlet for both of the simulations. Under these circumstances the difference in the flow patterns has to be attributed only to the change in the total temperature distribution.

With the boundary conditions explained above two time resolved simulations have been carried out. The time step used in the unsteady simulations is 3% of one rotor blade passing period which in total makes up 100 snapshots for a time frame covering three rotor blade passings. Unsteady flow field data has been written out which the particle tracking tool continuously reads for the marching of the particles released.

The flow field inside the rotor row shows a periodic pattern with the passing of the upstream stator blades. Especially the rotor secondary flow features are strongly influenced by that and the tip leakage flow is one of those. Depending on the relative position between the stator and the rotor the tip leakage mass flow and the intensity of the tip leakage vortex vary in time. In order to capture the variation of the migration pattern in time due to the rotation of the rotor blade which is the most dominant unsteadiness in the flow, particles are released from the turbine inlet at consecutive snapshots. So at every set of particle release the rotor is situated in a different relative position with respect to the stator. For this particular study a new set of particles has been released at every time step within the time frame of one rotor blade passing which makes up 33 sets of release within one rotor blade passing period. Every set 2400 particles have been released at the turbine inlet. These particles are uniformly distributed on an area bordered by the thick black curve covering 25% of the blade span and 1.3 times the stator pitch. The number of the particles should be related to the mesh density in the circumferential and radial directions. Accordingly, roughly about four particles are released per cell. After releasing the particles they are migrated within the turbine according to the velocity field depending on their position and time. Meanwhile, the rotor blade is also rotated continuously. All the particles are marched with the same time step until they leave the computational domain. Using the same time step for all

the particles might cause for some particles close to the solid boundaries unphysical situations such as migrating of them into the solid walls if the time step used for the marching of the particles is much larger than the local allowable time step defined by the CFL criteria. For those particles an additional impermeability condition is imposed as discussed previously in Section 2.3.
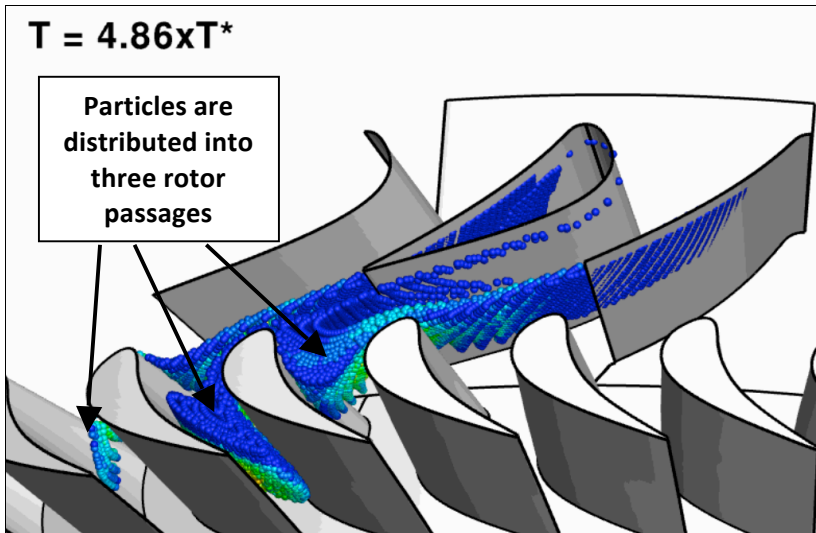
Figure 5.10 A snapshot in time showing the positions and local absolute total temperature levels of the particles released in different instants in time upstream of the stator (T* = time required for the rotor to rotate one rotor pitch)

This unsteady particle tracking study covered roughly 80,000 particles both for the hot streak and for the uniform total temperature cases. Marching all these particles is computationally very expensive. However, since tracking each set of particles is computationally independent from each other, all the 33 sets can be run in parallel and simulations can be finished in a reasonable time frame provided that enough hardware is present. On the present hardware on computer cluster Brutus [87] each of the runs took

about 30 hours. Figure 5.10 shows a snapshot in time while all the 80,000 particles were migrating through the turbine stage. While the particles are marched within the turbine, their positions are written out to a text file in a continuous manner. After all the particles have left the domain, text data consisting of time and space information for all the particles released will be written out. This data can be post-processed afterwards depending on the needs. For this particular study a post-processing tool run on the data and detected the particles migrating to the rotor blade tip among all released at the turbine inlet.

5.3.2. Observations on the Migration Pattern to the Rotor Blade Tip

In Figure 5.11 the pathlines of the particles migrating through the rotor tip gap are shown among all released at a particular set. Here the pathlines are drawn in relative frame of reference. As shown by the colors of the pathlines, the particles have been correctly recognized by the post-processor when they lay within the rotor blade tip gap. Another observation is that the particles migrate to three subsequent rotor blade tips even though they have been released at the same axial position and at the same time. This is due to the fact that they have been released at different circumferential positions upstream of the stator. Depending on their circumferential positions the particles end up at varying times and at different circumferential positions at the stator exit plane and this affects which rotor blade they approach. For example; by the time a slow particle has approached the rotor row, the rotor blade which the fast particles have migrated on might have been passed already.
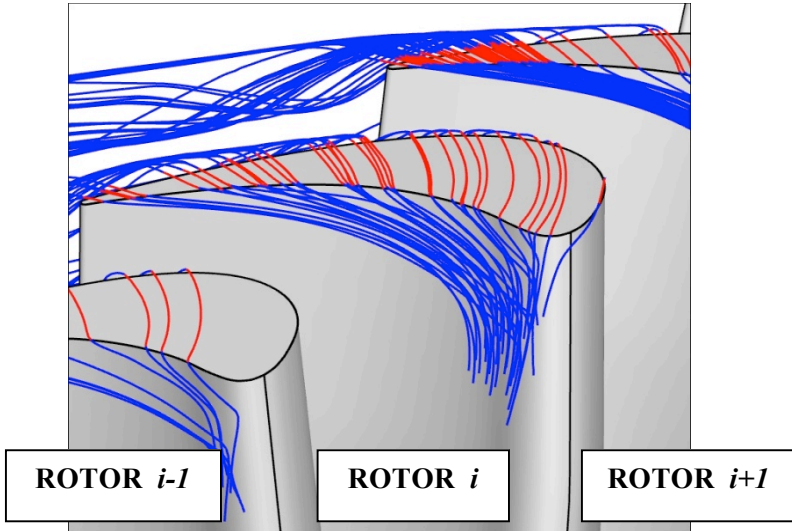
Figure 5.11 The particle paths (rotor relative frame of reference) migrating through the rotor tip clearance among all released upstream of the turbine at one instant in time – once the particle is in the tip gap it is detected by the post processor (shown in red when they are in the tip gap)

After identifying the particles migrating to the rotor blade tip their origins at the turbine inlet are next located. Figure 5.12 shows the positions of the particles at the inlet plane which have passed through the rotor tip gap among all released within one set of particles. Here, the three different zones can be identified. As mentioned before, the particles released upstream of the stator can migrate to three subsequent rotor blade tips. And in Figure 5.12 it is shown that the distributions of the particles moving to three subsequent rotor blade tips are circumferentially separated. The particles released from zone 1 migrate to the rotor blade with the number $i-1$, the particles released from zone 2 to the rotor blade i, and the particles released from zone 3 migrate to the next rotor blade tip with the number $i+1$. As shown, the number of the particles released from the zone 2 is higher compared to the number of the particles in the other zones.

Figure 5.12 The distribution of the particles migrating to the rotor blade tip released at the same instant in time upstream of the stator

The same detection has been carried out for all the sets of particles released at different instances in time. For the subsequent sets particles released from the other positions at the inlet plane migrate to the rotor blade tip, because the rotor keeps rotating and the time a new set of particle has been released the rotor is positioned at a different relative position with respect to the stator. As the rotor keeps rotating the particles that are positioned towards the suction side of the stator migrate to the rotor blade tip. Figure 5.13 shows the distribution of the particles moving to the rotor blade tip released at different instants in time upstream of the turbine. As shown with the enumeration, in the subsequent releases the particle's positions shift towards the direction of the rotation of the rotor blade. The behavior is observed in all the three zones mentioned before. After particles directly at the suction side of the blade migrate to the rotor blade tip again particles released at the pressure side of the stator migrate to the rotor tip and it continues in a periodic pattern with the rotation of the rotor blade. Finally, locating the initial positions of all the particles moving to the rotor blade tip

among all the 33 sets of particles released within a time frame covering one rotor blade passing period a time-averaged view about the migration pattern to the rotor blade tip can be obtained.
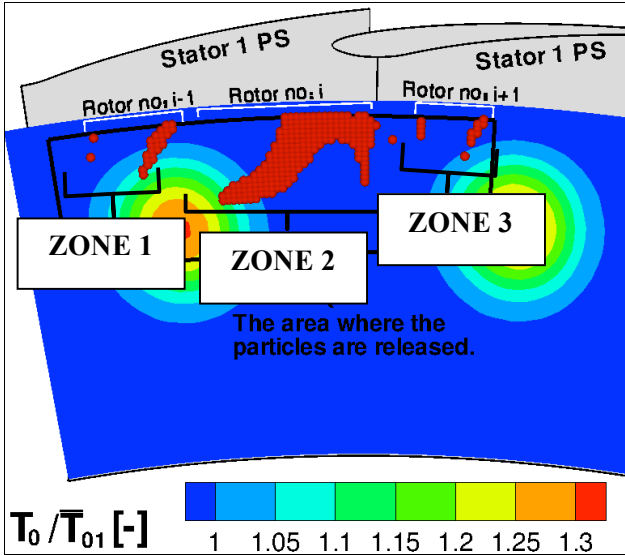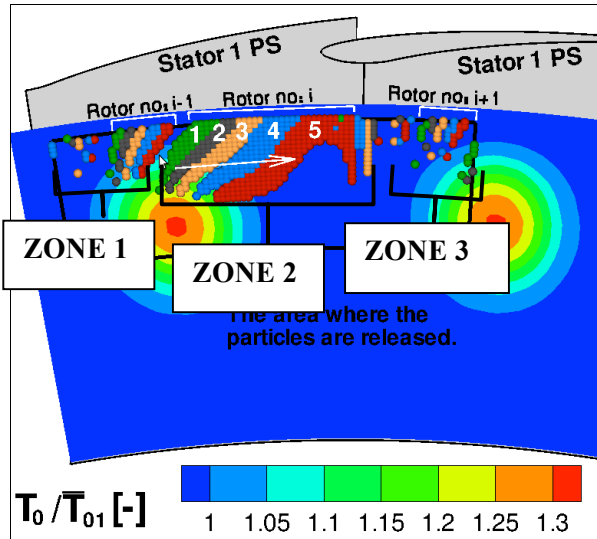

Figure 5.13 The distribution of the particles migrating to the rotor blade tip released at different instants in time upstream of the stator

Figure 5.14 shows the initial positions of all the particles released from the stator inlet plane within the time frame of one rotor blade passing and finally migrate through the rotor blade tip gap. As expected, mainly particles at high radial positions migrate to the rotor blade tip. Additionally, there is non-uniformity in the distribution of these particles in the circumferential direction showing an increasing trend in the number of the particles moving from the pressure side to the suction side of the stator. Moreover, particles closer to the suction side of the stator blade can migrate to the rotor blade tip even though they have been released at lower spanwise positions at the inlet plane compared to the particles close to the pressure side. According to this observation main hot streak impingement on the rotor blade tip should have been originated close to the suction side

taking into account that the peak in the radial temperature profile is positioned around the midspan.

Figure 5.14 The distribution of the particles migrating to the rotor blade tip among all the particles released within a time frame of one rotor blade passing – when the hot streak is imposed at the inlet

However, it is yet unclear whether the observed circumferential non-uniformity is due to the effect of hot streaks or not. It is known that hot streaks generate secondary flows and thereby affect the streamline pattern inside rotating blade rows. In order to evaluate the effect of the hot streaks on the migration pattern to the rotor blade tip, the same particle tracking analysis will also be carried out for the uniform total temperature case whose radial temperature profile was compared with the one of the hot streak case in Figure 5.9. It is important to mention again that the mass averaged turbine inlet temperature levels are the same for these two scenarios.

5.3.3. Effect of Hot Streaks on Migration Pattern

Figure 5.15 shows the distribution of the particles moving to the rotor blade tip when the uniform total temperature distribution was imposed at the turbine inlet. Also in this case a circumferential non-uniformity in the distribution of the particles is observed. Similarly, particles closer to the suction side can migrate to the rotor blade tip even though they have been released at relatively lower spanwise positions. Since the circumferential non-uniformity in the distribution of the particles is also present for the uniform total temperature case it should have been caused by the main turbine aerodynamics which will be investigated further in the next sections of this study.
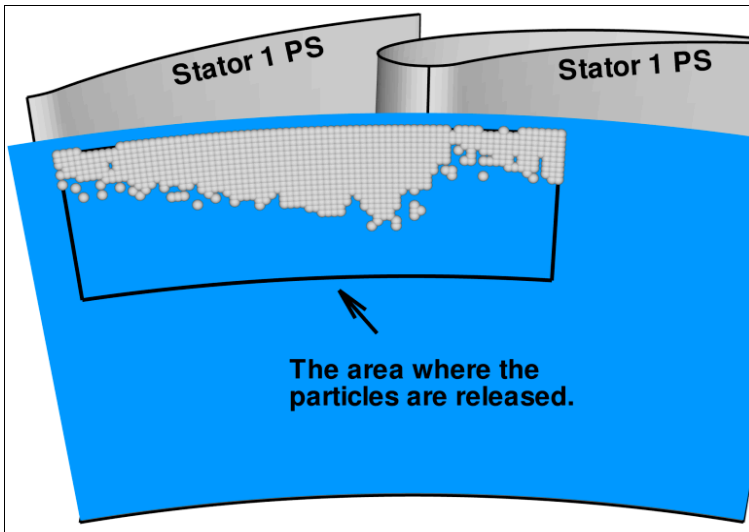
Figure 5.15 The distribution of the particles migrating to the rotor blade tip among all the particles released within a time frame of one rotor blade passing – when uniform total temperature distribution is imposed at the turbine inlet

To compare the migration patterns between the two cases namely with and without hot streak, both distribution patterns have been shown in Figure 5.16 on top of each other. The grey particles correspond to the case where the uniform total temperature distribution was imposed at the turbine inlet on the other hand, the red particles correspond to the case where the hot streak was imposed at the turbine inlet.
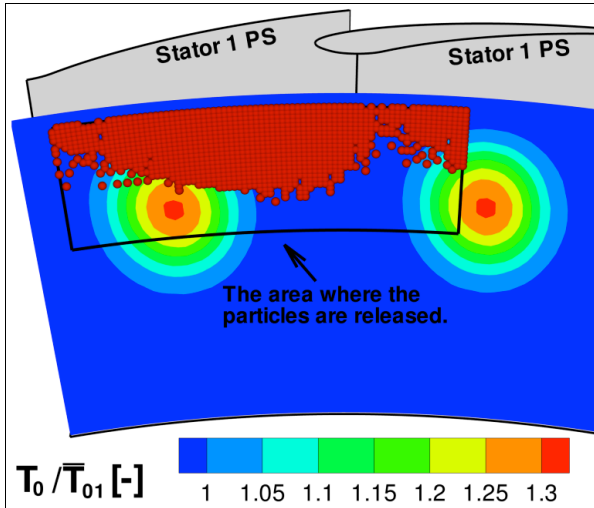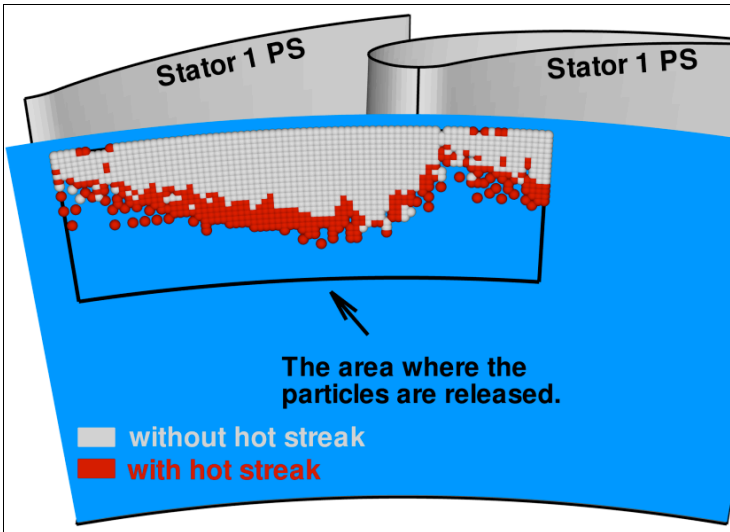

Figure 5.16 The distribution of the particles migrating to the rotor blade tip among all the particles released within a time frame of one rotor blade passing (particles shown in red in case of the hot streak is imposed at the turbine inlet and particles in grey when the uniform temperature distribution is imposed.)

As shown in Figure 5.16 the red particles are distributed to a larger spanwise extent. Even though they have started at lower spanwise positions compared to the grey particles they could migrate to the rotor blade tip which points out that hot streak particles should have shown an enhanced spanwise migration within the turbine in order to reach the rotor blade tip gap. This difference in the distribution patterns clearly shows the

enhancement in the spanwise transport which could only be taken place within the rotor row, since hot streaks do not change the streamline pattern inside the stator according to the Munk and Prim [10] principle. The observed enhancement in the radial migration is mentioned in the literature with the hot streak induced secondary flows in rotating blade rows.

5.4. Effect of Hot Streak Induced Secondary Flows on Spanwise Migration

Hot streaks change the streamline pattern inside rotating blade rows in two ways. First, they increase the relative flow angle and thereby they cause the preferential pressure side heating of the rotor blades. This is known as the Kerrebrock-Mikolajczak [11] effect. Secondly, hot streaks generate additional secondary flows by affecting the relative total pressure distribution upstream of the rotor row and thereby they increase the spanwise migration as shown in the particle tracking study. In a time resolved, multi-row simulation both of these mechanisms should be captured. In order to conduct a deeper analysis of the effect of the induced secondary flows on the rotor flow field an additional numerical study has been conducted that covers two steady, single rotor simulations with different inlet boundary conditions. In both of these simulations the measured time averaged flow field downstream of the stator 1 (B-plane) has been imposed as the inlet boundary conditions. To do that, first the absolute quantities measured in the stationary frame of reference are time averaged and converted into the rotor relative quantities and after that they are circumferentially averaged. It is important to point out that the flow angles and the total temperature distributions are circumferentially mass averaged and the total pressure distribution is circumferentially area averaged as discussed by Cumpsty and Horlock [88]. At the rotor inlet both simulations are imposed to experimentally measured flow angle (relative yaw and relative pitch) profiles and the relative total temperature distribution shown in Figure 5.17. Due to the increased absolute flow velocities inside the hot streak, the relative yaw angle at the rotor inlet is increased around the midspan. The dashed line indicates the relative yaw angle distribution if the hot streak was not present at the turbine inlet.

It is also important to point out that the hub endwall boundary layer is neglected in these profiles because it was outside of the region where the probe can access. The yaw angle outside of the measurement plane (about from 0% span to 8% span) is set to a constant level that is equal to the level at the very last point of the measurement plane. The relative total pressure distributions imposed at the rotor inlet plane are given in Figure 5.18. Both cases have a deficit in the relative total pressure level at around the midspan due to the disturbance added by the hot streak generator placed at the turbine inlet. As shown in Figure 5.4, it creates a certain level of disturbance and reduces the total pressure level. Ideally, there should have been no deficit in the relative total pressure level downstream of the stator at midspan which is indicated by the dashed black line. Among the two profiles Case 1 has the experimentally measured relative total pressure distribution and Case 2 has an artificially designed distribution to extract the additional rise in the relative total pressure due to the effect of the hot streak which enhances the spanwise migration inside the rotating blade rows.

Calculation Method of the Artificially Designed Relative Total Pressure for Case 2:

Inside the stator passage the flow is accelerated due to the imposed pressure difference and as shown by the Munk and Prim[10] principle, the non-uniformity in the temperature distribution does not lead to different Mach number levels downstream of the stationary blade rows. However, the absolute velocity level within the hot streak is higher compared to the surrounding due to the dependence of the speed of sound on the temperature level. This additional rise in the absolute velocity within the hot streak creates a rise in the relative Mach number distribution upstream of the rotor blade. In order to extract the effect of the rise in the relative Mach number level from the relative total pressure distribution, the free stream temperature levels are used in the calculation of the relative Mach number distribution instead of the real ones.
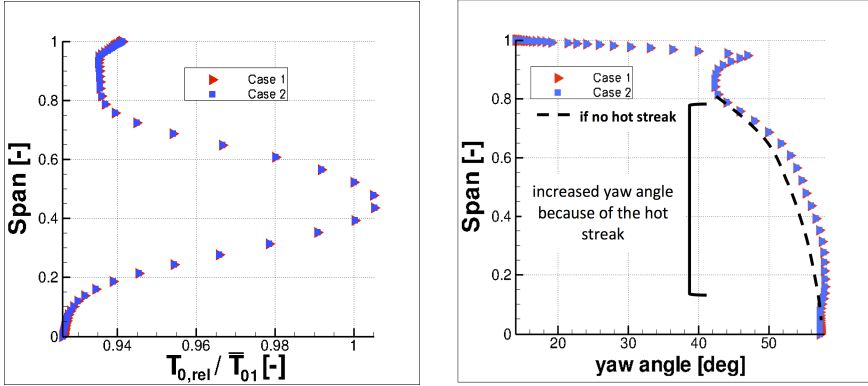
Figure 5.17 The circumferentially mass averaged relative total temperature profiles are shown on the left and the circumferentially mass averaged yaw angle profiles imposed upstream of the rotor blade are shown on the right
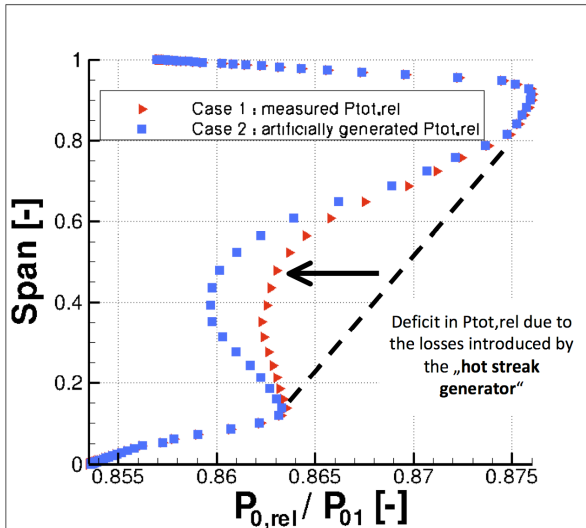
Figure 5.18 The circumferentially area averaged relative total pressure profiles imposed upstream of the rotor blade as inlet boundary conditions
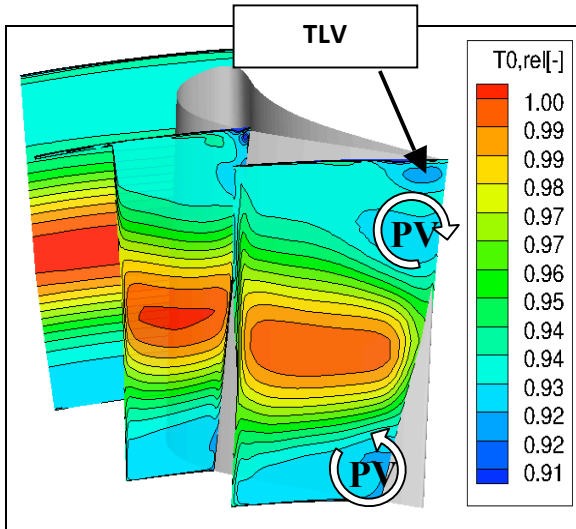
Figure 5.19 The evolution of the radial temperature profile within the rotor (TLV : tip leakage vortex; PV : passage vortex)

Two steady, single passage, single rotor row simulations have been conducted with the inlet boundary conditions mentioned above. Additionally, an adiabatic, no slip wall boundary condition is set at the solid walls. For these simulations the same rotor geometry is kept and the mesh is taken from the multi row mesh used in the previous simulations. For the closure of the RANS equations Baldwin-Lomax [38] turbulence model has been used. Figure 5.19 shows the convection of the imposed temperature profile for Case 1. As shown, downstream of the rotor the spanwise extents of the hot streaks on opposite side of the rotor blades differ. On the pressure side a relatively large spanwise coverage of the hot streak is observed and on the suction side the hot streak is confined between the two passage vortices marked.

Next, the resulting adiabatic blade wall temperature levels of these two flow scenarios (Case 1 & Case 2) are compared. Figure 5.20 shows the adiabatic wall temperature distributions in radial direction at 80% axial

chord for both sides of the blades and for both simulations. As shown in Figure 5.20, for both of the scenarios the temperature level at the pressure side is higher than the level at the suction side. It is important to point out that this result cannot be due to the Kerrebrock-Mikolajczak [11] effect, because upstream of the rotor the same yaw angle distributions are set for both of the simulations. The internal aerodynamics of the rotor passage leads to this differentiation of the adiabatic wall temperature levels between the two sides of the rotor blade.
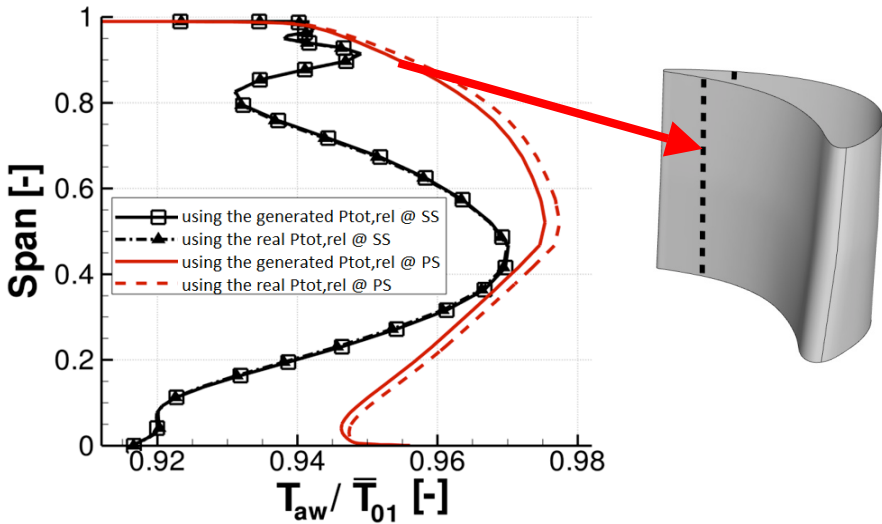
Figure 5.20 The numerically predicted spanwise adiabatic wall temperature distributions along the sides (red curves showing the distributions at the pressure side and the black curves showing the distributions at the suction side) of the rotor blade at 80% axial chord for both of the simulations using the real measured relative total pressure distribution and the generated artificial relative total pressure distribution

According to Figure 5.20 imposing the real relative total pressure distribution at the rotor inlet leads to a temperature rise at the rotor pressure side. The rise in the peak temperature level is by 0.25% of the mean total temperature level upstream of the stator that would correspond to a 5K

increase in temperature in real engine conditions. However, this prediction is based on the steady runs where the inlet conditions imposed upstream of the rotor have been circumferentially averaged. In an unsteady stator-rotor interaction the local rise in the relative total pressure level inside the hot streak would be more pronounced and the resulting effect on the rotor blade adiabatic wall temperatures would be more severe.

Moreover, there is a considerable increase in the temperature level close to the endwalls as well. The difference in the temperature levels close to the endwalls occurs even though the relative total pressure levels imposed at the rotor inlet close to the endwalls are the same for both of the scenarios. For instance, at 80% blade span both cases have the same relative inlet total pressure levels but the scenario with the real total pressure distribution has an increased adiabatic wall temperature level at that spanwise position at the pressure side which directly shows the three-dimensionality in the flow pattern. Consistent with the particle tracking analysis this study confirms the increase in the spanwise transport along the pressure side of the rotor blade by the hot streak induced secondary flows.

The radial adiabatic wall temperature profiles at the rotor suction side at the same axial chord are also shown for both simulations in Figure 5.20. On the contrary of the distribution at the pressure side, there is no difference in the adiabatic temperature levels between the two flow scenarios. So the change in the relative total pressure distribution upstream of the rotor blade does not affect the adiabatic wall temperature distribution at the rotor suction side. With this numerical investigation it has been confirmed for the first time that hot streak induced secondary flows influence the flow field only at the pressure side of the rotor blade where they increase the spread of the hot fluid in the spanwise direction. On the other hand, no observable change in the gas temperature level at the suction side wall indicates that the secondary flows are not effective at the blade suction side. This behavior was previously mentioned by Ong et al. [89] and has been clearly shown here in this numerical study.

5.5. Effect of the Stator Aerodynamics on the Hot Streak Migration

The circumferential non-uniformity in the migration pattern to the rotor blade tip was previously discussed. It has been shown that it was present not only when the hot streak was present at the turbine inlet but also when the uniform total temperature distribution was imposed at the inlet. In order to investigate the effect of the stator aerodynamics on the migration pattern, the distribution of the same particles migrating to the rotor blade tip shown in Figure 5.14 is also plotted right after they have left the stator passage. As shown in Figure 5.21, the particles are distributed more uniformly in the circumferential direction downstream of the stator blade compared to the distribution upstream. (The contours in the background represent the pitch angle distribution which will be referred to later on.) This observation points out the presence of a spanwise migration pattern within the stator row which will be investigated more directly using the streamlines.
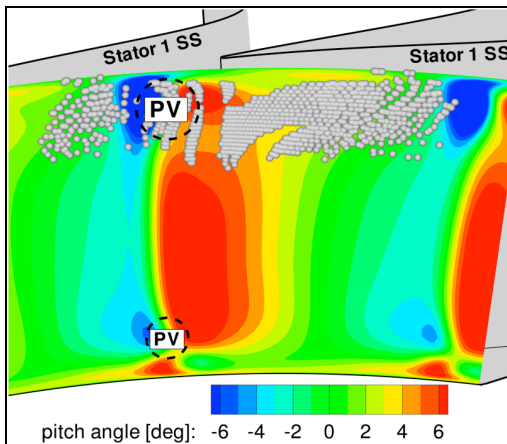
Figure 5.21 The numerically predicted time averaged pitch angle distribution in the background and the distribution of the particles migrating to the rotor blade tip among all the particles released within a time frame of one rotor blade passing

Due to the almost steady flow field conditions in the major part of the stator the streamlines do not considerably deviate from the pathlines or streaklines and using streamlines a qualitative analysis about the radial migration patterns inside the stator passage can be carried out. In that regard, two streamlines have been plotted using the time averaged flow field prediction. One of these streamlines has been plotted at the suction side and the other one close to the pressure side.
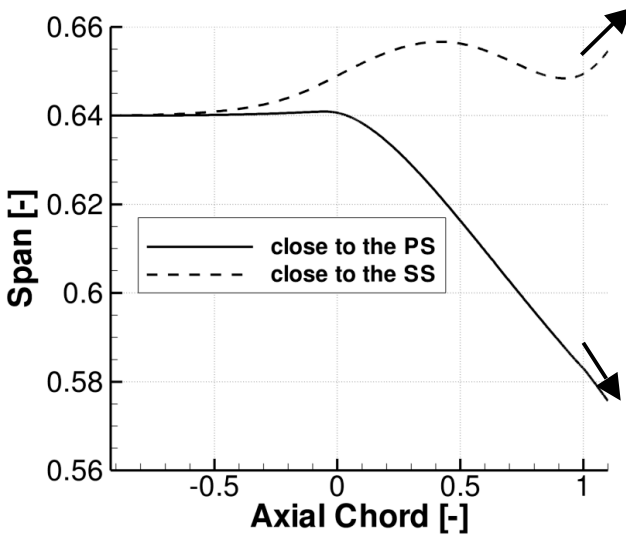
Figure 5.22 The change in the radial positions of the streamlines passing close to the two sides of the stator blade

Figure 5.22 shows the radial coordinates of these streamlines along the axial distance where the leading and trailing edges of the stator are positioned along the horizontal axis at 0 and 1 respectively. As shown, they both start at the same radial positions upstream of the stator. As they move downstream of the passage their radial positions start to diverge. The streamline at the pressure side shows a continuous downward trend whereas the other one at the suction side exhibits an upward trend in the radial direction. When both of these streamlines leave the stator passage there is a

difference in their radial positions of about 9 % of the blade span where the streamline at the suction side ends up at a higher radial position compared to the one at the pressure side. As shown, with the particle tracking study and also with the streamlines there is a spanwise transport mechanism pointing in opposite directions at each side of the stator blade. At the suction side there is an upward flow towards the tip, on the other hand at the pressure side the gas experiences a downward flow towards the hub endwall.

So far, it has been discussed that the spanwise migration pattern inside the stator passage is effective in the migration of the particles to the tip leakage flow. However, there is a still circumferentially non-uniform distribution pattern even at the stator exit as shown in Figure 5.21. The particles at the suction side could migrate to the rotor blade tip even though they were at lower spanwise positions at the suction side compared to the particles at the pressure side of the blade. This still remaining non-uniformity in the distribution of the particles indicates another aspect of the flow that is not considered so far. In that regard, the pitch angle distribution at the stator exit will be considered. In Figure 5.21 the calculated time averaged pitch angle distribution downstream of the stator was shown in the background. As shown, the flow has a positive pitch angle distribution (pointing to the tip endwall) close to the suction side and a negative pitch angle distribution (pointing to the hub endwall) at the pressure side. The footprint of the stator wake could also be seen with a negative pitch angle distribution. The radial pressure gradient due to radial equilibrium condition forces the wake to migrate towards the hub because of its velocity deficit. In summary, the opposite behavior in the spanwise migration patterns on the sides of the stator also exists in the pitch angle distribution. At the suction side the gas migrates into the rotor passage with a positive pitch angle on the other hand, at the pressure side the flow points to the hub endwall. This pattern in the pitch angle distribution could also be seen in the trend of the streamlines at the stator exit as shown previously in Figure 5.22.
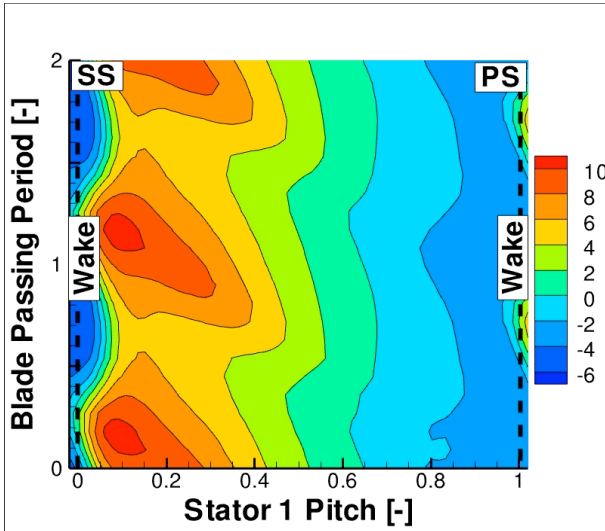
Figure 5.23 The time evolution of the calculated pitch angle at midspan at the stator exit

Next, the evolution of the pitch angle distribution downstream of the stator will be investigated both in time and in space with the aid of the space-time diagrams. The way they are plotted in this study is as follows. The horizontal axis shows the distribution of the pitch angle along the arc across the stator passage at midspan and the temporal change in the pitch angle at each circumferential position is plotted in the vertical direction. With these specifications the space-time diagram of the numerically predicted pitch angle distribution downstream of the stator is shown in Figure 5.23. In this diagram the sides of the blade are marked with vertical dashed lines bordering the wake of the stator which is visible with a negative pitch angle distribution. Looking in vertical direction there is a variation of the pitch angle in time. The inclination of iso-pitch angle lines in the diagram is due to the rotation of the rotor blade. In the time frame of two rotor blade passings the pitch angle distribution in the middle of the passage showed two peaks and two troughs. So the variation of the pitch angle is periodic with the rotor blade passing frequency. Moreover, except this periodic pattern in time there is also a change in the pitch angle distribution in space shown along the horizontal axis. Moving towards the pressure side the pitch

angle distribution becomes negative. On the other hand, at the suction side the pitch angle turns into positive. Even though the pitch angles vary in time due to the rotor potential field their signs are constant in time close to the sides of the blade.
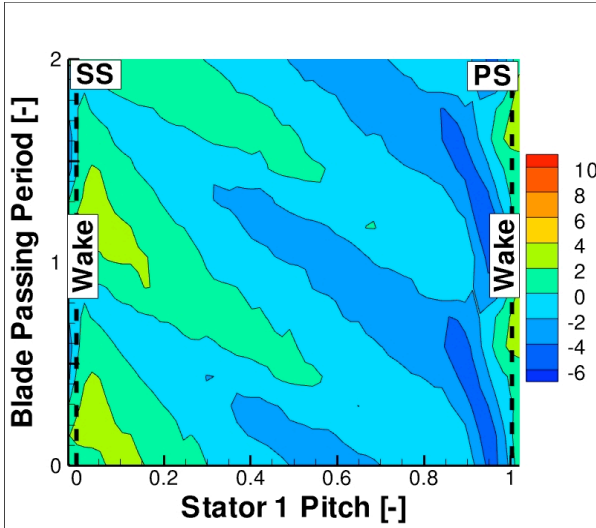
Figure 5.24 The time evolution of the measured pitch angle at midspan at the stator exit

To ensure the validity of the numerical results in terms of the stator aerodynamics, the numerically predicted pitch angle distribution downstream of the stator blade is compared with the time-resolved aerodynamic measurements conducted downstream of the stator (plane B). Figure 5.24 shows the space-time diagram of the experimentally measured pitch angle distribution downstream of the stator. Comparing the measured space-time diagram with the numerically predicted one, a qualitative match between the two can be observed. As in the numerical predictions there is a change in the pitch angle of the flow from positive at the suction side to negative at the pressure side of the stator. However, the measurements show a weaker variation across the passage compared to the predictions. So in space the predictions match with the measurements in terms of the trend,

but the magnitudes are predicted higher compared to what has been measured. In terms of the time evaluation of the pitch angle the measurements also confirm the effect of the rotor potential field which can be observed in the inclination of the iso-pitch angle lines.

5.6.   Hot Streak – Stator Clocking

Up to now the hot streak migration pattern in the turbine has been carefully investigated with the aid of the unsteady particle tracking analysis and complementary simulations. The flow physics behind the observed pattern in the migration of the hot streak has also been investigated in great detail. To benefit out of what has been learnt so far, the hot streak at the turbine inlet will be shaped in a way that makes use of the inherent flow patterns inside the turbine and reduce the heat load on the rotor blade tip. For that purpose a hot streak-stator clocking study will be carried out that will be based on the circumferential non-uniformity in the spanwise migration pattern within the turbine.   According to the distribution pattern of the particles at the turbine inlet as shown in Figure 5.14, the hot streak is clocked towards the pressure side of the stator 1 and the resulting effect on the incident heat load on the rotor blade will be investigated. The hot streak used for the particle tracking study is used as a baseline in this study. In addition to the baseline case three clocking positions towards the pressure side and one clocking position towards the suction side of the stator are considered. In this study the shifts towards the pressure side are taken as positive and the shifts towards the suction side as negative. The clocking angles used are 2%, 6% and 10% of the stator pitch towards the pressure side and -6% of the stator pitch towards the suction side. The clocking towards the suction side will be used to test the validity of the flow pattern shown by the particle tracking code. The total temperature distributions at the inlet plane are shown in Figure 5.25. Since the hot streaks are only moved in circumferential direction all the cases have the same circumferentially mass averaged temperature profiles at the turbine inlet which means that the heat added to the flow at each spanwise position is the same for all the cases.
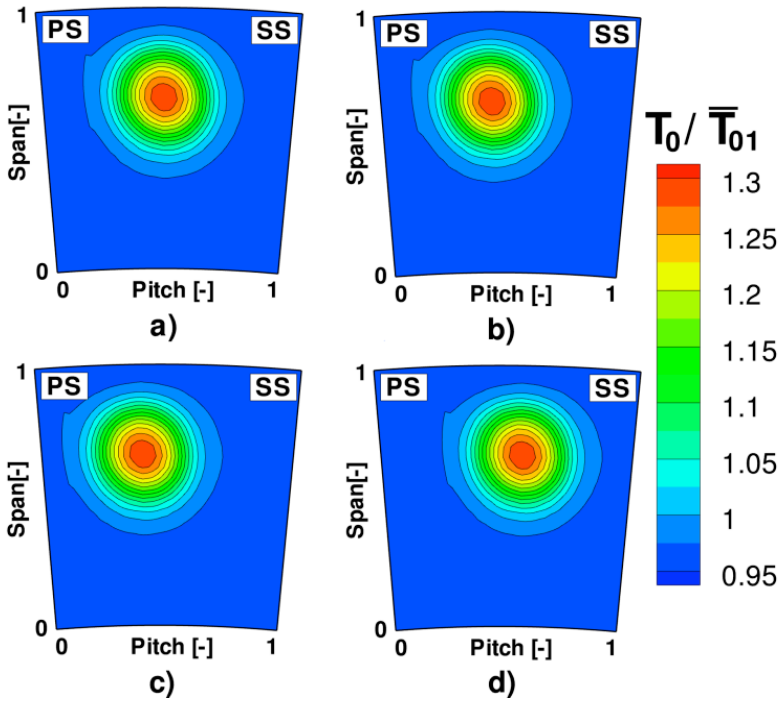
Figure 5.25 The total temperature inlet boundary conditions used in the hot streak clocking study a) circular hot streak clocked towards the PS of the stator by 2 % of the stator pitch, b) circular hot streak clocked towards the PS of the stator by 6 % of the stator pitch, c) circular hot streak clocked towards the PS of the stator by 10 % of the stator pitch, d) circular hot streak clocked towards the SS of the stator by 6 % of the stator pitch

The circumferentially mass averaged total temperature distributions of three of the hot streak shapes are shown in Figure 5.26. There are minor differences in the temperature profiles between the clocking positions due to the non-uniformity in the mass flow distribution at the inlet plane of the stator. However, the differences are of the order of 0.02%, which is quite small to be considered for this study. As shown, the spanwise position of the temperature peak is raised to about 65% which was at about 50% span in the experiment as shown in Figure 3.5. The rise in the spanwise position

of the hot streak is to enhance its migration to the rotor blade tip since no considerable migration was observed in the measurements. Moreover, having the spanwise position of the peak temperature above midspan is usual in real engines [8].
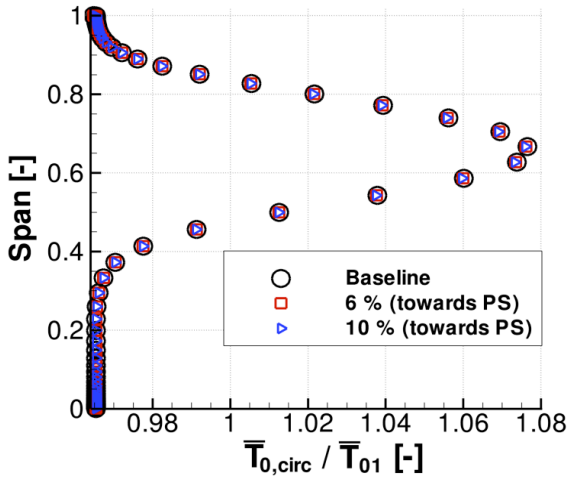
Figure 5.26 The circumferentially mass averaged total temperature profiles at the turbine inlet for the baseline and two of the clocked (towards the stator pressure side) hot streak cases

5.6.1. Effect of Hot Streak – Stator Clocking on Mixing within the Stator

To investigate the effect of the opposite spanwise transport directions inside the stator on the temperature field downstream of the stator the circumferentially mass averaged temperature distribution at the stator-rotor interface has been investigated. As shown previously in Figure 5.26, the circumferentially mass averaged temperature profiles upstream of the stator were the same for all the clocking positions.
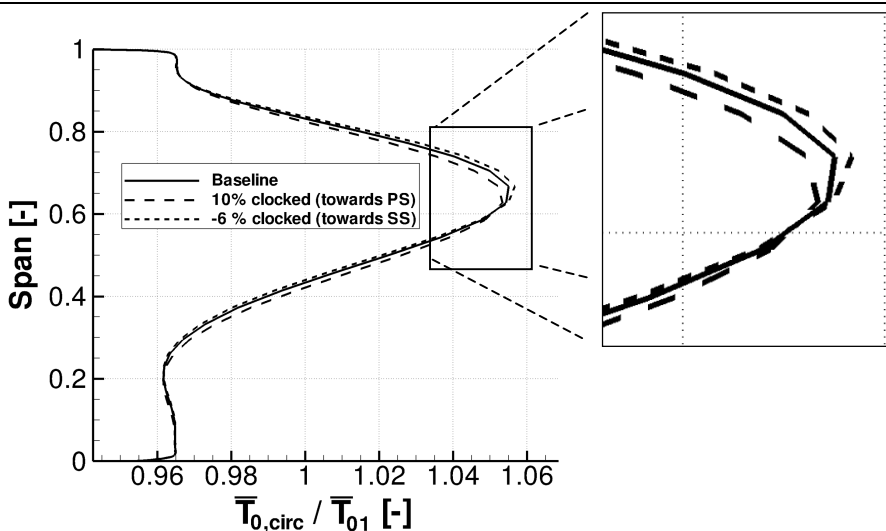
Figure 5.27 The circumferentially mass averaged temperature profiles downstream of the stator for the baseline and two of the clocked hot streak cases

In Figure 5.27 the same distribution downstream of the stator has been plotted for the baseline and for two other clocking positions. At this plane a considerable difference between the total temperature profiles has been observed. The 10% clocked hot streak has its peak at a 2% lower spanwise position compared to the baseline and the -6% clocked hot streak has its peak at a higher spanwise position compared to the baseline. These differences in the spanwise positions of the peaks are due to the opposite spanwise flow patterns at the two sides of the stator blade. In addition to the difference in the positions of the peaks there are also small differences in the peak temperature levels due to the clocking. The reduction in the peak temperature indicates a higher radial spread of the hot streak due to the fact that the mass averaged total temperature has to be conserved in stationary blade rows assuming adiabatic wall boundary conditions. Having a lower peak temperature for the 10% clocking position indicates a relatively high radial spread of the hot fluid at the pressure side. The reduction in the peak temperature level is about 0.2% of the average turbine inlet temperature

level that would correspond to 4K in real engine conditions. On the other hand, clocking the hot streak towards the suction side led to a more peaked profile downstream of the stator which shows a lower spread of the hot streak in the radial direction. To summarize, close to the stator pressure side there is a higher radial mixing and also the flow pitches towards the hub. On the other hand, opposite to the behavior at the pressure side the radial mixing is reduced at the stator suction side and the flow pitches towards the shroud increasing the spanwise position of the peak temperature region. The present numerical study showed a consistency with the numerical work of An et. al. [17] in terms of the presence of these effects and also in terms of their behaviors on the sides of the stator. Among these two effects influencing the spanwise heat load distribution on the downstream rows, the small differences in the peak temperatures show that the radial mixing has a rather secondary effect on the spanwise heat load distribution compared to the change in the position of the peaks.

Table 5.3 Behavior of the stator aerodynamics on the evolution of the hot streak

	Suction Side	Pressure Side
Radial profile shape	Peaked	Less peaked (more flat)
Spanwise position of the peak	Increases	Decreases

As a conclusion of the observations made in the particle tracking study and later on in the hot streak clocking study a conceptual mixing model has been developed that reflects the effect of the stator aerodynamics on the two important aspects of the hot streaks downstream of the stator. One of these aspects is the shape of the radial profile. Migrating close to the pressure side the hot streak elongates in radial direction and the peaked radial temperature profile at the turbine inlet gets flat downstream of the stator. On the other hand, at the suction side the hot streak is diffused in circumferential direction which orients the hot streak at about the midspan and prevents its radial elongation. Due to the constrained radial diffusion of the hot streak at the suction side the profile becomes more peaked

compared to the pressure side. Secondly, the radial position of the peak temperature is another important aspect to consider. As observed in Figure 5.22 at the pressure side there is a migration pattern directed towards the hub endwall. Accordingly, the hot streak's peak migrates towards the hub endwall at the pressure side. On the other hand, when the hot streak migrates close to the suction side the hot streak migrates towards the shroud leading its peak being positioned at a higher radial position compared to the turbine inlet. The behavior of the stator aerodynamics on the aspects of the hot streak discussed is summarized in Table 5.3.

5.6.2. Effect of Hot Streak – Stator Clocking on Rotor Blade Heat Load

The differences in the time averaged adiabatic wall temperatures of the rotor blade between each clocking position and the baseline case are shown in Figure 5.28. The regions with negative or positive values indicate a decrease or an increase in the adiabatic wall temperature levels with respect to the baseline case respectively. As shown, clocking of the hot streak leads to a heat load distribution in the rotor row in the spanwise direction. Clocking towards the stator pressure side decreases the adiabatic wall temperature at the rotor blade tip and increases it at lower spanwise positions. The more the hot streak is clocked towards the pressure side the larger is the area of temperature reduction at the blade tip. Moreover, as shown in Figure 5.29 the adiabatic wall temperature levels along the camberline at the rotor blade tip are reduced with increasing clocking angles starting from 25% axial chord. The maximum temperature reduction along the camber line is observed at the trailing edge and will be about 24 K for the 10% clocking position scaling up the mean total temperature at the stator inlet to realistic engine conditions (assuming a mean turbine entry total temperature level of 2000 K). The relatively small increase in the adiabatic wall temperatures towards the hub end wall and close to the trailing edge as shown in the subfigures a, b, and c in Figure 5.28 is due to the effect of the stator on the spanwise transport in both of the blade rows. Clocking the hot streak towards the pressure side the hot streak is diverted towards the hub endwall which results in an increase in the adiabatic wall

temperature close to the hub endwall as shown most obviously in Figure 5.28c.
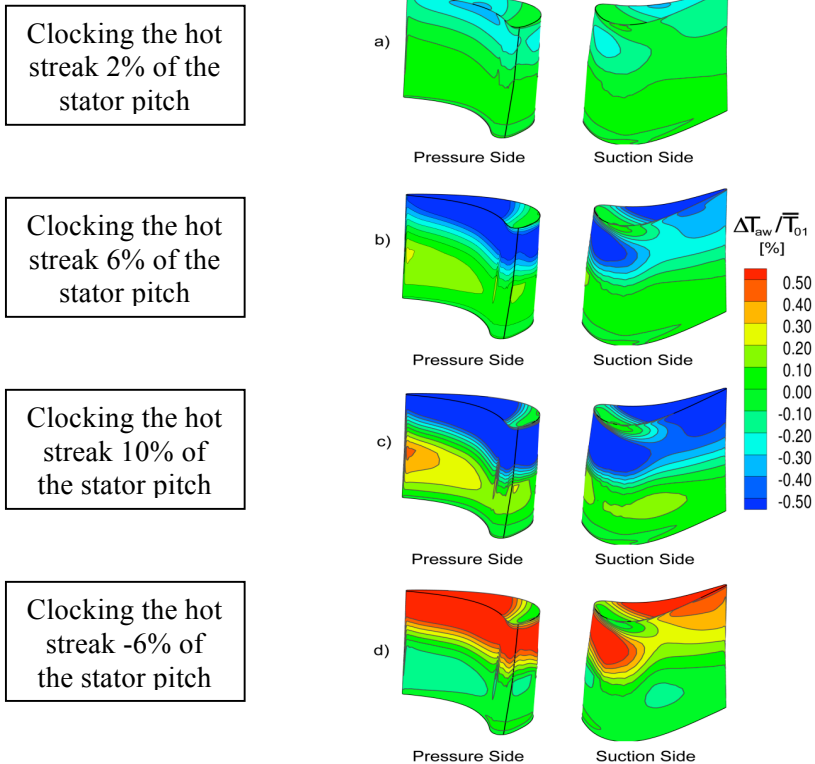
Figure 5.28 The differences in the calculated, time averaged adiabatic wall temperatures of the rotor blade imposed to hot streaks with different clocking positions shown in Figure 5.25 ($\Delta T_{aw} = T_{aw,clocked} - T_{aw,baseline}$)

5.7. Discussion - Impact on the Combustor Design

In this chapter the hot streak migration pattern to the rotor blade tip is analyzed via the unsteady particle tracking tool and the effect of the stator aerodynamics and the hot streak inherent secondary flows on the observed

migration pattern is discussed. The fuel injector – stator clocking study is proposed to modify the circumferential temperature distribution at the turbine inlet in favor of the rotor blade tip heat load. Using a circular hot streak which has the same temperature gradients in all directions (spanwise and circumferential) a very big sensitivity of the rotor tip heat load on the clocking position of the hot streak was observed. Even clocking the hot streak by 10% of the stator pitch, reductions of about 24K in rotor tip adiabatic wall temperatures could be observed in real engine conditions which is quite substantial effect. [1] In this work the blade itself was not modeled as it is done in a conjugate heat transfer study, so the effect of the hot streak clocking on the real blade wall temperature could not be evaluated. However, changing the adiabatic wall temperature level, the main driving force of heat transfer, by more than 20 K is expected to increase the component life time considerably or reduce the cooling requirement which would increase the cycle efficiency of the turbine.

Now, the realizability of this approach in real combustors will be discussed. One very big disadvantage of the fuel injector – stator clocking is that their number ratio has to be an integer. Otherwise the clocking approach which is also discussed in the literature could not be practically applied in real engines. The second issue is the level of circumferential temperature non-uniformity downstream of the combustor. In can-annular combustors where the fuel injectors are placed in separate liners, hot streak shapes with relatively high circumferential temperature gradients could be observed. So it is expected that in this kind of combustors the fuel injector – stator clocking approach to be highly effective in distributing the heat loads between the downstream rows. However, in more modern full annular combustor due to the reduced circumferential temperature non-uniformities the effectiveness of this approach would possibly be reduced.
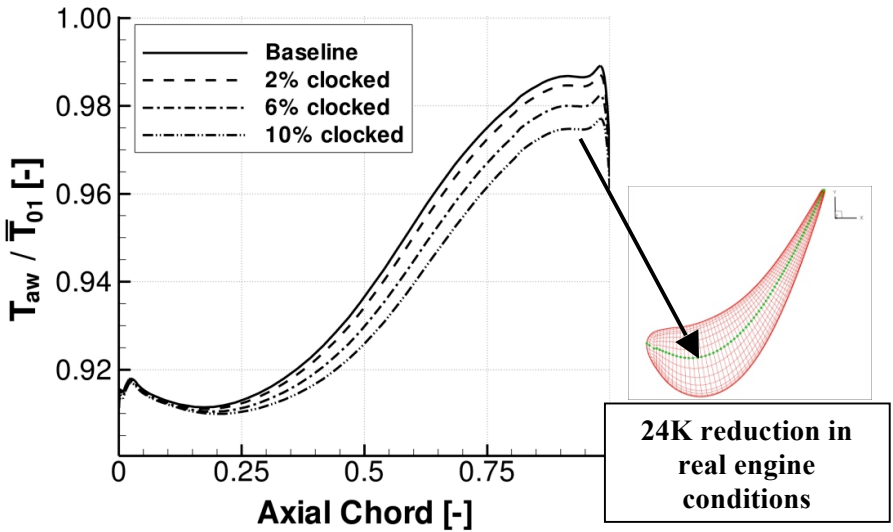
Figure 5.29 The time averaged, calculated adiabatic wall temperatures along the camberline of the rotor blade imposed to hot streaks with different clocking positions shown in Figure 5.25

6. Hot Streak Migration in HP Turbine with Non-axisymmetric Endwalls

In the previous chapter the hot streak migration pattern within the stage has been investigated in detail with the aid of the unsteady simulations and an unsteady particle tracking analysis. The lessons learned about the flow patterns affecting the hot streak migration are used in transforming the temperature profile at the turbine inlet to reduce the incident heat load on the rotor blade tip. In the last chapter this has been achieved by varying the circumferential position of the hot spot at the turbine inlet with respect to the stator blade. The so called fuel injector – stator clocking method has been considered before in the literature [2] [16] [17] as a simple and practical way of distributing the heat load between the blade rows. Different from the previous work the same method has been investigated in the last chapter in terms of its effect on the rotor blade tip heat load.

Although the fuel injector – stator clocking has been considered in the literature both in the numerical [16] and in the experimental studies [2], it has a serious limitation; requiring the number of the fuel injectors and the number of the stator blades have to have an integer ratio. Secondly, the developments in the combustor technology to ensure a low NOx operation character resulted in a more uniform temperature distribution at the turbine inlet. For the combustors with reduced circumferential temperature variation at midspan the benefits of the fuel injector – stator clocking are possibly considerably reduced as well.

The increased temperature uniformity in the circumferential direction is also observed to some extent in the radial direction. The flattening of the radial temperature profiles at the turbine inlet increased the incident heat load on the endwalls and on the rotor blade tip as well. Recent data from the open literature shown in Chapter 1 obtained from the numerical tools confirms the trends in the combustor outlet temperature distribution. To

model the observed temperature distributions downstream of the real combustors a non-symmetric hot streak shape has been experimentally generated which will be considered in this part of the numerical study. The generated hot streak has different spanwise extents on its sides along the spanwise direction. Compared to the circular hot streak considered before, this form of the hot streak reduced the circumferential temperature gradients at the midspan but kept them close to the endwalls as it was observed in Chapter 1. Measurements have been conducted in LEC's axial turbine facility "LISA" using the in-house "FENT" probe technology which delivers time resolved pressure and velocity data alongside of the unsteady temperature field. The experimental data is utilized to validate the numerical simulations conducted using the inlet boundary conditions taken from the measurements. Different from the turbine geometry used in the previous chapter, in this study the first stator is equipped with non-axisymmetric endwall profiling. This design feature is increasingly becoming a more common design feature in modern turbines due to its effectiveness in reducing secondary losses [20]. However, it is expected that the non-axisymmetry at the endwalls will have an additional effect on the spanwise migration pattern within the stator passage which will be analyzed with the aid of the unsteady particle tracking study. Making use of the resulting turbine inherent migration characteristics, the circumferential temperature variations at the endwalls are shaped in the numerical study that would reduce the incident heat load on the rotor blade tip. The modifications required on the combustor side in terms of the realizability of the considered hot streak shapes will be handled in the last portion of this chapter.

6.1.   Turbine Geometry & Numerical Model

In this study the "LISA-M1" case turbine geometry has been used. This turbine geometry is composed of one-and-a-half stages and except the design of the first stator the rotor and the second stator share the same designs with the ones used in the "LISA-D" case geometry used in the previous study in Chapter 1. In this turbine geometry the first stator is equipped with non-axisymmetric endwalls whereas the other two rows have conventional axisymmetric endwalls. The first stator has the same blade geometry as the first stator of the "LISA-D" case turbine but differs only in

the shape of the endwalls. Information about the design of the non-axisymmetric endwalls is given by Germain et. al. [21] and very detailed flow field measurements have been carried out by Schuepbach et. al. [20] revealing the effect of the endwall profiling on the flow field and secondary losses generated.

The computational mesh has been generated with the in-house multi-block mesh generator "MEHSBOUND" [41]. The stator and rotor passages have been meshed separately. The tip clearance gap is also included in the rotor mesh. The separately meshed rows are merged afterwards in a multi-pitch and multi-row arrangement. The non-axisymmetric endwall shapes have been added to both endwalls of the stator 1. The wall mesh of the computational model is shown in Figure 5.1. The overall mesh consists of about 3.2 million nodes and the y+ values at the wall correspond to the levels shown in for the fine mesh.
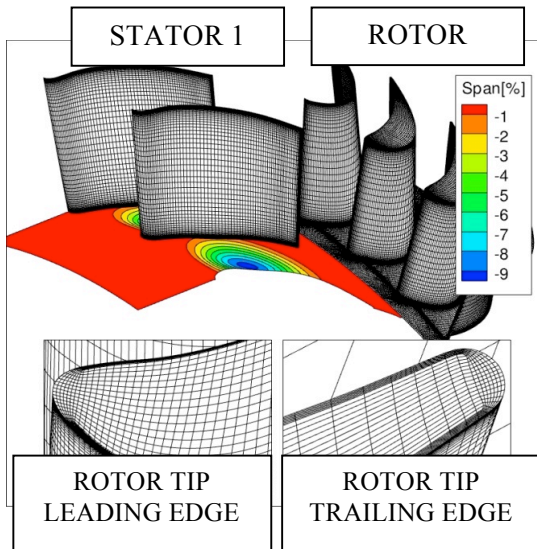
Figure 6.1 The wall mesh with the non-axisymmetric endwall profiling applied on the stator

6.2.   Analysis of the Hot Streak Migration Pattern in the Turbine

In a similar reasoning as in Chapter 1 the hot streak migration pattern to the rotor blade tip has been investigated with the unsteady particle tracking tool which runs on time resolved simulation data. In order to reveal the effect of the endwall profiling on the migration pattern within the stage the particle tracking study have also been conducted for the "LISA-D" case geometry with the axisymmetric endwalls at the stator 1. The inlet boundary conditions have been taken from the measurements conducted upstream of the turbine shown in Section 4.6.5. As in the previous study, adiabatic, no-slip wall boundary conditions are imposed at the walls and the information between the rows has been transferred via the sliding interface technique. At the outlet of the domain the static pressure is set at the hub and radial equilibrium condition is imposed to calculate the pressure level at higher spanwise positions. The validation of the numerical model has been covered in Section 4.6.5.

6.2.1. Boundary Conditions and Settings for the Particle Tracking Study

The settings used for the particle tracking study are very similar to the one used in Section 5.3.1. Here, they will be mentioned only briefly. More detailed information about the specifications of the particle tracking study can be found in 5.3. For this study 2400 particles are continuously released from turbine inlet at different time steps. These particles are uniformly distributed upstream of the stator blade spanning an area of 20% of the blade span and 1.3 times the blade pitch. This distribution corresponds to roughly 4 particles per cell. Every time step a new set of particles has been released from the turbine inlet. For the time resolution used this makes in total 33 sets within one rotor blade passing period. This way the migration pattern covering all the possible relative positions between the stator and the rotor will be considered. Figure 6.2 shows a snapshot in time while all the 80,000 particles were migrating through the turbine stage. After all the sets of particles have been convected through the turbine, the ones which

migrate to the rotor blade tip within each set of particles have been detected and their initial positions at the turbine inlet are shown.

6.2.2. Observations on the Hot Streak Migration Pattern to the Rotor Blade Tip

Figure 6.3 shows the initial positions of the particles released upstream of the stator with non-axisymmetric endwalls within a time frame of one rotor blade passing and finally migrate to the rotor blade tip.
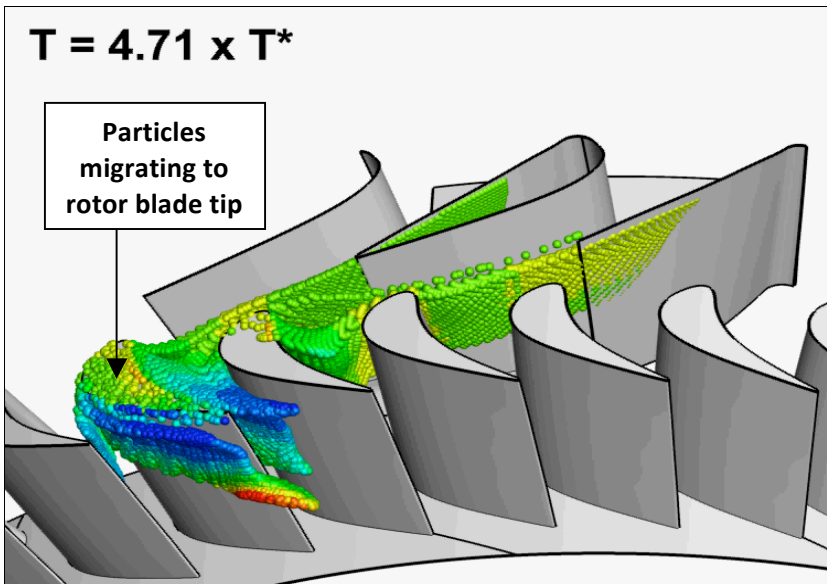
Figure 6.2 A snapshot in time showing the positions and local absolute total temperature levels of the particles released in different instants in time upstream of the stator (T* = time required for the rotor to rotate one rotor pitch)

Major similarities exist between this distribution pattern and the one shown in Figure 5.14. Also here a circumferential non-uniformity in the distribution pattern of the particles is observed. Particles closer to the suction side of the stator blade can migrate to the rotor blade tip even though they have been released at lower spanwise positions at the inlet plane compared to the particles close to the pressure side. Compared to the distribution shown in Figure 5.14 in the previous chapter a stronger circumferential non-uniformity is observed which might be due to the non-symmetric hot streak shape or due to the effect of the non-axisymmetric endwall profiling.
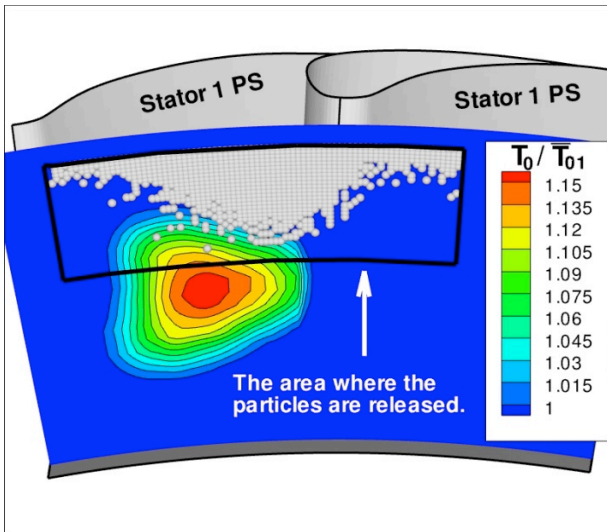
Figure 6.3 The distribution of the particles migrating to the rotor blade tip among all the particles released within a time frame of one rotor blade passing upstream of the stator with non-axisymmetric endwall profiling

6.2.3. Spanwise Migration Pattern inside the Stator Passage

In order to investigate the effect of the stator aerodynamics on this migration pattern, the distribution of the same particles shown in Figure 6.3

is next examined at the stator outlet plane in Figure 6.4. The particles are colored according to the change in their spanwise positions relative to their radii at their initial positions at the stator inlet plane. A positive change in the spanwise position indicates a migration of the particle towards the tip endwall. On the other hand, a negative change indicates a migration towards the hub endwall. It is evident from the pattern seen in Figure 6.4 that particles closer to the suction side of the stator have experienced a positive radial flow reaching up to 4% of the stator span. On the other hand, particles closer to the stator pressure side had an opposite radial flow reaching of up to -4% of the blade span.
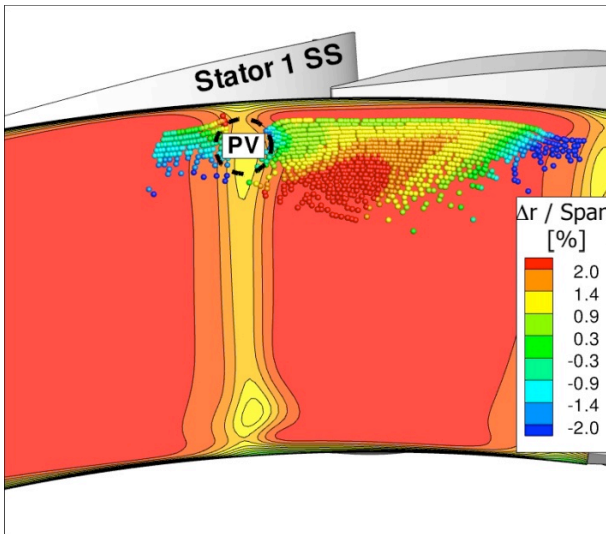
Figure 6.4 The numerically predicted time averaged absolute total pressure distribution in the background and the distribution of the particles shown in Figure 6.3 downstream of the stator – the particles are colored according to the change in their spanwise position within the stator

The circumferentially increased uniformity in the distribution of the particles especially close to the suction side compared to the distribution at

the stator inlet plane shown in Figure 6.3 reveals the importance of the spanwise migration patterns inside the stator on the hot streak migration pattern. The still existing non-uniformity indicates other aspects of the flow that are not uniform in circumferential direction such as the pitch angle distribution which was discussed in Section 5.5.

6.2.4. Effect of the Endwall Profiling on the Migration Pattern

In order to evaluate the effect of the non-axisymmetric endwalls in the migration pattern, the particle tracking study has been repeated using the stator with axisymmetric endwalls. Figure 6.5 shows the initial positions of the particles migrating to the rotor blade tip among all the ones released upstream of the stator with axisymmetric endwalls within a time frame of one rotor blade passing. As shown, only very minor differences are observed between this distribution pattern and the one shown in Figure 6.3. In order to evaluate the differences easily the number of particles migrating to the rotor blade tip from each circumferential position has been plotted for both cases in Figure 6.6. The leading edges of the stator blades are shown with the dashed lines and the pressure and suction sides are located on the right and left hand sides of the leading edges respectively. As shown, the peak in the graph is shifted towards the suction side, which shows that mainly particles close to the suction side of the stator blade migrate to the rotor tip. The two distributions have similar patterns along the stator pitch except in the vicinity of the pressure side where the number of the particles is higher for the case with non-axisymmetric endwalls than it is with axisymmetric endwalls. The fact that the two distributions only differ at the pressure side indicates that the circumferential non-uniformity in the distribution pattern is weakened by the effect of the non-axisymmetric endwall profiling.

To investigate the effect of the non-axisymmetric endwall profiling on the streamline pattern inside the stator, streamlines are released at 90% span where the effect of the endwall profiling is expected to be more pronounced. In Figure 6.7, the radial positions of two streamlines released at 90% span from each side of the stators (both with and without endwall profiling) have been plotted with respect to the axial distance from the inlet

of the domain. In the stator with axisymmetric endwalls, the streamline close to the suction side shows increase and decrease in its spanwise position depending on its axial position. However, in total the streamline ends up at a higher spanwise position downstream of the stator relative to its position at the stator inlet, whereas the streamline close to the pressure side shows a continuous drop in its spanwise position. So there is a considerable difference in the spanwise positions of the streamlines at their endpoints downstream of the stator even though they have started from the same spanwise position upstream of the stator.
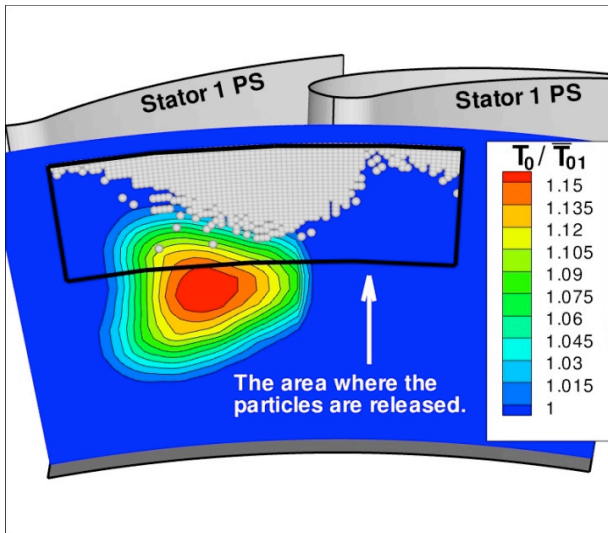
Figure 6.5 The distribution of the particles migrating to the rotor blade tip among all the particles released within a time frame of one rotor blade passing upstream of the stator with conventional axisymmetric endwalls

On the other hand, inside the stator with non-axisymmetric endwalls, both of the streamlines released from each side of the stator show first a radial migration towards the tip and then move towards the hub. There is also a difference in the spanwise positions of the streamlines at their endpoints downstream of the stator but not as much as the difference in the radial positions of the streamlines inside the stator with axisymmetric endwalls.

This clearly shows the effect of the endwall profiling unifying the opposite spanwise migration patterns observed at the sides of the stator. Because of this reason more particles released from the pressure side of the stator with non-axisymmetric endwall profiling could have migrated to the rotor blade tip. However, the endwall profiling also affects the whole aerodynamics of the stator including the loading of the profiles. Introducing the profiles at the endwalls makes the stator more aft-loaded and the loading in the front of the airfoil is considerable reduced [21]. The difference in the migration pattern between the two stators might also be related to the change in the loading behavior of the blade.
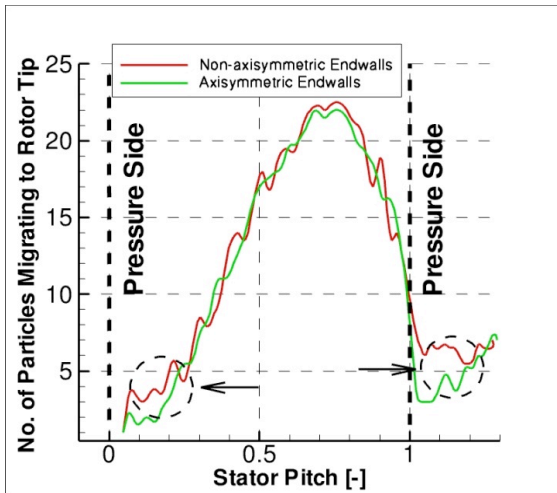
Figure 6.6 Number of particles migrating to the rotor blade tip released upstream of the stators with and without non-axisymmetric endwall profiling
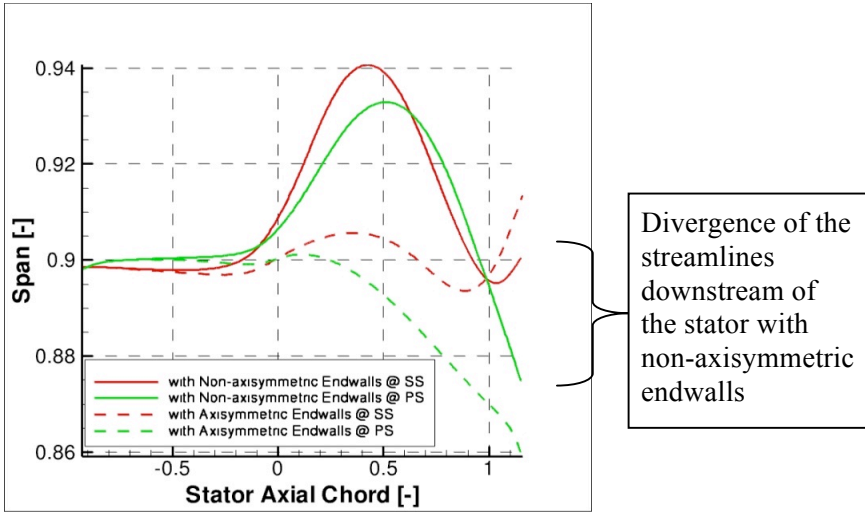
Figure 6.7 The change in the radial positions of the streamlines released close to the pressure and suction sides of the stator with and without endwall profiling

6.3. Effect of Hot Streak Shape on Rotor Blade Heat Load

In the previous sub-chapters the flow pattern to the rotor blade tip has been in detail analyzed and the effect of the endwall profiling on this pattern is discussed. Non-symmetric hot streak shape was motivated to model the circumferential temperature non-uniformities observed close to the endwalls in the combustor data shown in 1. Adjusting an hot streak shape that has its spanwise larger edge impinged on the stator's pressure side was to minimize the hot streak convection to the rotor blade tip according to the migration pattern observed. In this part the implications of the circumferential non-uniformity in the migration pattern on the incident heat load on the rotor blade tip will be analyzed. In that regard the same hot streak shape imposed at the turbine inlet is rotated around its axis such that its spanwise longer side positioned at the stator suction side. Conducting unsteady simulations with both of these inlet boundary conditions, the

change in the rotor blade heat load can be derived using the differences in the adiabatic wall temperatures.

The inlet total temperature distributions used in this study are shown in Figure 6.8. For this study the experimentally measured hot streak shape is taken as the baseline case which had its longer extent at the stator pressure side. Based on the migration pattern analysis it is expected that this hot streak shape is favorable in terms of rotor blade tip heat load. For this study the spanwise positions of the temperature peaks have been raised to about 60% span. With that, the effect of the hot streak shaping will be more pronounced on the rotor tip heat load and also it is more common in real engines to have the temperature peak slightly above the midspan since mechanical stresses increase towards the hub of the rotor blade. Since the two temperature inlet boundary conditions can be simply generated by rotating each shape, the circumferentially mass averaged total temperature profiles are the same for both of the cases meaning that the heat addition to the flow at each spanwise position is kept unchanged. The circumferentially averaged total temperature profiles are given in Figure 6.9. Additionally, a uniform total pressure distribution with axial inflow conditions have been imposed at the turbine inlet. Since k-ω turbulence model is used in this study turbulence intensity has to be also imposed as an inlet boundary condition which is set to 10% for both of the cases. This value is a reasonable estimate for the incoming turbulence intensity level at the turbine inlet in real engines. The calculations are conducted for two different uniform turbulent length scale values; the large being 2mm and the small 0.01mm. The 2mm turbulent length scale leads to the eddy viscosity levels in excess of 1000 times of the laminar viscosity levels which leads to considerable diffusion of the hot streaks within the stator. On the other hand, the low turbulent length scale results in eddy viscosity levels around 5 times the laminar viscosity level. Adiabatic, no-slip boundary conditions have been set at the solid walls and a sliding mesh approach has been used to transfer both the flow and turbulence quantities between the blade rows. The time resolved simulations are conducted with these boundary conditions and the time averaged adiabatic wall temperatures on the rotor blade is derived as an indicative of the incident heat load on the rotor blade. Any difference in the adiabatic wall temperature levels between these different scenarios will be related only to the difference in the inlet total temperature boundary conditions.
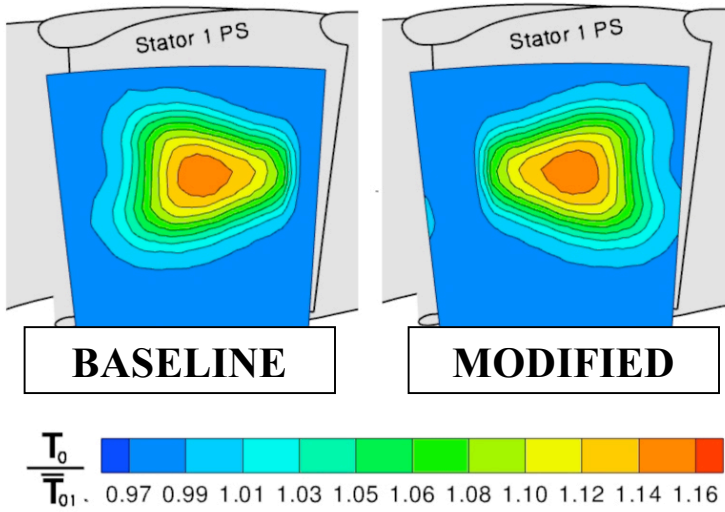
Figure 6.8 The total temperature distributions at the turbine inlet used in the numerical study
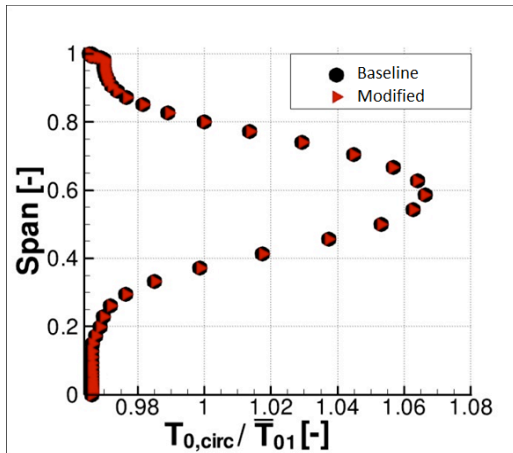
Figure 6.9 The circumferentially mass averaged total temperature profiles for both hot streak shapes

6.3.1. Change in the Rotor Blade Adiabatic Wall Temperatures

Time resolved, multi-row simulations for the two cases mentioned above yielded solutions from which time averaged, adiabatic wall temperatures on the rotor blades can be determined. The two hot streak shapes resulted in different level of heat loads on the rotor blade which will be evaluated in terms of the difference in the adiabatic wall temperature levels. Figure 6.10 shows the percentage difference in the adiabatic wall temperatures on the rotor blade resulted by exchanging the two hot streak shapes upstream of the stator with endwall profiling. The reduction in the adiabatic wall temperature level on a particular location of the rotor blade indicates that the local incident heat load is lower with the baseline hot streak shape than with the modified one. On the contrary, an increase in the temperature level points out a higher local heat load with the baseline hot streak shape. A 0.5% change in the temperature level would correspond to a 10 K change in the adiabatic wall temperatures under real engine conditions, with a mean turbine inlet temperature of 2000 K. First the results with the small turbulence length scale at the turbine inlet will be discussed.

On the rotor pressure side at the midspan there is a zone of temperature reduction extending like a band from the leading edge to the trailing edge. At this region a reduction in the adiabatic wall temperature levels is observed with the baseline hot streak. The reduction at the midspan can be explained via the conceptual radial mixing model covered in Section 5.6.1. According to this model, the radial temperature profile downstream of the stator becomes more flat if the hot streak impinges on the pressure side of the stator blade. On the other hand, impinging the hot streak on the stator suction side leads to more peaked radial temperature profiles downstream of the stator. Accordingly, the baseline hot streak shape led to a reduced temperature level at the rotor midspan and to elevated temperature levels towards the endwalls which can also be observed in Figure 6.10. A similar pattern in the change of the adiabatic temperature distribution is observed at the suction side of the rotor blade. However, compared to the pattern at the pressure side the regions with the elevated temperature are more compressed towards the midspan of the rotor blade at the suction side. At the rotor blade tip at about 50% axial chord considerable reduction in the

adiabatic wall temperatures could be observed. However, towards the trailing edge the drop in the temperature level reduces and even a zone with increased temperature levels is found at the trailing edge close to the pressure side of the blade. This portion of the rotor blade has a small thickness and manufacturing of the internal cooling channels at this region of the blade is challenging. Therefore the increase in the heat load level at this portion of the blade can be prohibitive.
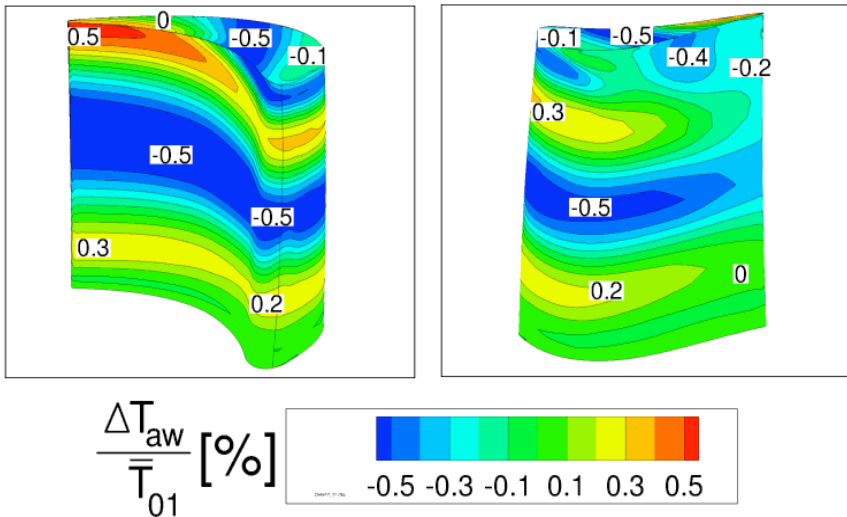
Figure 6.10 Difference in the rotor blade adiabatic wall temperatures between the two hot streak shapes imposed upstream of the stator with non-axisymmetric endwall profiling (ΔTaw = Taw,baseline - Taw,modified) with low turbulent length scale level at the turbine inlet
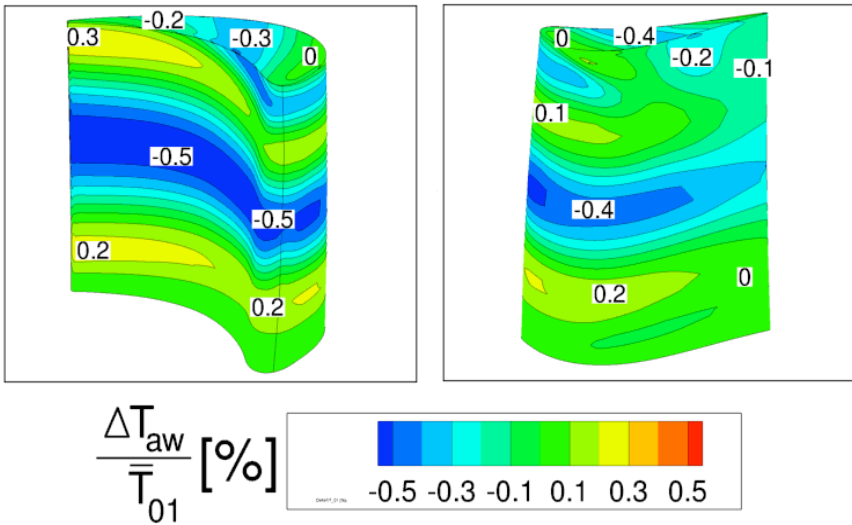
Figure 6.11 Difference in the rotor blade adiabatic wall temperatures between the two hot streak shapes imposed upstream of the stator with non-axisymmetric endwall profiling (ΔTaw = Taw,baseline - Taw,modified) with high turbulent length scale level at the turbine inlet

Figure 6.11 shows the change in the adiabatic wall temperature levels on the rotor blade positioned downstream of the stator with non-axisymmetric endwall profiling and imposed to the high turbulent length scale levels at the turbine inlet. As shown, increasing the turbulent length scale lowers the intensity of the temperature rise close to the rotor tip at the pressure side. In a consistent manner the intensity of the zones with the temperature drop is also decreased. The elevated turbulence by increasing the length scale level at the turbine inlet increases the mixing and reduces the temperature gradients. In Figure 6.12 the effect of the turbulent length scale on the change in the adiabatic temperature levels on the rotor blade tip is shown. With increased turbulent length scale the reduction in the adiabatic wall temperatures reduced from 10 K to about 6 K at about the 50% of the axial chord. However, the zone with the temperature rise is also eliminated using the large turbulent length scale.
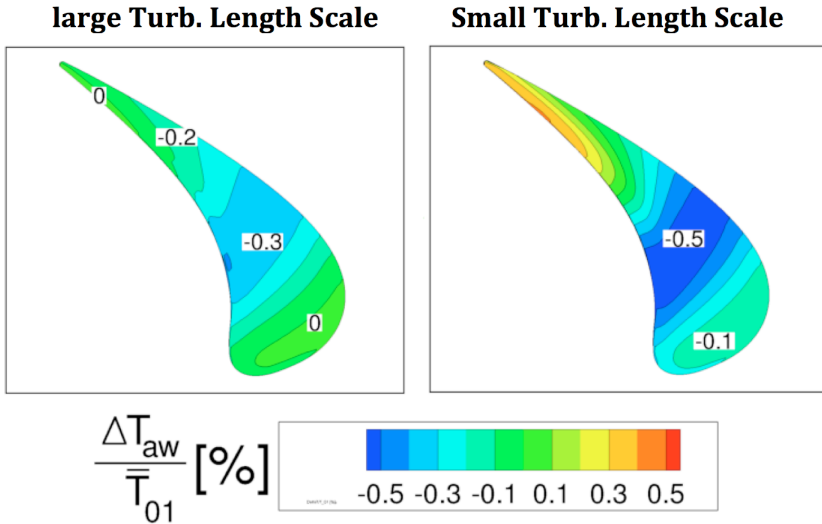
Figure 6.12 Difference in the rotor blade tip adiabatic wall temperatures between the two hot streak shapes imposed upstream of the stator with non-axisymmetric endwall profiling (ΔTaw = Taw,baseline - Taw,modified) imposed to high (on the left hand side) and low (on the right hand side) turbulent length scale conditions at the turbine inlet

6.4.   Discussion – Impact on the Combustor Design

Following the trends in the combustor outlet temperature distribution and studying the measured and simulated data published in the open literature non-symmetric hot streak shapes have been considered in this chapter. The non-symmetric hot streak has different spanwise extents either side of the stator. Making use of this circumferential temperature non-uniformity in favor of the rotor blade tip heat load by using the migration pattern characteristics was the main motivation behind this study. Now, the implications of this study in terms of the combustor design will be briefly discussed.

The migration pattern inside the turbine shows a periodic behavior with the number of the stators and in order to make use of this pattern the

temperature distribution at the combustor exit should also show a periodicity accordingly. This is a very first condition that has to be fulfilled. However, this condition sometimes can impose very strict requirements such as setting the number of the fuel injectors to be in integer ratio with the number of the stator blades. As discussed before, this is a very strict condition affecting both the design of the turbine and the combustor itself. In this chapter, an alternative method is proposed to alter the local circumferential temperature distribution close to the endwall which has the most dominant effect on the rotor blade tip heat load. Dilution air injected from the liner to control the radial temperature profiles already could also be used to shape the circumferential temperature distribution along the casing as well in a way that is in accordance with the migration pattern discussed. The circumferential non-uniformity in the migration pattern in this turbine geometry would necessitate bigger dilution holes positioned close to the suction side of the stator blade to provoke a deeper penetration of the dilution air. On the contrary, smaller size holes can be positioned close to the pressure side of the stator blade such that a non-axisymmetric hot streak shape similar to the one studied in this chapter forms at the turbine inlet. In full annular combustors used in the modern aircrafts all the fuel injectors are placed in a common liner and what is proposed here is to have a circumferentially non-uniform dilution hole size distribution on the liner and to clock these according to the flow patterns observed instead of clocking the fuel injectors themselves. This method is proposed as a more flexible way of modifying the combustor outlet temperature distribution as opposed to the fuel injector-stator clocking.

7.   Discussion & Conclusions

In this numerical study the effect of the combustor outlet temperature non-uniformities on the turbine aero-thermodynamics has been in detail investigated. Temperature non-uniformities modeling the real combustor outlet temperature distributions have been experimentally generated and measurements have been conducted in LEC's axial research turbine facility "LISA". Two hot streak shapes have been considered. With its relatively high circumferential temperature gradients the circular hot streak case models the temperature distribution downstream of the can-annular combustors. For the second experimental study a non-axisymmetric hot streak shape has been considered that has a prolonged circumferential extent at the center and towards the endwalls its circumferential extents are reduced. Compared to the circular hot streak it has a lower circumferential non-uniformity around the midspan. With these characteristics the shape reflects the trend in the reduction in the circumferential temperature gradients along the mid span in modern full-annular combustors. Using the measured inlet boundary conditions from the measurements unsteady, multi row RANS simulations have been conducted with the in-house CFD capabilities. Numerical predictions of the solver have been extensively validated with the very detailed and time resolved measurement results especially in the aspects of the flow that had a direct influence on the area of research.

The acquired understanding about the flow physics is utilized in shaping the combustor outlet temperature distributions taking the combustor framework into account such that they can be realizable in real practice. The effect of the modifications done in the combustor outlet temperature distribution on the rotor blade heat load has been investigated. Finally, the implications of this study for the combustor design have been discussed.

Necessary tools such as the unsteady particle tracking tool has been developed which improved the understanding about the hot streak migration physics considerably and supplied very practical information.

Accurate prediction of the secondary flows is very crucial for the turbomachinery CFD. Especially in HP turbines, where low aspect ratio blades are used, they cover a very considerable portion of the passage and affect the aerothermodynamics even at midspan. However, in the RANS approach very high aspect ratio cells are used to resolve the boundary layers where the secondary flows are initiated from. The solver's accuracy in resolving the boundary layers and also predicting the secondary flow regions such as the tip leakage vortex is substantially increased. The developed anisotropic scaling approach for the scalar, nonlinear artificial dissipation scheme provides a superior accuracy over the existing approaches (utilizing second order central space discretization) shown in the literature in resolving the boundary layers. More detailed outcomes of this thesis are listed below.

7.1.   Contributions to the Numerical Tools

The following contributions have been added to the in-house numerical tools during the period of this thesis.

i) Wilcox k-ω Turbulence Model:

The existing Wilcox [29] k-ω turbulence model implementation based on the Ni's Lax-Wendroff approach has been substantially improved in terms of the accuracy and robustness.

- A high-resolution, non-oscillatory, second order upwind discretization scheme has been used for the convective part of the turbulence model equations.

- Sweby [55] flux limiter has been utilized.

- The implementation can work on the unstructured, quadrilateral meshes where multi-block structured meshes are merged into a single unstructured mesh.

- This scheme proved to be robust and stable on a variety of steady and unsteady flow scenarios without necessitating additional

artificial smoothing algorithm.

- The implementation has been validated on flat plate scenarios, on external aerodynamics and also on multi-row axial turbine aerodynamics using the time resolved measurements from LEC's axial turbine facility "LISA".

- According to the measurement results the model has some deficiencies predicting the turbulence field within the vortical structures present in secondary flows in axial turbines.

ii) A New, Anisotropic Scaling Approach for Scalar, Non-linear Artificial Dissipation Scheme

A new, anisotropic approach for the scaling of the smoothing coefficients of the JST type scalar artificial dissipation scheme has been developed. The developed scaling approach considers the dependency of the inherent damping characteristics of the Ni's Lax-Wendroff scheme on the local CFL number which is particularly important for the high aspect ratio cells used close to the walls in RANS simulations. Additionally, the modeled eddy viscosity level is also taken into account in the scaling of the smoothing coefficients. The new algorithm is tested on a variety of flow scenarios.

- The developed anisotropic artificial dissipation scheme considerably increased the accuracy of the solver at the wall.

- The present approach can predict the wall shear at the turbulent boundary layers without artificial oscillations and also without contamination of the boundary layers.

- The increased accuracy of the present approach is also demonstrated in multi-row, axial turbine simulations in predicting of the secondary flow patterns downstream of the rotating blade row.

  ➢ The artificial dissipation scheme used had a very considerable effect on the mixing rate of the tip leakage vortex after it has

been emerged as a jet through the tip clearance. There was only a minor difference in the tip leakage mass flow rates between the different dissipation schemes used. The additional cell Reynolds number scaling of the smoothing coefficients increased the accuracy in the near wake region of the rotor blade mainly by interacting with the turbulence model; leading the model to predict a higher eddy viscosity level. The relative error in the relative total pressure level inside the tip leakage vortex is reduced from 11% with the isotropic artificial dissipation scheme to 7% with the developed anisotropic artificial dissipation scheme. A much more considerable improvement is observed in the Mach number predictions downstream of the rotor within the tip leakage vortex.

➢ The deficit in the efficiency predictions reduced from 0.7% with the isotropic dissipation scheme to 0.4% with the anisotropic dissipation scheme.

- A further improvement is observed in the unsteady, one stage turbine simulations with the presence of temperature non-uniformities.

➢ The difference in the peak temperature levels between the measurements and the calculation results dropped from 0.7 % of the mean total temperature level at the turbine inlet to 0.6 %

➢ The reduced advantage of the developed artificial dissipation scheme might be due to the coverage of the hot streak of the whole blade passage where H-grid with low aspect ratio cells is present.

- The anisotropic artificial dissipation scheme increases the computation time on GPU by about 30% over the computation time with the isotropic artificial dissipation scheme.

iii) GPU Acceleration

The in-house solver "MULTI3" has been GPU - accelerated. The restructuring and parallelization of the laminar part of the solver have been carried out by Huber [61]. Following developments have been conducted since then.

- Parallelization of the k-ω turbulence model

- Parallelization of the developed anisotropic dissipation scheme

- Additional restructuring has also been conducted to reduce the memory usage of the solver for the multi-row simulations. As a result, the memory requirement of the code decreased by 20% for the multi-row turbine simulations. For multi-row simulations the solver requires about 0.8 GB of memory per 1 million mesh points using single precision accuracy.

- An unsteady, multi-row URANS simulation using k-ω turbulence model with a mesh size up to 6 million nodes can be conducted on a single "Nvidia C2070" GPU with 5.3 GB accessible onboard memory using single precision accuracy.

- The final implementation resulted in a 16X reduction in run time on a single "Nvidia C2070" GPU over the run time of a single core of the "AMD Opteron 2435" CPU using double precision. The current latest Nvidia GPU model "K20X" resulted in a 30X speedup over the single core of the "AMD Opteron 2435" CPU.

- An unsteady, one-and-half stage turbine simulation with 4.5 million mesh points can be completed within 24 hours on a single "Nvidia C2070" GPU and within 12 hours on a single "Nvidia K20X" GPU using even the costly anisotropic artificial dissipation approach.

iv) Post-processing

An unsteady particle tracking tool has been developed that runs as a post-processor on the unsteady flow data generated by the flow solver.

- The tool can deal with particles both with [90] and without mass.

- Special treatment for the particles close to the solid boundaries is developed that allows to use considerably larger time steps for the particles close to the solid boundaries by imposing an additional impermeability condition inside the particle tracking tool. In addition, it has been also used for modeling the solid particle's collisions with the blade walls.

7.2.   Effect of Hot Streaks on High Pressure Turbine Aerodynamics

- Unsteady particle tracking studies investigating the migration pattern to the rotor blade tip revealed that the temperature non-uniformities imposed at the turbine inlet increase the spanwise transport within the turbine.

- The increase in the spanwise transport takes must have taken place inside the rotor row since temperature non-uniformities do not change the streamline pattern inside the stationary blade rows according to the Munk and Prim [10] principle.

- Unlike in stators hot streaks rise the relative total pressure level within the rotating blade rows. The rise in the relative total pressure level increased the adiabatic wall temperatures at the rotor pressure side that would correspond to 5K in real engine conditions. On the other hand, no effect on the adiabatic wall temperature distribution at the suction side is observed. For the first time in the literature the effect of the hot streak secondary flows are isolated and their effect on the rotor heat load is shown.

7.3. Effect of the Stator Aerodynamics on the Hot Streak Migration

- The particle tracking study revealed a considerable circumferential non-uniformity in the spanwise migration patterns across the opposite sides of the stator blade.

- This behavior has been observed not only in presence of hot streaks but even a uniform total temperature distribution was imposed at the turbine inlet.

- The particles emerging close to the stator's suction side can migrate to the rotor blade tip even if they have been originated at lower spanwise positions compared to the particles at the stator's pressure side. The aerodynamics of the radially stacked stators affects this pattern in two aspects.

    ➢ Within the stator quite considerable spanwise migration patterns have been observed. At the stator suction side the flow migrates towards the shroud endwall and at the pressure side it migrates towards the hub. The opposite migration patterns lead to about 10% divergence in the spanwise positions of the particles downstream of the stator.

    ➢ Downstream of the stator the pitch angle distribution shows opposite signs at the opposite sides of the stator blade. At the suction side due to the positive pitch angle the flow is directed towards the shroud and at the pressure side the flow is directed towards the hub endwall. This behavior is validated trendwise by the experimental measurements as well. But in terms of the magnitudes the predicted pitch angle distributions were higher than the ones measured. The observed pitch angle distribution might affect the spanwise migration within the rotor row.

- The stator aerodynamics influences the spanwise mixing of the hot streak. When the hot streak impinges on the stator's pressure side it spreads along the spanwise direction leading the peak temperature

to drop and the distribution downstream of the stator becomes less peaked. On the other hand, when the hot streak migrates close to the suction side it is much less diffused in spanwise direction and a more peaked radial temperature profile forms downstream of the stator.

- The circumferential non-uniformity in the spanwise migration patterns observed across the opposite sides of the stator blade is weakened by the effect of the non-axisymmetric endwall profiling.

- The non-axisymmetric endwall profiling at the stator enhanced the spanwise migration patterns within the stator but the divergence of the streamlines downstream of the stator was reduced. Two streamlines released at 90 % span close to opposite sides of the stator with axisymmetric endwalls are diverted by 5 % which was reduced to 2.5 % due to the effect of the non-axisymmetric endwall profiling. The change in the endwall aerodynamics weakened the circumferential non-uniformity in the spanwise migration patterns observed across the opposite sides of the stator blade. Also endwall profiling had an effect on the loading distribution on the blade and which might also be effective in the difference in the migration pattern between the two stator geometries.

7.4. Effect of Hot Streak Shaping on the Rotor Blade Heat Load

The effect of the hot streak's circumferential orientation relative to the stator blade on the rotor blade heat load has been investigated. In all the cases the same circumferentially mass averaged radial temperature profiles have been used. The modifications conducted in the hot streak's orientation in the circumferential direction relative to the stator blade led to spanwise heat load re-distribution on the rotor blade. The change in the heat load distribution was consistent with the observations made in the particle tracking study consistent with the convection dominated flow pattern inside the turbine.

Two different hot streak shapes have been considered.

Circular hot streak shape:

- Due to its pronounced circumferential temperature gradients the clocking of the circular hot streak showed very effective results in terms of the rotor blade heat load. Clocking the circular hot streak by even 10% of the stator pitch towards the pressure side resulted in a reduction in the rotor tip adiabatic wall temperature levels that would correspond up to 24 K in real engine conditions.

Non-symmetric hot streak shapes:

- Consistent with the particle tracking studies, among the two hot streak shapes considered the baseline hot streak shape with its larger spanwise extent aligned with the stator pressure side resulted in a lower heat load on the rotor tip especially at about the 50 % axial chord.

- Impinging the side of the hot streak with its spanwise larger extent onto the pressure side of the stator led to a more flat temperature distribution downstream of the stator which reduced the heat load on the rotor blade at the midspan. However, the adiabatic temperature levels close to the endwalls of the rotor blade are accordingly increased which was less severe when a large turbulent length scale level at the turbine inlet was imposed.

- Compared to the clocking study the modifications conducted with the non-symmetric hot streak shape (aligning the longer spanwise edge close to the pressure side or suction side) had a rather limited effect on the rotor tip heat load. The reductions in the rotor blade tip adiabatic wall temperatures are between 5 and 10 K when the TET is scaled up to real engine conditions.

7.5. Impact on the Combustor Design

- Circumferential temperature variations downstream of the

combustor are imported. They are not averaged out within the rotor and lead to spanwise heat load re-distribution on the rotor blade.

- Two different hot streak shapes (circular and non.-axisymmetric) with differing circumferential temperature variations have been considered.

- To vary the hot streak's circumferential orientation relative to the stator two different approaches have been followed which could be practically applied on the real combustor – turbine interface.

   ➢ The fuel injector – stator clocking requires that the fuel injector – stator ratio is an integer, which is a major constraint affecting the design of both the turbine and the combustor itself. Moreover, due the advances in the combustor technology the circumferential temperature gradients are reduced which would probably reduce the benefits of the fuel injector clocking than it is in this numerical study.

   ➢ A new, more practical way of shaping the hot streaks is proposed. The shaping of the circumferential temperature distributions via positioning of the dilution holes on the liner is offered as a more flexible way of modifying the temperature distribution close to the endwalls. In order to achieve a periodic pattern in the circumferential temperature distribution the size of the dilution holes on the liner have to be adjusted according to the spanwise migration pattern. Aligning larger diameter dilution holes close to the stator suction side would ensure a deeper penetration of the dilution air [4] and produce a temperature distribution that is close to the baseline hot streak shape used.

Bibliography

[1]   Han, J., Dutta, S., and Ekkad, S., Gas Turbine Heat Transfer and Cooling Technology, Taylor & Francis, 2000.

[2]   Povey, T., Chana, K. S.,Jones, T.V., Hurrion,J., "The Effect of Hot-Streaks on HP Vane Surface and Endwall Heat Transfer: An Experimental and Numerical Study," ASME J. of Turbomachinery, vol. 129, no. 1, pp. 1-12, 2007.

[3]   W. R. Bender, "Lean Pre-Mixed Combustion," in The Gas Turbine Handbook, 2006, pp. 217-227.

[4]   S. Samuelsen, "Rich Burn,Quick - Mix, Lean Burn (RQL) Combustor," in The Gas Turbine Handbook, 2006, pp. 227-232.

[5]   A.W. LeFebvre, 'Gas Turbine Propulsion', New York : McGraw-Hill, 1983

[6]   J. Odgers, and D. Kretschmer, 'Gas Turbine Fuels and Their Influence on Combustion', Energy and Engineering Series, Tunbridge Wells, Kent : Abacus Press, 1986

[7]   'The Jet Engine', Rolls-Royce Limited, Derby, 3rd Edition, 1969

[8]   Povey,T., Qureshi, I., "Developments in hot-streak simulators for turbine testing," ASME J. of Turbomachinery, vol. 131, no. 03-1009, 2009.

[9]   Butler, T. L., Sharma, O. P., Joslyn, H. D., and Dring, R. P., "Redistribution of an inlet temperature distortion in an axial flow turbine stage," AIAA J. of Propulsion and Power, vol. 5, no. 1, p. 64–71, 1989.

[10]   Munk, M. and Prim, R.C., "On the Multiplicity of Steady Gas Flows Having the Same Streamline Pattern," Proc. Natl. Acad. Sci. U.S.A., vol. 33, pp. 137-141, 1947.

[11] Kerrebrock, J., and Mikolajczak, A., "Intra-stator transport of rotor wakes and its effect on compressor performance," ASME J. of Engineering for Power, vol. 92, no. 4, p. 359–368, 1970.

[12] Rai, M., and Dring, R., "Navier-stokes analysis of the redistribution of inlet temperature distortions in a turbine," AIAA J. of Propulsion and Power, vol. 6, p. 276–282, 1990.

[13] Krouthen, B., and Giles, M., "Numerical investigation of hot streaks in turbines," AIAA J. of Propulsion and Power, vol. 6, no. 6, p. 769–776, 1990.

[14] Dorney, D., Davis, R., Edwards, D., and Madavan, N., "Unsteady analysis of hot streak migration in a turbine stage," AIAA J. of Propulsion and Power, vol. 8, no. 2, p. 520–529, 1992.

[15] Takahashi, R., Ni, R.H., "Unsteady hot streak migration through a 1-stage turbine," in AIAA paper 96-2796, 1996.

[16] Dorney, D., and Burlet, K., "Hot streak clocking in a 1-1/2 stage turbine," AIAA J. of Propulsion and Power, vol. 12, no. 3, p. 619–620, 1996.

[17] An, B., Liu, J., and Jiang, H., "Numerical investigation on unsteady effects of hot streak on flow and heat transfer in a turbine stage," ASME J. of Turbomachinery, vol. 131, no. 03-1015, 2009.

[18] Dorney, D., Davis, R., Edwards, D., and Madavan, N., "Effects of tip clearance on hot streak migration in a high-subsonic single-stage turbine," ASME J. of Turbomachinery, vol. 122, no. 4, p. 613–620, 2000.

[19] Prasad, D. , Hendricks, G., "A Numerical Study of Secondary Flows in Axial Turbines With Application to Radial Transport of Hot Streaks," ASME J. of Turbomachinery, vol. 122, pp. 667-673, 2000.

[20] Schuepbach, P., Abhari, R.S., Rose, M.G., Germain, T., Raab, I., Gier, J., "Improving Efficiency of a High Work Turbine Using Non-Axisymmetric Endwalls: Part II—Time-Resolved Flow Physics," ASME Paper GT2008-50470, 2008.

[21] Germain, T., Nagel, M., Raab, I., Schuepbach, P., Abhari, R. S., "Improving Efficiency of a High Work Turbine Using Non-Axisymmetric Endwalls: Part I—Endwall Design and Performance," ASME Paper GT2008-50469, 2008.

[22] Jenny, P., Abhari, R.S., Rose, M.G., Brettschneider, M., Gier, J., "A Low Pressure Turbine with Profiled End Walls and Purge Flow Operating with a Pressure Side Bubble," ASME Paper GT2011-46309, 2011.

[23] Shang, T., and Epstein, A., "Analysis of hot streak effects on turbine rotor heat load," ASME J. of Turbomachinery, vol. 119, no. 3, p. 544–553, 1997.

[24] Jenny, P., Lenherr, C., Kalfas, A., and Abhari, R., "Effect of unsteady blade row interaction on hot streak migration in an axial turbine," ASME Paper GT2010-23034, 2010.

[25] R. Clifford, "Rotating Heat Transfer Investigations on a Multipass Cooling Geometry," in AGARD CP 390, 1985.

[26] Bunker, R.S., "Advances in Turbomachinery Aero-Thermo-Mechanical Design Analysis," VKI Lecture Series, 02 2007.

[27] Bunker, R.S., Bailey,J.C., Ameri,A.A., "Heat Transfer and Flow on the First-Stage Blade Tip of a Power Generation Gas Turbine: Part 1-Experimental Results," ASME J. of Turbomachinery, vol. 122, no. 2, pp. 263-271, 2000.

[28] Ameri, A.A., and Bunker., R.S., "Heat Transfer and Flow on the First Stage Blade Tip of a Power Generation Gas Turbine, Part 2: Simulation Results," ASME J. of Turbomachinery, vol. 122, pp. 272-277, 2000.

[29] Wilcox,D.C.,'Reassessment of the Scale-Determining Equation for Advanced Turbulence Models', AIAA Journal, vol. 26, No. 11, 1988, pp. 1299-1310

[30] Bunker, R.S., "Axial Turbine Blade Tips: Function, Design, and Durability," AIAA J. of Propulsion and Power, vol. 22, no. 2, pp. 271-285, 2006.

[31]   Ameri,A.A., Steinthorsson, E., Rigby, D.L., "Effect of Squealer Tip on Rotor Heat Transfer and Efficiency," ASME J. of Turbomachinery, vol. 120, no. 4, pp. 753-759, 1998.

[32]   Mischo, B., Behr, T., and Abhari, R., "Flow physics and profiling of recessed blade tips: Impact on performance and heat load," ASME J. of Turbomachinery, vol. 130, no. 02-0008, 2008.

[33]   Denton, J.D.,"Some Limitations of Turbomachinery CFD", ASME Paper GT2010-22540, 2010

[34]   Zhang, Q., Ligrani, P., 'Aerodynamic Losses of a Cambered Turbine Vane: Influences of Surface Roughness and Freestream Turbulence Intensity', Journal of Turbomachinery, vol128:536-546, 2006

[35]   Boyle, R.J., Senyitko, R.G., 'Measurements and Predictions of Surface Roughness Effects on Turbine Vane Aerodynamics', ASME Paper GT2003-38580, 2003

[36]   Rao, V. N., Loveday, R. J., Tucker, P.G., Lardeau, S., 'Large Eddy Simulations in Turbines: Influence of Roughness and Free-Stream Turbulence', Flow, Turbulence and Combustion, 2013

[37]   Brandvik, T., Pullan, G. , "An Accelerated 3D Navier-Stokes Solver for Flows in Turbomachines," ASME J. of Turbomachinery, vol. 133, no. 021025, pp. 1-9, 2011.

[38]   Phillips, E.H., Davis, R. L., Owens, J.D., "Unsteady Turbulent Simulations on a Cluster of Graphics Processors," in AIAA-2010-5036, 2010.

[39]   R. Ni, "A Multiple Grid Scheme for Solving the Euler Equations," AIAA Journal, vol. 20, no. 3, p. 1565–1571, 1981.

[40]   Tallman,J. , Lakshminarayana, B., "Numerical Simulation of Tip Leakage Flows in Axial Flow Turbines, With Emphasis on Flow Physics: Part I - Effect of Tip Clearance Height," ASME J. of

[41]   B. Mischo, "Axial Turbine Rotor Aero-thermal Blade Tip Performance Improvement through Flow Control," ETH Zurich, Zurich, 2008

[42] J. Blazek, Computational Fluid Dynamics: Principles and Applications, Elsevier , 2005.

[43] Giles,M., "Non-reflecting Boundary Conditions for Euler Equation Calculations," in AIAA Paper 89-1942-CP, 1989.

[44] Burdet, A., "A computationally efficient feature based jet model for prediction of film cooling flows," ETH Zurich, Zurich, 2005.

[45] Baldwin,B., Lomax, H.,"Thin Layer Approximation and Algebraic Model for Separated Turbulent Flows," in AIAA paper 78-257, 1978.

[46] Spalart, P. R., Allmaras, S. R., "A one-equation turbulence model for aerodynamic flows," La Recherche Aérospatiale, vol. 1, p. 5, 1994.

[47] Kato, M. and Launder, B. E., "The Modeling of Turbulent Flow Around Stationary and Vibrating Square Cylinders", Proc. 9th Symposium on Turbulent Shear Flows, Kyoto, pp. 10.4.1-10.4.6., 1993

[48] Chima, R.V., "A k-ω Turbulence Model for Quasi-Three-Dimensional Turbomachinery Flows" , NASA TM 107051, 1996

[49] Liu,F., Zheng,X., "Staggered Finite Volume Scheme for Solving Cascade Flow with a k-ω Turbulence Model," AIAA Journal, vol. 32, no. 8, pp. 1589-1597, 1994.

[50] Godunov, S.,"Finite Difference Method for Numerical Computation of Discontinuous Solutions of the Equations of Fluid Dynamics," Mat. Sb. , vol. 47, pp. 271-306, 1959.

[51] Darwish, M.S., Moukalled, F., "TVD Schemes for Unstructured Grids," International Journal of Heat and Mass Transfer, vol. 46, pp. 599-611, 2003.

[52] Van Leer, B.,"Towards the Ultimate Conservative Difference Scheme. II: Monotonicity and Conservation Combined in a Second Order Scheme," J. of Computational Physics, 14, pp. 361-370, 1974.

[53] Van Albada, G.D.,Van Leer, B., Roberts, W.W.,"A Comparitive

Study of Computational Methods in Cosmic Gas Dynamics," Astron. Astrophy., 108, pp. 76-84, 1982.

[54] Roe,P.L., "Some Contributions to the Modeling of Discontinuous Flows," Proceedings of 1985 AMS-SIAM Summer Seminar on Large Scale Computing in Fluid Mechanics, Lectures in Applied Mechanics, vol. 22, Springer Verlag, New York, pp. 163-193,1985.

[55] Sweby, P.K., "High resolution schemes using flux-limiters for hyperbolic conservation laws", SIAM J. Num. Anal. 21 (5),pp. 995–1011,1984

[56] C. Hirsch, Numerical Computation of Internal and External Flows: Numerical Computation V 2: Computational Methods for Inviscid and Viscous Flows, John Wiley & Sons, 2002.

[57] A. Jameson, "Time Dependent Calculations using Multigrid with Applications to Unsteady Flows Past Airfoils and Wings," in AIAA paper 91-1596, 1991.

[58] T. Behr, "Control of Rotor Tip Leakage and Secondary Flow by Casing Air Injection in Unshrouded Axial Turbines", ETH Zurich, Zurich, 2007.

[59] Kulisa,P.,Dano, C., 'Assessment of Linear and Non-Linear Two-Equation Turbulence Models for Aerothermal Turbomachinery Flows', Journal of Thermal Science, vol. 15:1, pp. 14-26, 2005

[60] M. Wolfe, "The PGI Accelerator Programming Model on NVIDIA GPUs," PGI, 2009. [Online]. Available: http://www.pgroup.com/lit/articles/insider/v1n1a1.htm.

[61] Huber, M., "GPU Acceleration of a Fluid Flow Solver for Turbomachinery Applications," LEC - ETH Zurich, Zurich, 2011.

[62] http://www.nvidia.com/docs/IO/43395/NV_DS_Tesla_C2050_C2070_jul10_lores.pdf

[63] Mansour, M., Chokani, N., Kalfas, A., and Abhari, R., "Impact of time-resolved entropy measurements on a one-and-1/2-stage axial turbine performance," ASME Paper GT2008-50807, 2008.

[64] Lenherr, C., Kalfas, A., and Abhari, R., "High temperature fast

response aerodynamic probe," ASME Paper GT2010-23010, 2010.

[65] Jenny, P., Lenherr, C., Kalfas, A., Abhari, R.S., "Effect of Hot Streak Migration on Unsteady Blade Row Interaction in an Axial Turbine," ASME J. of Turbomachinery, vol. 134, no. 5, pp. 1-9, 2012.

[66] Barringer, M.D.,Thole, K.A.,Polanka, M.D., "Experimental Evaluation of an Inlet Profile Generator for High Pressure Turbine Tests," ASME Paper GT2006-90401, 2006.

[67] Tarasov, D., Lebedev, A., Simin, N., Grinevich, V.,"Numerical Simulation of Combustion Processes and Analysis of Temperature Field Non-uniformity in GTE-65 Gas Turbine Combustor," ASME Paper GT2010-23798, 2010.

[68] Felten,F.N.,Kapetanovic,S.,Holmes,D.G.,Ostrowski,M.,"Gas Turbine Temperature Prediction using Unsteady CFD and Realistic Non-uniform 2D Combustor Exit Properties," ASME Paper GT2008-50275, 2008.

[69] Regina, K., Basol,A.M., Jenny,P., Kalfas,A.I.,Abhari, R.S., "Hot Streak Shaping and Migration in an Axial Turbine," in IGTC, 2011.

[70] Jameson, A., Schmidth, W., Turkel, E., "Numerical Solutions of Euler Equations by Finite Volume Methods using Runge-Kutta Time Stepping Schemes," in AIAA Paper 81-1259, 1981.

[71] Pulliam, T. H. and Steger, J. L. Implicit Finite- Difference Simulations of Three Dimensional Compressible Flow, AIAA J Vol. 18 1980 pp. 159

[72] Beam, R. and Warming, R. F. An Implicit Finite-Difference Algorithm for Hyper- bolic Systems in Conservation Law Form, J. Comp. Phys., Vol. 22, 1976, pp. 87-110

[73] Swanson, R.C., Turkel, E., "On Central-Difference and Upwind Schemes", 1992, J. of Comp. Physics, Vol. 101, pp.292-306

[74] R. D. Richtmeyer and K.W. Morton, 'Difference Methods for Initial-Value Problems', John Wiley & Sons, second edition, 1967

[75] D. G. Holmes, S.D. Connell, 'Solution of the 2-D Navier-Stokes

Equations on Unstructured Adaptive Grids', AIAA Paper 89-1932-CP, 1989

[76]   A. Saxer, "A Numerical Analysis of 3D Inviscid Stator/Rotor Interactions Using Non-Reflecting Boundary Conditions", Phd thesis, 1992.

[77]   R. C. Swanson, R. Radespiel, E. Turkel, 'On Some Numerical Dissipation Schemes', Journal of Computational Physics, 147:518-544, 1998

[78]   T. H. Pulliam, Artificial dissipation for the Euler equations, AIAA J. 24, 1931 (1986)

[79]   R. C. Swanson and E. Turkel, 'Artificial dissipation and central difference schemes for the Euler and Navier-Stokes equations', in AIAA 8th Computational Fluid Dynamics Conference, AIAA, 1987, p. 55. [AIAA Paper 87-1107-CP]

[80]   C. Hirsch, 'Numerical Computation of Internal & External Flows : Volume 1 Fundamentals of Computational Fluid Dynamics', 2007, Elsevier, Oxford

[81]   Y. Wang, K.Hutter, 'Comparisons of Numerical Methods with respect to Convectively Dominated Problems, International Journal for Numerical Methods in Fluids', 37:721-745, 2001

[82]   E. Shalman, A. Y akhot, S. Shalman, O. Igra, and Y. Yadlin, 'Attenuating Artificial Dissipation in the Computation of Navier-Stokes Turbulent Boundary Layers', Journal of Scientific Computing, 13(2): 151-172,1998

[83]   Tatsumi, S., Martinelli, L., Jameson, A., "Flux-Limited Schemes for Compressible Navier-Stokes Equations", AIAA J., vol. 33, no.2, pp. 252-261, 1995.

[84]   Mackenzie, J.A., "An Investigation of Artificial Dissipation for the Cell-Vertex Finite Volume Method", Inter. J. for Numerical Methods in Fluids, vol. 21, pp. 499-522, 1995.

[85]   G. Kalitzin, G. Medic, G. Iaccarino, P. Durbin, 'Near-wall behavior of RANS turbulence models and implications for wall functions',

Journal of Computational Physics, 204:265-291, 2005

[86]   Schuepbach, P., Abhari, R.S., Rose, M.G., Gier, J. , "Influence of Rim Seal Purge Flow on the Performance of an Endwall-Profiled Axial Turbine," ASME J. of Turbomachinery, vol. 133, no. 2, 2011.

[87]   brutuswiki.ethz.ch

[88]   Cumpsty, N.A., Horlock, J.H., "Averaging nonuniform flow for a purpose," ASME J. of Turbomachinery, vol. 128, no. 1, pp. 120-129, 2006.

[89]   Ong, J., and Miller, R., "Hot streak and vane coolant migration in a downstream rotor," ASME Paper GT2008-50971, 2008.

[90]   G. Sassano, "Modeling of Solid Particle Migration in a High Pressure Turbine," LEC - ETH Zurich, Zurich , 2011.

A. Non-dimensionalization of the Wilcox *k-ω* Turbulence Model Equations

Dimensional form of the k-equation

$$\left[\frac{\partial(\rho k)}{\partial t}+\frac{\partial\left(\rho u_j k\right)}{\partial x_j}\right]=\frac{\partial}{\partial x_j}\left[\left(\mu+\sigma^*\mu_t\right)\frac{\partial k}{\partial x_j}\right]+\tau_{ij}\frac{\partial u_i}{\partial x_j}-\beta^*\rho\omega k$$

Eq A.1

Dimensional form of the ω-equation

$$\left[\frac{\partial(\rho\omega)}{\partial t}+\frac{\partial\left(\rho u_j\omega\right)}{\partial x_j}\right]=\frac{\partial}{\partial x_j}\left[\left(\mu+\sigma\mu_t\right)\frac{\partial\omega}{\partial x_j}\right]+\left(\frac{\alpha\omega}{k}\right)\tau_{ij}\frac{\partial u_i}{\partial x_j}-\beta^*\rho\omega^2$$

Eq A.2

A.1. Non-dimensionalization of the k-equation

For the non-dimensionalization of the k-equation the following reference variables are used.

$$\rho^*=\frac{\rho}{\rho_{ref}}$$

$$k^*=\frac{k}{vel_{ref}^2};\quad \omega^*=\frac{\omega}{vel_{ref}/l_{ref}}$$

$$t^*=\frac{t}{l_{ref}/vel_{ref}}$$

$$x_j^* = \frac{x_j}{l_{ref}}; \quad u_j^* = \frac{u_j}{vel_{ref}}$$

$$\mu_t^* = \frac{\mu_t}{\mu_{ref}vel_{ref}l_{ref}}; \quad \mu_{ref} = \rho_{ref}vel_{ref}l_{ref}$$

A.1.1.Non-dimensionalization of the LHS

$$\left[\frac{\partial(\rho k)}{\partial t} + \frac{\partial(\rho u_j k)}{\partial x_j}\right]$$

Eq A.3

Using the non-dimensionalized forms of the variables the LHS turns into the following form.

$$\left(\frac{\rho_{ref}vel_{ref}^3}{l_{ref}}\right)\left[\frac{\partial(\rho^* k^*)}{\partial t^*} + \frac{\partial(\rho^* u_j^* k^*)}{\partial x_j^*}\right]$$

Eq A.4

A.1.2.Non-dimensionalization of the Diffusive Terms on RHS

$$\frac{\partial}{\partial x_j}\left[\left(\mu + \sigma^* \mu_t\right)\frac{\partial k}{\partial x_j}\right]$$

Eq A.5

Non-dimensional form of this part is given below.

$$\frac{\partial}{\partial x_j}\left[\left(\mu + \sigma^* \mu_t\right)\frac{\partial k}{\partial x_j}\right] = \frac{\partial}{\partial x_j^*}\left[\left(\frac{\mu^*}{\mathrm{Re}_{ref}} + \sigma^* \mu_t^*\right)\frac{\partial k^*}{\partial x_j^*}\right]\left(\frac{\rho_{ref} vel_{ref}^3}{l_{ref}}\right)$$

Eq A.6

where Reynolds number is defined below

$$\mathrm{Re}_{ref} = \frac{\rho_{ref} vel_{ref} l_{ref}}{\mu_{ref}}$$

A.1.3. Non-dimensionalization of the Positive Source Term on RHS

$$\mu_t S_{ij}\Omega_{ij}$$

Eq A.7

the definitions of S and Ω are given in   Eq A.8.

$$S_{ij} = \sqrt{\frac{1}{2}\left(\frac{\partial u_i}{\partial x_j} + \frac{\partial u_j}{\partial x_i}\right)^2}, \quad \Omega_{ij} = \sqrt{\frac{1}{2}\left(\frac{\partial u_i}{\partial x_j} - \frac{\partial u_j}{\partial x_i}\right)^2}$$ Eq A.8

$$\mu_t S_{ij}\Omega_{ij} = \left(\frac{\rho_{ref} vel_{ref}^3}{l_{ref}}\right)\mu_t^* S_{ij}^*\Omega_{ij}^*$$

Eq A.9

A.1.4. Non-dimensionalization of the Negative Source Term on RHS

$$\beta^* \rho \omega k$$

<div align="right">Eq A.10</div>

Non-dimensional form of the sink term is derived below.

$$\beta^* \rho \omega k = \left(\frac{\rho_{ref} vel_{ref}^3}{l_{ref}} \right) \beta^* \rho^* \omega^* k^*$$

<div align="right">Eq A.11</div>

A.1.5. Non-dimensional Form of the k-equation

$$\left[\frac{\partial \left(\rho^* k^* \right)}{\partial t^*} + \frac{\partial \left(\rho^* u_j^* k^* \right)}{\partial x_j^*} \right] = \frac{\partial}{\partial x_j^*} \left[\left(\frac{\mu^*}{Re_{ref}} + \sigma^* \mu_t^* \right) \frac{\partial k^*}{\partial x_j^*} \right] + \mu_t^* S_{ij}^* \Omega_{ij}^* - \beta^* \rho^* \omega^* k^*$$

<div align="right">Eq A.12</div>

A.2. Non-dimensionalization of the ω-equation

Carrying out a similar procedure for the ω equation as it has been done for the k-equation, one can end up with the following non-dimensional form of the ω - equation.

$$\left[\frac{\partial \left(\rho^* \omega^* \right)}{\partial t^*} + \frac{\partial \left(\rho^* u_j^* \omega^* \right)}{\partial x_j^*} \right] = \frac{\partial}{\partial x_j^*} \left[\left(\frac{\mu^*}{Re_{ref}} + \sigma^* \mu_t^* \right) \frac{\partial \omega^*}{\partial x_j^*} \right] + \alpha S_{ij}^* \Omega_{ij}^* - \beta^* \rho^* \left(\omega^* \right)^2$$

<div align="right">Eq A.13</div>

B. Nomenclature

k	turbulent kinetic energy	$[m^2/s^2]$
P	pressure	[Pa]
S	rate of strain tensor	[1/s]
t	time	[s]
T	temperature	[K]
u	velocity vector	[m/s]
vel	magnitude of the velocity vector	[m/s]
y+	non-dimensional distance	[-]
Y	loss coefficient	[-]
x	position vector	[m]

Greek

ρ	density	$[kg/m^3]$
τ	shear stress tensor	$[N/m^2]$
δ_{ij}	Kronecker symbol	
ω	specific turbulence dissipation	[1/s]
μ	laminar viscosity	[kg/m/s]
μ_t	eddy viscosity	[kg/m/s]

Abbreviations

CFD	Computational Fluid Dynamics
CFL	Courant-Friedrichs-Levy
CPU	Central Processing Unit
CUDA	Compute Unified Device Architecture
GPU	Graphical Processing Unit
EGT	Exhaust Gas Temperature
FRAP	Fast Response Aerodynamic Probe
FRAP-HT	High Temperature Fast Response Aerodynamic Probe
FENT	Fast Response Entropy Probe
HP	high pressure
HS	hot streak
MPI	Message Passing Interface
OpenMp	Open Multi-Processing
PS	pressure side
PV	passage vortex
RANS	Reynolds Averaged Navier Stokes
Re	Reynolds number
SS	suction side
TET	turbine entry temperature
TLV	tip leakage vortex

Subscripts

abs	absolute state

aw	adiabatic wall
circ	circumferential direction
ref	reference state
rel	relative state
tot	total conditions
0	total conditions
1	turbine inlet
2	stator 1 outlet
3	rotor outlet

Superscripts

-	averaged value

C. Publications

Journal Publications

Basol, A.M. , Jafari, S., Abhari, R.S., "A New Anisotropic Scaling Approach for the Scalar, Non-linear Artificial Dissipation Scheme", submitted to the Journal of Computation Physics.

Basol, A.M., Regina, K., Kalfas A.I., Abhari R.S., 2012, "Integrated Combustor – Turbine Design for Improved Aerothermal Performance : Effect of Dilution Air Control", Journal of Engineering for Gas Turbines and Power, GT2011-46354

Basol, A.M., Jenny, P., Ibrahim, M., Kalfas, A.I., Abhari, R.S., 2011, "Hot Streak Migration in a Turbine Stage: Integrated Design to Improve Aero-Thermal Performance", Journal of Engineering for Gas Turbines and Power, Vol. 133, 019011

Conference Proceedings

Jafari, S. , **Basol, A.M.**, Chokani, N. , Abhari, R.S., "Simulations of Atmospheric Flow and Wind Turbine Wakes using a Preconditioned Multigrid" *to be presented at AIAA Sci Meeting, Maryland, USA, 2014*

Basol, A.M., Abhari, R.S. , 2013, "Performance Improvements of Centrifugal Compressors Through Shroud Cavity Leakage Management", ASME Turbo Expo 2013, GT2013 – 95809

Regina K., **Basol A.M**., Jenny P., Kalfas A.I., Abhari R.S. , 2011, "Hot Streak Shaping and Migration in an Axial Turbine", International Gas Turbine Congress vol. 10 (November 13-18, Osaka, Japan)

Basol, A.M., Regina, K., Kalfas A.I., Abhari R.S., 2011, "Integrated Combustor – Turbine Design for Improved Aerothermal Performance : Effect of Dilution Air Control", presented at ASME Turbo Expo 2011, Vancouver

Basol, A.M., Jenny, P., Ibrahim, M., Kalfas, A.I., Abhari, R.S., 2010, "Hot Streak Migration in a Turbine Stage: Integrated Design to Improve Aero-Thermal Performance", presented at ASME Turbo Expo 2010, Glasgow

D. Curriculum Vitae

Personal Data

Altug Melik Basol, born August 04, 1980 in Istanbul, Turkey

Education

1986 – 1991	Isik Lisesi, Istanbul, Turkey
1991 – 1999	Istanbul Lisesi, Istanbul, Turkey
1999 – 2004	B. Sc. Chemical Engineering / Process Engineering, Bogazici University, Istanbul, Turkey
2004 – 2007	M. Sc. Mechanical Engineering, Bogazici University, Istanbul, Turkey

Professional Experience

2007 – 2013	Research assistant and doctoral student at the Laboratory for Energy Conversion at the Swiss Federal Institute of Technology (ETH – Zurich), Zurich, Switzerland